Beyond Lithium-ion: Reaction Mechanisms of Low-Cost Rechargeable Zinc/Manganese Dioxide and Lithium/Sulfur Batteries

Yun Li

A dissertation

submitted in partial fulfillment of the

requirements for the degree of

Doctor of Philosophy

University of Washington

2019

Reading Committee:

Jihui Yang, Chair

Guozhong Cao

Fumio Ohuchi

Program Authorized to Offer Degree:

Materials Science and Engineering

University of Washington

Abstract

Beyond Lithium-ion: Reaction Mechanisms of Low-Cost Rechargeable Zinc/Manganese Dioxide and Lithium/Sulfur Batteries

Yun Li

Chair of the Supervisory Committee:
Professor Jihui Yang
Materials Science and Engineering

New rechargeable batteries beyond lithium-ion have attracted increasing interest due to their potential in commercializing various applications, including grid storage, electric vehicle (EV), etc. These new batteries hinge upon the respective storage/conversion mechanisms suitable for the particular application purposes. For instance, the stationary energy storage applications necessitate batteries to possess high cycling stability and, in some cases, high power densities, while high volumetric and gravimetric energy densities are critical for EV applications. Most importantly, all need to be cost competitive.

Rechargeable zinc/manganese dioxide (Zn/MnO_2) batteries are very promising for the stationary energy storage owing to their low cost, environmentally benign constituents, excellent safety, and relatively high energy density. Their usage, however, is largely hampered by the fast capacity fading. The complexity of the reactions has resulted in long-standing ambiguities of the

capacity fading of Zn/MnO_2 system. In this thesis, we find that both H^+/Zn^{2+} intercalation and conversion reactions occur at different voltages in Zn/MnO_2 and that the rapid capacity fading can clearly be ascribed to the rate-limiting and irreversible conversion reactions at a lower voltage. By limiting the irreversible conversion reactions, we successfully demonstrate ultrahigh power and long life that are superior to most of the reported zinc-ion batteries (ZIBs) or even some lithium-ion batteries (LIBs).

As for the application of batteries in the EV market, lithium/sulfur (Li/S) batteries hold great promise as the next-generation energy battery. Their practical application, however, is hindered by the rapid capacity fading associated with the dissolution of lithium polysulfides (LiPSs) into the organic electrolytes. By anchoring thiol (-SH) functional groups to the nonpolar surface of a mesoporous carbon host, we successfully impede these losses. This new strategy increases the surface polarity of conductive carbons and traps LiPSs inside cathodes. By utilizing various spectroscopic methods, we investigate the mechanisms of LiPS trapping, which originate from the electrostatic and covalent interactions of the thiol functional groups with Li^+ from the electrolyte and with S from the LiPS chains. The fundamental insight on the thiol functionality suggests a further rational design of multifunctional interfaces to achieve better Li/S performance.

TABLE OF CONTENTS

LIST OF FIGURES

LIST OF TABLES

ACKNOWLEDGEMENTS

I would like to express my sincere gratitude to Dr. Jihui Yang for his guidance and support throughout the years. As my research advisor and mentor, he has helped me set, focus on, and attain my research and professional goals. He also allowed me to work in General Motors (GM) as an intern for two summers and in the Pacific Northeast National Laboratory (PNNL) as a visiting student for half a year. Meanwhile, I truly appreciate what Jihui has taught me about critical thinking, open mind, integrity, leadership, and the importance of taking a step back to look at the big picture and not always focusing on just the details. I know I am prepared for my future endeavors because of my time here at the University of Washington.

I would also like to express my gratitude to my undergraduate research advisor Dr. Yong Yang who stimulated my passion for study abroad. Without him, I won't be able to chase my dreams here. In addition, I want to thank my Ph.D. committee members, Dr. Fumio Ohuchi, Dr. Guozhong Cao, and Dr. Junlan Wang for their support, advice, and guidance towards my Ph.D. work.

I'm grateful to my supervisors at GM and PNNL, Dr. Mei Cai, Dr. James R. Salvador, Dr. Chongmin Wang, and Dr. Langli Luo. The GM and PNNL experience helped better understand the connections among acdemica, industry, and research institute, which will benefit my future career without any doubt. I also appreciate other GM and PNNL colleagues, Dr. Yang He, Dr. Li Yang, Dr. Fang Dai, Dr. Qiangfeng Xiao, Dr. Mahmoud Abdelhamid, Dr. Michael Balogh, Dr. Xingchen Xiao, et al., for their help in training and discussion.

Sincerely thanks to Dr. Wanli Yang and Dr. Jinpeng Wu of the Lawrence Berkeley National Laboratory for the support of soft X-ray absorption spectroscopy (sXAS) work. Thanks to Mr. Bo Liu, Dr. Jiong Yang, and Dr. Wenqing Zhang from Shanghai University for their help in density

functional theory (DFT) calculation. I would also like to acknowledge the scientists in Dr. Alex Jen's group, Dr. Sei-Hum Jang, Mr. Dion Hubble, Mr. Jiaxu Qin, Mr. Francis (Ray) Lin, and Mr. Ian A. Murphy for their cooperation on the Li/S project. Additionally, thanks to the funding support from the State of Washington and the US Department of Energy and the fellowships from the Advanced Materials for Energy and the Clean Energy Institute. Without them, the work would not have been possible to be finished.

I always feel indebted to the present and past members of the Yang group, who have helped me learn and grow through the years and have collaborated with me on many projects. I learned a great deal from our many postdocs, including Dr. Shanyu Wang, Dr. Jiong Yang, Dr. Mengyu Yan, Dr. Lihua Wu, and Dr. Xiaoyu Jiang. I would also like to thank Dr. Carolina Vinado and Mr. Xiang Han, who were also graduate students at the time. In particular, I sincerely thank Dr. Shanyu Wang and Dr. Carolina Vinado for their guidance and accompany throughout my graduate career.

There are many friends that I was lucky enough to have, who shared happiness and sorrow with me and always kept me grounded through this arduous journey. I owe sincere thankfulness to Mochong Duan, Li Wang, Xiao Fu, Moke Mao, Ting Zhao, Jieming Li, and Chu Han. Moreover, I would like to thank James' and Shanyu's families for their hospitality and "parental" care. The warm feeling of a home they provided has been strong support for me in the past six years.

Last but not least, I would like to thank Chris Kong for his support. We have had many life-changing events and have sacrificed much to reach this point together. The best is yet to come. More than everything, I would like to thank my loving and supportive parents, Jianyun Li and Xiaomei Wu. They have always made me laugh, and throughout all the ups and downs, there was always a beacon of light in my life. I love you both with all my heart.

Chapter 1. INTRODUCTION

1.1 IMPORTANCE OF BATTERIES

It is universally recognized that the abusive use of fossil fuels and biomass not only causes air pollutions and accompanied global warming, but also generates national vulnerabilities that endanger social stability due to the strong dependence on foreign fuels. It is therefore necessary to shift electricity and heat production from traditional fossil fuels to sustainable energy sources and move transportation towards electrical propulsion with no harmful exhaust.

Most sustainable energy sources such as solar radiation, wind, hydroelectric, and wave powers are variable in time and diffuse in space. To make the usage of sustainable energy sources use reliable and cost-effective, the energy storage and conversion technology is of extreme importance.[1] The energy carriers include stationary electricity grid, electromagnetic waves, and chemical energy. The most convenient and high-density form of energy storage is as chemical energy, which is why the nations are so addicted to fossil fuels.

In addition to the fossil fuels, rechargeable battery is also a viable and portable chemical energy carrier, and a promising alternative to fossil fuels. A rechargeable battery has the ability to store and release the electrical energy produced by the sustainable energy with a high conversion efficiency and no gaseous exhaust. Although impressive progress in recent years has been seen in the development of technologies for harvesting sustainable energy, *e.g.,* better wind turbines and photovoltaic cells,[2,3] the development of energy storage and conversion devices, *e.g.,* the rechargeable batteries, is still lagging far behind. Hence, to move away from fossil fuels, we need to develop low-cost, safe, rechargeable batteries that can store sustainable energy with long-term stability and prolonged cycle life, and meet the environmental constraints. This has been proven to be extremely challenging for modern electrochemistry.

1.2 GENERAL DEFINITIONS OF BATTERIES

Batteries are electrically connected electrochemical cells having terminals/contacts to supply electrical energy. Upon discharge, they are referred to as galvanic cells, given that they are converting chemical energy into electric energy. When charging, the batteries switch to electrolytic cells where electric energy is converted to chemical energy.

Primary batteries are those in which the chemical processes are not reversible. Once discharged, they cannot be charged again for re-use. In contrast, the reactions in a rechargeable battery can be driven in reverse, allowing for multiple charge/discharge cycles.

1.2.1 *Basic Components of Batteries*

The basic structure of a battery cell is shown in Figure 1.1.[4] The negative and positive electrodes are separated by an ionically conductive but electrically insulating electrolyte. Each electrode undergoes a half-cell reaction, which can be added to give the overall reaction of the cell. The first LIB ($LiCoO_2/Li^+$ electrolyte/graphite) is shown as an example of the half-reactions in Figure 1.1. These half-reactions on the electrodes produce a flow of electrons in the external circuit that is balanced by the migration of ions through the electrolyte and into the electrodes.

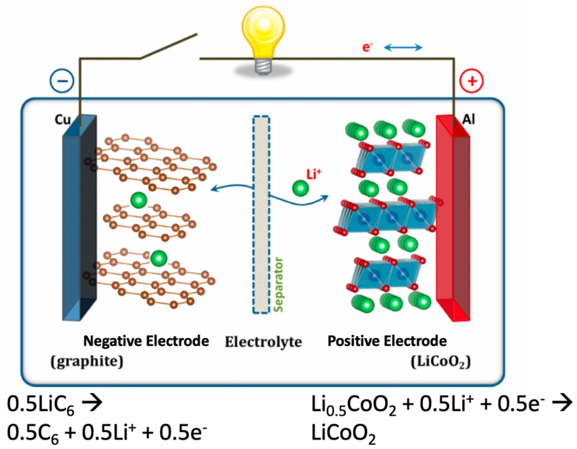

Figure 1.1. Schematic of an electrochemical cell with half reaction examples and all chemically inactive components including current collectors (Cu and Al), electrolyte, separator, etc.[4]

The two electrodes with different half-cell reactions have different electric potentials. Connecting the positive and negative electrodes causes a driving force for charge transfer resulting from the potential difference. The driving force is called the electromotive force, open-circuit voltage (OCV, Voc), or emf, and it is measured in volts (V). The negative electrode is the electrode with lower electric potential (more negative), and the positive electrode has higher electric potential (more positive), as shown in Figure 1.2.[1]

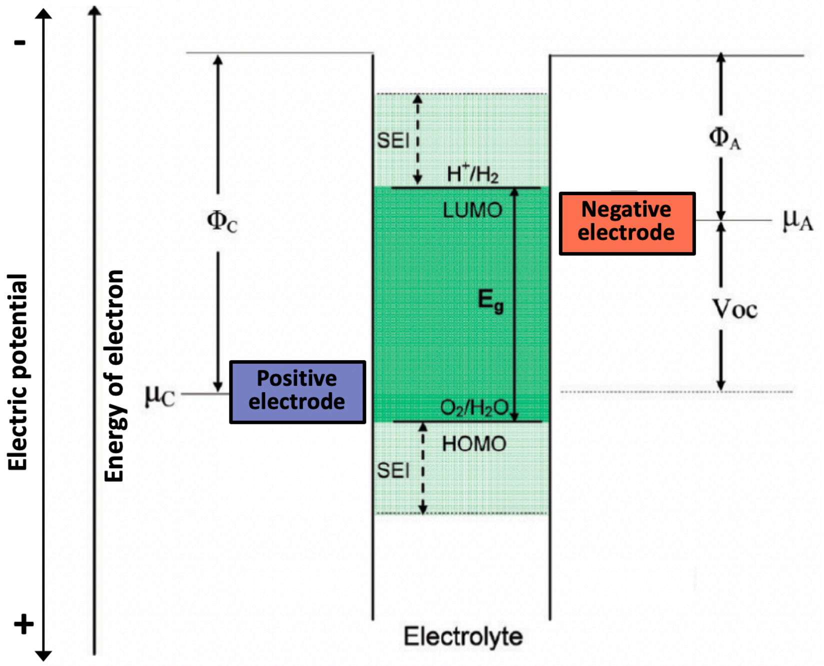

Figure 1.2. Schematic open-circuit energy diagram of a typical battery system. μ_A and μ_C are the anode (negative electrode) and cathode (positive electrode) electric potential (their Fermi energies ε_F), respectively. Φ_A and Φ_C are the anode and cathode work functions, respectively. E_g is the window of the electrolyte for thermodynamic stability. A μ_A > LUMO and/or μ_C < HOMO requires a kinetic stability by the formation of an solid electrolyte interphase (SEI) layer.[1]

During discharge, the negative electrode attempts to push electrons around the external circuit towards the positive electrode. The oxidation or anodic reactions occur at the negative electrode named the anode, and the reduction or cathodic reactions occur at the positive electrode known as the cathode. Conversely, during charge, a lower electric potential is applied to the negative electrode via an external voltage source, while a higher electric potential is applied to the positive electrolyte. This forces electrons towards the negative electrode which means that during charge the reduction or cathodic reaction takes place at the negative electrode and oxidation or anodic reaction takes place at the positive electrode.5 The definition of positive/negative electrode and cathode/anode is summarized in

Table 1.1. In the battery research community, the discharge process is taken as the formal standard process; hence the positive electrode during discharge is consistently referred to as the cathode, even though it undergoes an anodic reaction during charge.

Table 1.1. Definition of cell electrodes

		Battery community
Electrode	**Charge**	**Discharge**
Positive	**Anode**	**Cathode**
Negative	**Cathode**	**Anode**

1.2.2 *Voltage, Current, Capacity, Energy Density, and Power*

Operational voltage is different from OCV for a battery. The operation voltage is the one at which the cell operates during discharge and is lower than the OCV because the passage of current induces overpotential (*e.g.,* the surface overpotential and the concentration overpotential) and ohmic potential drop.[5] This overvoltage and ohmic voltage drop are caused by the internal ionic or electrical resistance, electrical double layers at the particle's interface, rate of reactions, mass transfer, and diffusion rate, among others.

The current in a battery is closely related to the rate of electrochemical reactions. Charge and discharge rates of a battery are governed by the C-rate. A 1C rate means that the discharge current will discharge the entire fully-charged battery in 1 hour. A C/5 rate corresponds to the current required to fully discharge (or charge) a battery in 5 hours.[6]

Capacity is a term generally used to convey how much electricity could be released when a battery is discharged from 100% state-of-charged to the cut-off voltage in a certain amount of time. Practically, the unit to measure the amount of electricity is expressed in ampere-hour (Ah), or mAh for smaller batteries.[6] The theoretical capacity is the amount of electricity theoretically available in the active material and is expressed in a unit of mAh g^{-1}. Effective/real/practical capacity is the amount of electricity released by a fully charged battery. A battery is out of service, or at the end of its lifetime, when its capacity irreversibly drops below 80% of the nominal value, regardless of the reason.

Energy density is the amount of energy in watts-hour (Wh) stored per unit weight (Wh kg^{-1}), or unit volume (Wh m^{-3}).[6] It determines the battery weight/size required to achieve a given electric range. For power batteries, gravimetric power density is the maximum available power per unit, given in units of W kg^{-1}, and volumetric power density in W m^{-3}. It determines the battery weight/size required to achieve a given power performance target.

1.3 DEVELOPMENT OF STATE-OF-THE-ART RECHARGEABLE BATTERIES

1.3.1 *Applications: Storage, Energy, and Power*

To date, the development of battery technology is prosperous. It seems clear that there will not only be a single battery technology for all applications (technology monopoly), but rather different battery systems can be suitable or combined for various applications (technology diversity). In general, state-of-the-art rechargeable batteries are primarily utilized in three applications, including storage, energy, and power.

Storage batteries are those used to store and convert electricity to overcome the mismatch between generation and end-use and improve renewable energy integration in the grid.[7,8] They can also efficiently increase the value of electric power by correcting for power fluctuations in a very short time. A storage battery could be analog to a cheap and large tank of water from which water needs to be dumped into and out of quickly and repeatedly with little maintenance required. For a good storage battery, low cost, high cycling stability, and fast response-balancing systems for frequency regulation are more of a concern than weight.[8–10] Today a large number of different types of the storage battery with different characteristics are available. The available systems range from short-term (seconds to minutes) to long-term (hours and days) storage, such as the vanadium redox (VR) and lead-acid (L/A) batteries (Figure 1.3).[11] Installations using VR to create long term storage has been successfully implemented in Utah (US) on a small scale (259 kW for 8 hours) to manage peak flows in the distribution feeder.[12] Another project is to manage the wind farm in the San Gorgonio area of California (US) with a massive installation of 2.88 MW and 17.28 MWh lead-acid batteries.[13]

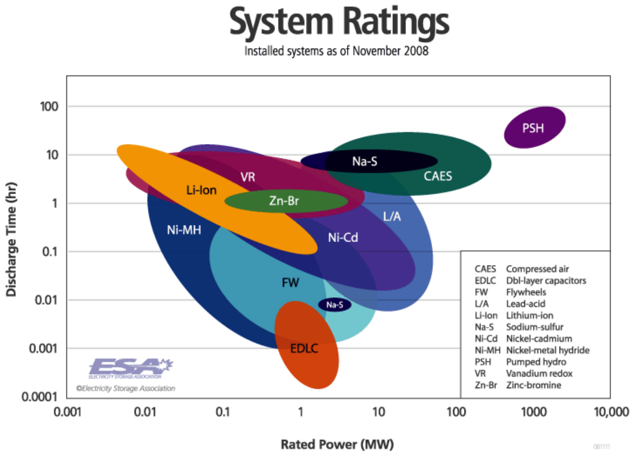

Figure 1.3. Storage system ratings.[11]

Energy batteries are aimed at supplying mobile consumer electronics such as mobile phones, cameras, laptops, and electric cars. They are meant to deliver electric energy over extended periods; a dense electrode with a small space and a light weight tends to be a priority. The characteristics of a successful energy battery include high energy density with high Coulombic and energy efficiencies, low cost, and high safety performance with high reliability. Today, LIBs are widely employed in the consumer electronics due to their relatively high energy density (Figure 1.4), which substantially replaces lead-acid and nickel-metal hydride batteries in the market.[14] The specific energy of LIBs, that increased from ~ 90 Wh kg^{-1} cell in the 1990s to over 250 Wh kg^{-1} cell today,[15] has allowed full-size automobiles to travel sufficient distances for typical driving patterns.[16] In the meantime, the cost of Li-ion battery packs has decreased from over 1,000 US$ per kWh to ~ 250 US$ per kWh.[17,18]

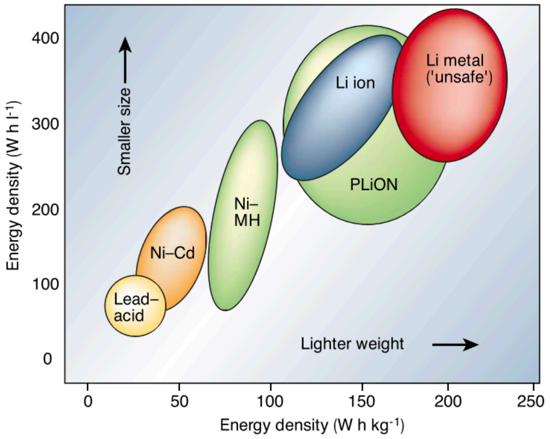

Figure 1.4. Comparison of the battery systems in terms of volumetric and gravimetric energy density(2001).[14]

Power batteries are expected to provide a large amount of current in very little time, which are widely used in medical devices, safety/lifejacket lights, motive powers, telecoms, and surveillances. Electrodes for power applications tend to possess small particle size and large electrode surface area, allowing the charged species to move quickly through the battery. In real life, lead-acid batteries are utilized as starter batteries for cars and back-up power supplies;[19] nickel-cadmium batteries are applied to the emergency lighting;[20] Ni/MH batteries meet the need of a Bentone Blitz-type senior racing motor for accelerating from 0 to 100 Km h^{-1} within 6s;[21] LIBs are also adopted in hybrid EV to provide a sufficient amount of power for acceleration.[22]

1.3.2 *Modern Li-Ion Batteries for Various Applications*

Among all booming battery technologies, hitherto LIBs become the most successful battery technique. They have attracted massive attention due to the high energy density, good performance, and long cycling life compared to the conventional Ni-H, Ni-Cd, and lead-acid batteries. Currently, they not only dominate the small format battery market for portable electronic devices, but have also have been successfully implemented as the technology for stationary energy storages as well as for EVs.[23–25] The drastically growing demand for LIBs during the past few decades has stimulated enormous investigations on the development of novel LIBs to fulfill their potential in different scenarios.

The present-day market for LIBs is far more complicated than the original small electronic devices, as summarized in Table 1.2.[25,26] Nowadays, Graphite/$LiCoO_2$ (C/LCO) occupies the main market of smaller portable electronics. $Li_4Ti_5O_{12}$/$LiMn_2O_4$ (LTO/LMO) with good power capability is excellent for high power applications such as power tools. The use of Graphite/$LiNi_xMn_yCo_{1-x-y}O_2$ (C/NMC) and Si-C or C/$LiNi_{0.8}Co_{0.15}O_2$ (Si-C or C/NCA) is rapidly growing for the EVs due to its exceptional combination of properties (energy, power, and cycle life). Additionally, Graphite /$LeFePO_4$ (C/LFP) is suitable for stationary energy storage owing to its excellent cycle life.

Table 1.2 Properties of various LIBs and their advantages, disadvantages, and applications (2017).[25,26]

LIBs	Midpoint voltage vs. Li (C/20)	Specific Capacity (Ah/kg)	Advantages	Disadvantages	Applications
C/LCO	3.9	155	Good cycle life, good energy	Moderate thermal stability	Smaller portable electronics
LTO/LMO	4.0	100-120	Very good power capability, very good thermal stability, inexpensive	Moderate cycle life, lower energy	High power applications such as power tools

Si-C/NCA or C/NCA	3.7	180	Very good energy, good power capability, good cycle life	Sensitive to moisture, moderate thermal stability	Excellent for motive power and premium electronic applications
C/NMC	3.8	160	Very good combination of properties (energy, power, cycle life and thermal stability)	Patent issues	Electric vehicles
C/LFP	3.4	160	Very good cycle life, good power capability, very good thermal stability	Lower energy, special preparation conditions	Energy storage applications

1.3.3 *Demand of New-Generation Batteries Beyond Li-Ion*

As mentioned above, LIBs have created significant changes in modern life. Even though the most promising modern LIBs hold more than twice as much energy by weight as the first commercial versions sold by Sony in 1991 and are four times cheaper, they are still far from the criteria of ideal batteries.

For instance, in EV applications, the cost element is particularly important. Recent estimates place the cost of producing a LIB battery pack being as low as $190-250 per kWh,[27] while the goal of most auto-manufacturers and the US Department of Energy is $125 per kWh for a battery pack.[28] Besides, it is worth to notice that only the costly Tesla models have 200 or more miles in range.[25,26] Such a high vehicle range with a low price is currently hard to accomplish for LIBs.[29,30]

The second area of major applications of batteries is that of energy storage in connection with stabilization and storage for the electric grid. Many storage devices involve LIBs because of the long cycle life and calendar life, but the safety and cost issues inside stationary LIBs need to be further considered.[17]

Therefore, to approach the criteria and further exploit the ideal battery devices for particular applications, researchers need to take a leap beyond the Li-ion technology by changing the electrodes, the electrolyte, and the charge-carry ions, such as Li/S, Li/O, and multivalent-ion batteries.

1.4 FUNDAMENTAL STUDY OF LOW-COST ALTERNATIVE CANDIDATES BEYOND LIBS

In this section, we will introduce two attractive battery candidates beyond LIBs, Zn/MnO_2 and Li/S batteries, which are expected to achieve cost competitiveness with LIBs in the storage and energy battery markets, respectively.

1.4.1 *Zn/MnO_2 Batteries for Large-Scale Stationary Grid Storage*

Although LIBs possess significantly high energy density, many factors (cost, safety, lifetime, eco-friendliness) will likely limit their large-scale applications and dictate against their use in stationary grid storage, where low cost, durability, and fast response-balancing systems for frequency regulation are more of a concern than weight.[31–33] Figure 1.5 compares the lifetime investment cost and other characteristics of storage batteries that are appropriate for large-scale stationary energy storage.[34,35] Redox flow (V-redox), sodium-sulfur, lead-acid, LIBs, etc., have been proposed as possible systems for large-scale stationary energy storage, but they also suffer from poor energy-to-volume ratio, low charging rates, high operating temperatures, the use of hazardous materials in their components, and/or high costs.[7] These drawbacks limit their integration into the large-scale electric grid.[36] Batteries based on multivalent-ion, especially Zn^{2+} aqueous rechargeable batteries (*e.g.,* Zn/MnO_2), which utilize low-cost and safe water-based electrolytes, are promising alternatives.[34,37–43] They not only deliver comparable high energy density to those of LIBs at fast discharge/charge rate, but also show the advantage of abundant and environmentally benign constituents and excellent safety.

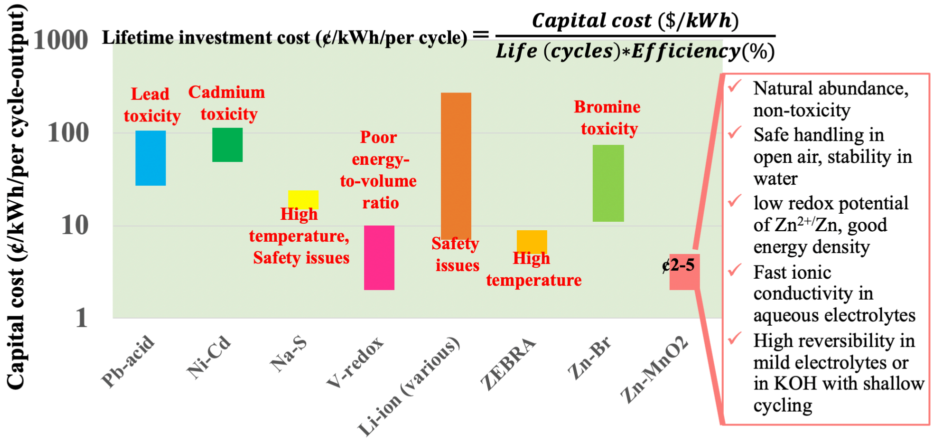

Figure 1.5. Comparison of storage batteries for large-scale energy storage applications. Lifetime investment cost range was calculated from cycle life and capital cost ranges taken from Ref.34, 35.

In spite of their low cost and high safety, cycling stability becomes a major obstacle for the practical application of Zn/MnO_2 systems. The ambiguities of the reaction mechanism makes it hard to determine and control the effect on the capacity fade in Zn/MnO_2. During the discharge/charge processes, it is not a trivial task to discern the contribution of proton and Zn^{2+} ions to the reaction mechanisms. On the experimental side, X-ray diffraction (XRD) data leave controversies of the structural changes of MnO_2 due to the overlapping diffraction peaks and the low crystallinity for many possible reaction products,[44–48] which are very sensitive to the local pH value, humidity, temperature, etc.[49,50] In addition to XRD, nuclear magnetic resonance (NMR) or high-resolution transmission electron microscopy (TEM) only offers localized structure, composition, and chemical environment information without macroscopic and quantitative analysis.[43,45,46,51] Therefore, a comprehensive approach needs to be called for to elucidate the reaction mechanisms, identify the origin of capacity fading, and design high-performance ZIBs. More details about the Zn/MnO_2 system will be discussed in Chapter 2.

1.4.2 *Li/S Batteries for Supplying Electric Vehicles*

Referred as the Beyond 2 Degrees Scenario (B2DS), the cumulative EV sales and EV market share need to increase to 1.8 billion and 86% by 2060,[52] respectively, while the values were 2 million and 0.2% in 2016 as reported.[53] It is now certain that EVs powered by LIBs will not be suitable for the future vehicle market, owing to inherent limits in their energy storage capacity, achievable cost, and safety. Alternative technologies with substantially improved specific energy without increasing cost are therefore an important focus. One tantalizing solution could be to look towards the Li/S batteries. This battery chemistry has been widely studied due to its multitude of favorable characteristics. Reduction of sulfur to form Li_2S produces a theoretical gravimetric specific capacity of 1673 mAh g^{-1} at ~2 V vs. Li/Li^+, rendering a theoretical cathode energy density improvement of 500% as compared to the LIBs. This increase can be matched on the anode side by using lithium metal, which possesses an intrinsic theoretical gravimetric specific capacity of 3860 mAh g^{-1} – an order of magnitude higher than that of graphite. Additionally, sulfur is lower cost and earth-abundant, making this redox couple highly attractive for EV battery usage.

Figure 1.6 displays the approximate cost of a vehicle as well as the cost of additional range of a vehicle.[54] It is apparent that the minimum cost for Li/S batteries would be a considerable improvement over LIBs, making them attractive for the emerging EV markets.

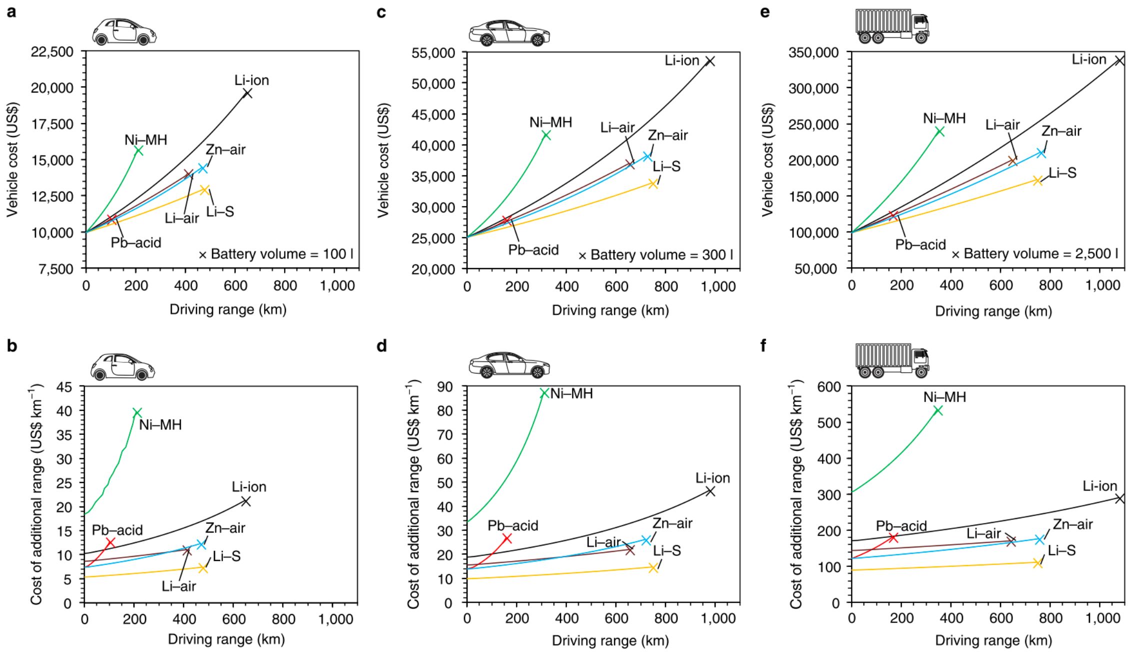

Figure 1.6. Vehicle cost and cost of additional range as a function of driving range. Curves are plotted for (a,b) mini vehicle, (c,d) mid-size vehicle and (e,f) semi-trailer truck.[54]

However, a commercially-viable Li/S has remained elusive due to a bevy of failure mechanisms upon cycling. Many of the failures stem from the formation of lithium polysulfides (Li_2S_x, $3 \leq x \leq 8$) through a multistep reduction process prior to forming Li_2S and Li_2S_2. These LiPSs are highly soluble in organic electrolytes, leading to self-discharge, passivation of the lithium anode, low Coulombic efficiency due to the escape of sulfur into the electrolyte, and voltage hysteresis from differences in the forward and backward reaction mechanisms.[55] In addition to the problems posed by LiPS formation, both the starting material (sulfur) and end products (Li_2S, Li_2S_2) are highly insulating, and lithium metal tends to form dendrites upon repeated stripping and plating.[55]

Researchers have addressed these issues, with a certain degree of success, using a variety of creative strategies. Because of the susceptibility of organic carbonates to nucleophilic attack by LiPSs, etheric solvents are standard, usually a combination of 1,3-dioxolane (DOL) and dimethoxyethane (DME) with lithium bis(trifluoromethane)sulfonimide (LiTFSI) salt.[56] Film-forming additives such as $LiNO_3$ are often used in electrolytes as well in order to form a preemptive passivation film on the Li metal and prevent its reaction with the dissolved LiPSs.[57] One of the most successful strategies to prevent LiPS-related problems has been to melt sulfur into the pores of a mesoporous carbon host, which both increases conductive surface area and hinders dissolved LiPSs from escaping into the "bulk" electrolyte.[58] Another recent success has been to introduce polymer coatings with higher affinity for LiPSs.[59,60] Yet, despite these myriad strategies, a safe Li/S battery with long cycle life based on scalable fabrication techniques remains difficult, as not a single methode of improvement has proven to be totally effective at stopping efficiency/capacity losses via LiPSs. Besides, it is also quite challenging to identify the specific role of individual species in cell function owing to the complexity in characterizing amorphous structures and versatile ionic species, which aggravates the difficulties in investigating effective strategies for LiPS trapping.[61]

With all the challenges in mind, a light-weight sulfur host material with good electrical conductivity and improved wettability to the electrolyte, that not only confines LiPSs physically but also contains a very high accessible fraction of LiPS chemisorption sites, should be an effective approach to realize long-life Li/S batteries. At the same time, fundamental insight on the reaction mechanisms with LiPSs needs to be investigated to suggest a further rational design of the Li/S system to achieve better Li/S performance. More details about the Li/S batteries will be discussed in Chapter 3.

1.5 THESIS OBJECTIVES AND OVERVIEW OF CHAPTERS

As has been reviewed, Zn/MnO_2 and Li/S batteries are regarded as the promising candidates for the next-generation beyond LIBs, which can be utilized in stationary energy storage and EVs, respectively. The existing obstacles in the commercialization of these batteries are divided into two categories: (1) the ambiguities of reaction mechanisms and capacity fading in Zn/MnO_2, and (2) the challenges to suppress the loss of soluble active materials and unveil the trapping mechanisms after surface modification in Li/S batteries. As such, the thesis objectives are to unravel the reaction mechanisms, identify the origin of capacity fading, and design high-performance Zn/MnO_2; and to demonstrate an optimal cathode host for LiPS trapping, identify the modified reaction mechanisms of the LiPSs after the cathode modification, and ultimately succeed to improve the cycling performance of Li/S.

Overall, this thesis consists of four chapters.

Chapter 1 presents a comprehensive introduction to the importance and definition of batteries; the applications of batteries focusing on three fields: storage, energy, and power; the current research status and challenges in state-of-the-art LIBs; and the recommended low-cost alternative candidates to LIBs for achieving mass-market penetration of batteries in the fields of stationary grid and EVs.

Chapter 2 describes the study and implementation of in-situ Zn/MnO_2 system. This promising battery with a mild $ZnSO_4$ electrolyte enables the co-intercalation and conversion of H^+/Zn^{2+}. The understanding of the co-intercalation and conversion reaction mechanisms was previously impossible due to the lack of a coupled experimental and computational analyses. A significant performance improvement of Zn/MnO_2 was achieved after comprehending the origin of capacity fade, which is closely relevant to the reaction mechanisms.

Chapter 3 focuses on anchoring thiol (SH-) functional groups to the non-polar surface of a mesoporous carbon host (MJ430). This new strategy increases the surface polarity of conductive carbon and significantly confines soluble LiPSs inside the cathode. Systematic studies have been carried out to understand the mechanisms of LiPS trapping. This is the first time to realize multiple performance enhancements from a single functional group.

Chapters 4 summarizes the results and contributions of this work and provide an outlook and future work on further improvement of the performance of Zn/MnO_2 and Li/S batteries.

Chapter 2. REACTION MECHANISMS FOR LONG-LIFE REACHARGEABLE ZN/MNO2 BATTERIES*

2.1 INTRODUCTION OF ZN/MNO2 FOR LARGE-SCALE STATIONARY GRID

Large-scale grid storage technology is critical for managing peak demands, improving the grid reliability, integrating most of the sustainable energy sources such as solar radiation, wind and wave power, geothermal energy, etc., and further powering the energy infrastructures.[7,8] For large-scale stationary grid storage, low cost, durability, and high-power capability for frequent peak clipping and valley filling usually outweigh the energy densities.[8–10] Redox flow, sodium sulfur, and lead carbon chemistries have been proposed as alternative battery systems, but they also suffer from issues such as low rates, high operating temperatures, hazardous constituents, high costs, etc.[63–65] Low-cost aqueous batteries with earth-abundant working ions, including various multivalent intercalation batteries (e.g., Zn, Ca, Mg, etc.), are more promising.[66–69]

2.1.1 *Alkaline vs. Mild Zn/MnO2 System*

Among these, aqueous ZIBs with mild electrolytes have the advantages of high energy density (~300 Wh kg^{-1}); low-cost constituent materials (e.g., Zn/MnO_2), manufacturing (air- and water-inert Zn anode), recycling (mild electrolytes); and excellent safety, making them prospective batteries for large-scale grid storage.[34,42,43]

---

* This chapter is reproduced from the article, Li, Y. et al. “Reaction Mechanisms for Long-Life Rechargeable Zn/MnO_2 Batteries.” *Chem. Mater. 2019*, **31**, 2036-2047.[62] Copyright (2019) American Chemical Society. This is an unofficial adaptation of the article that appeared in an ACS publication. ACS has not endorsed the content of this adaptation or the context of its use.

The major limitation of aqueous Zn/MnO_2 for grid storage, however, is the poor cycle stability. Aqueous Zn/MnO_2 system is the prototypical primary alkaline battery with KOH as the electrolyte.[70,71] A wide range of failure mechanisms largely prevent their effective use as the secondary batteries, such as the irreversible production of ZnO, the formation of black hard and non-porous layer of Zn, and the evolution of hydrogen occurring on the Zn anode.[72]

To improve the reversibility, mild electrolytes with neutral pH (5~7) have been studied to replace the alkaline KOH and thus to mitigate the failure mechanisms on the Zn anode (Figure 2.1).

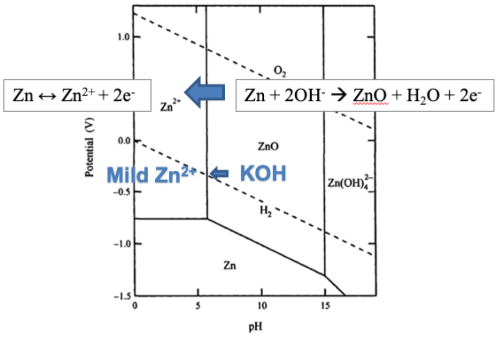

Figure 2.1. Simplified Pourbaix diagram of potential *vs.* pH for Zn at 1 mol kg^{-1} concentration of Zn^{2+} and $Zn(OH)_4^{2-}$. For reference, the dashed lines for the evolution of O_2 and H_2 indicate the limits of stability of water.

In the past thirty years, versatile mild electrolytes, *e.g.,* $ZnSO_4$, $Zn(NO_3)_2$, $ZnCl_2$, $ZnBF_4$, $ZnSiF_6$, and $Zn(CF_3SO_3)_2$ salts have been studied.[42,73] According to the results, $ZnSO_4$ or $Zn(CF_3SO_3)_2$ electrolytes with Mn^{2+} additives significantly improve the cycling performance (Figure 2.2).[42]

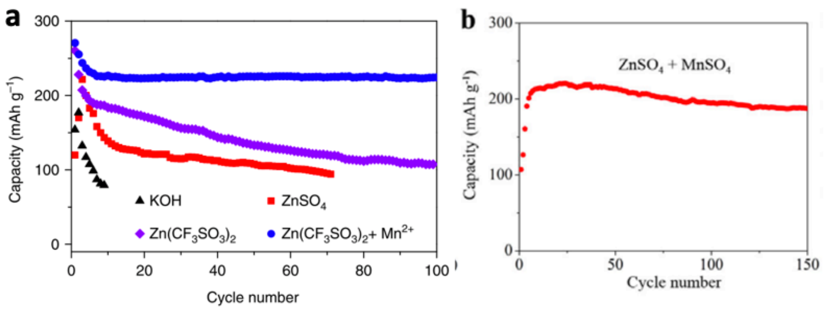

Figure 2.2. Comparison of the cycling performance of Zn/β-MnO_2 cells with electrolytes of (a) 45wt.% KOH, 3 M $ZnSO_4$, 3 M $Zn(CF_3SO_3)_2$, 3 M $Zn(CF_3SO_3)_2$ with 0.1 M $Mn(CF_3SO_3)_2$, and (b) 3 M $ZnSO_4$ with 0.1 M $MnSO_4$.[42]

2.1.2 *Different MnO_2 Morphologies*

In addition to the electrolyte chemistry, the morphology of MnO_2 would also affect the electrochemical performance and cycle stability of Zn/MnO_2 batteries. Zn/MnO_2 can employ many polymorphic MnO_2, including the α-, β-, γ-, λ-, δ-, ε-, and todorokite- MnO_2, the structures of which are shown in Figure 2.3.

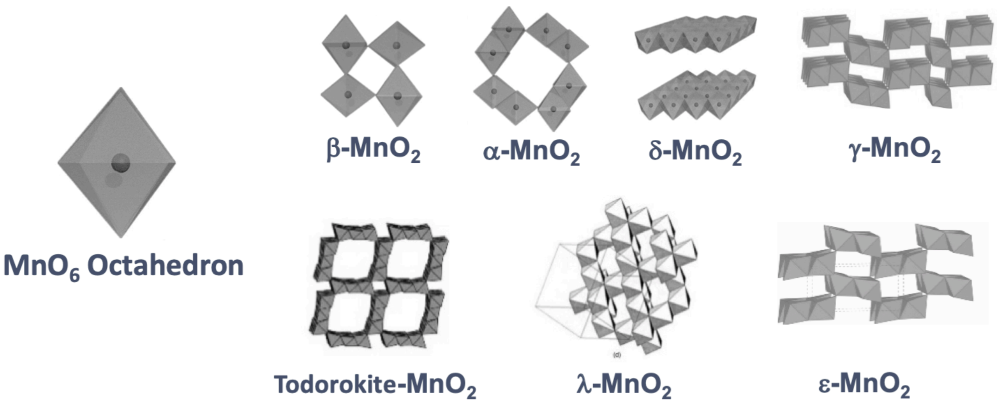

Figure 2.3. Structures of α-, β-, γ-, λ-, δ-, ε-, and todorokite- MnO_2.

Interestingly, the discharge/charge curves of the Zn/MnO_2 cells with different polymorphic MnO_2 are similar. They all consist of two discharge plateaus at ~ 1.40 and ~ 1.26 V, as shown in Figure 2.4.[42,43,46,74,75] However, the proposed explanation of the reactions occurring at these discharge plateaus are incredibly diverged in the literature, which will be discussed in the following Section 2.1.3.

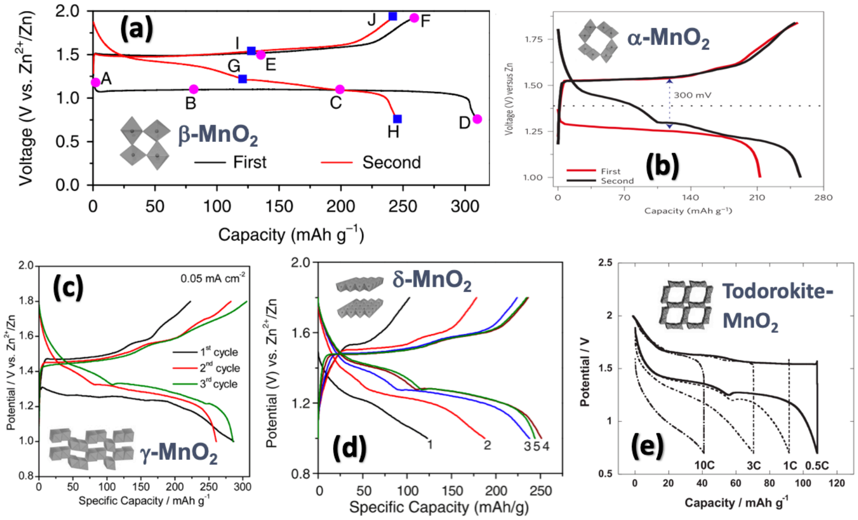

Figure 2.4. Typical discharge/charge curves of (a) Zn/3M Zn(CF$_3$SO$_3$)$_2$/β-MnO$_2$,[42] (b) Zn/2M ZnSO$_4$/α-MnO$_2$,[43] (c) Zn/1M ZnSO$_4$/γ-MnO$_2$,[46] (d) Zn/3M ZnSO$_4$/δ-MnO$_2$,[74] and (e) Zn/1M ZnSO$_4$/todoroskite-MnO$_2$.[75]

2.1.3 *Proposed Reaction Mechanisms of Zn/MnO$_2$ with Different morphologic MnO$_2$*

In 2010, by using nanostructured α-MnO$_2$ as the cathode active material, Xu et al. investigated the aqueous ZIB using mild ZnSO$_4$ as the electrolyte, demonstrating an intercalation reaction of Zn^{2+} into MnO$_2$ (Figure 2.5a).[44] A similar study of the α-MnO$_2$ has been reported by Pan et al.,[43] yet, a distinct conversion reaction involving H$^+$ in the cathodic reactions was suggested (Figure 2.5d), analogous to the argument of Shoji et al. and Kim et al with the γ-MnO$_2$ (Figure 2.5b).[4776] In contrast, the γ-MnO$_2$ was reported to be converted to the spinel ZnMn$_2$O$_4$ and the tunnel-/layered-Zn$_x$MnO$_2$ with Zn^{2+} instead of H$^+$ during discharge, by Alfaruqi et al. (Figure 2.5f)[46], and Lee et al.[45] Zhang et al.[42] also proposed sole Zn^{2+} conversion and insertion reactions occurring in the α-

MnO_2 and β-MnO_2 (Figure 2.5e). Recently, Sun et al.[77] and Zhao et al.[78] designed in situ ZIBs to study the reaction mechanisms in the Zn/MnO_2 systems. Regardless of the similarity of their in situ ZIBs, Sun et al. proposed that H^+- and Zn^{2+}-involved reactions occur at the two separate discharge plateaus in the ε-MnO_2 (Figure 2.5c), [77] yet Zhao et al. suggested only Zn^{2+}-involved conversion reactions at both discharge plateaus.[78] These different reaction pathways of MnO_2 cathode have been summarized in Figure 2.5.[42–44,46,47,77]

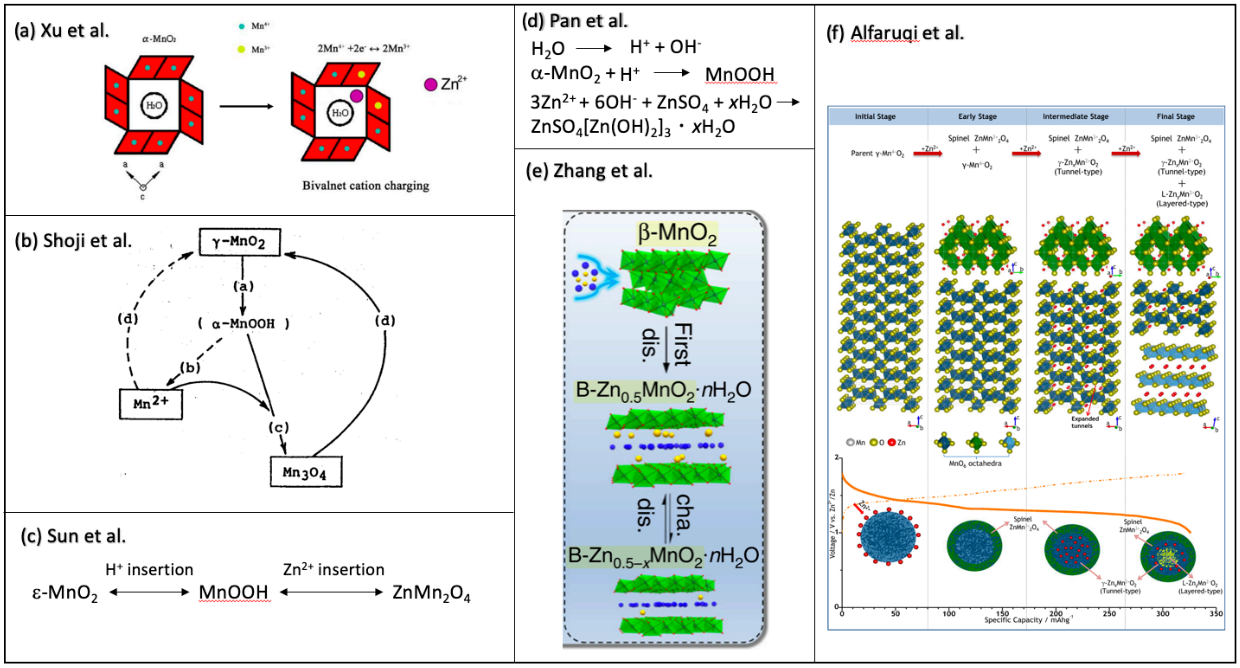

Figure 2.5. The reported reaction pathways of MnO_2 cathode. (a) Zn^{2+} insertion in the α-MnO_2 with 1 M $ZnSO_4$,[44] (b) H^+ conversion in the γ-MnO_2 with 2 M $ZnSO_4$,[47] (c) H^+/Zn^{2+} insertion in the ε-MnO_2 with 2 M $ZnSO_4$+0.2 M $MnSO_4$,[77] (d) H^+ conversion in the α-MnO_2 with 2 M $ZnSO_4$,[43] (e) Zn^{2+} conversion in the β-MnO_2 with 3 M $Zn(CF_3SO_3)_2$ + 0.1 M $MnSO_4$,[42] and (f) Zn^{2+} conversion/insertion in the γ-MnO_2 with 2 M $ZnSO_4$.[46]

In short, despite all of these prior efforts, the exact roles of H^+ and Zn^{2+} in the two discharge plateaus and the kinetics of the redox reactions still remain controversial and uncertain, which need to be unambiguously revealed to further optimize the cycle life of the Zn/MnO_2 systems.

2.1.4 *Challenges and Contradictions for the Study of Reaction Mechanisms*

In Zn/MnO_2 batteries, however, accurately determining the reaction products and mechanisms, especially under different rates, poses a grand challenge. On the experimental side, X-ray diffraction (XRD) data leave ambiguities and controversies due to the overlapping diffraction peaks and the low crystallinity for many possible reaction products, especially the ones containing Mn,[44–48] which are very sensitive to the local pH value, humidity, temperature, etc.[49,50]

In addition to XRD, nuclear magnetic resonance (NMR) or high-resolution transmission electron microscopy could offer localized structure, composition, and chemical environment information,[43,45,46,51] but the macroscopic and quantitative analysis is challenging. These difficult issues severely impede the study on the structural change of MnO_2 not only in rechargeable ZIBs but also in various other aqueous systems such as supercapacitors,[79] electrocatalysts,[80,81] and biomimetic membranes.[82]

In terms of the theoretical efforts, the computational modeling has been hindered by the complexity and a large variety of the reaction products (different phases and compositions) under various rates, which necessitates experimental guidance to reduce the required computational resources.

Therefore, a coupled experimental and computational approach is called for to elucidate the reaction mechanisms, identify the origin of capacity fading, and design high-performance ZIBs, which is the focus of this study. We also expect that the understanding of MnO_2 evolution in ZIBs would concurrently help other MnO_2 studies associated with different ions, water molecules, and natural materials.

2.1.5 *Brief Summary of This Work*

In this combined experimental and computational study, we unravel concomitant and conversion reactions of H^+/Zn^{2+} occurring at different voltages in the Zn/MnO_2 system. The rapid capacity fading is unambiguously ascribed to the irreversible conversion reactions at the lower voltage. More interestingly, the irreversible conversion reactions are also characterized as kinetic-limiting. Therefore, by purposefully cycling cells at higher rates, we successfully limited the irreversible conversion reactions at the lower voltage and demonstrated high-performance Zn/MnO_2 cells that can deliver high energy and power densities of ~300 Wh kg^{-1} and ~2 kW kg^{-1} at 3C (1.032 A g^{-1}), ~231 Wh kg^{-1} and ~4 kW kg^{-1} at 9C (3.096 A g^{-1}), as well as ~105 Wh kg^{-1} and ~15 kW kg^{-1} at 30C (10.32 A g^{-1}), respectively, with negligible capacity fading after 100 (at 3C), 1000 (at 9C), and 1000 (at 30C) cycles. These values are superior to most of the reported ZIBs or even some LIBs. Furthermore, the revealed reaction mechanisms in our in situ electrochemically deposited Zn/MnO_2 cells should be compatible to ex situ Zn/MnO_2 cells or other ZIBs previously reported and thus should be applicable for improving their cycle stability.

2.2 EXPERIMENTAL SECTION

2.2.1 *Materials and Characterization*

The carbon black electrodes for in situ deposited MnO_2 were prepared by thoroughly mixing 45 wt % carbon black (TIMCAL Graphite & Carbon super P, MTI Corporation) and 55 wt % poly(vinylidene fluoride) in Nmethyl-2-pyrrolidone (NMP). The slurries made by a planetary centrifugal mixer (ARE-310, Thinky) were cast on Ni foils by an MC-20 Mini-Coater (Hohsen, Japan). Ni foils with coatings were then dried in vacuum at 100 °C for 6 h to get rid of the NMP solvent. Afterward, MnO_2 was deposited on the carbon black electrodes from a 0.2 M $MnSO_4$ + 1 M $ZnSO_4$ aqueous solution at a current density of 0.01 mA cm^{-2} for 30 h.

Powder XRD data of the cathode materials were collected on a Rigaku RAPID II (Mo Kα radiation, Rigaku, Japan) at room temperature. Microstructures of the samples were determined by a field emission scanning electron microscope equipped with an Oxford energy-dispersive spectroscopy (EDS) (FEI Sirion XL30). The sample chemical compositions were determined by a two-dimensional micro-X-ray fluorescence (micro-XRF) analyzer (M4 TORNADO, Bruker). Inductively coupled plasma (ICP) atomic emission spectroscopy was used to determine the mass loadings of MnO_2 deposits. To investigate the evolution of the Mn oxidation state in the electrodes, soft X-ray absorption spectroscopy (sXAS) data were collected in total electron yield mode in the iRIXS endstation at Beamline 8.0.1 of the Advanced Light Source at Lawrence Berkeley National Laboratory.[83] The experimental resolution of sXAS is about 0.15 eV without considering core hole lifetime broadening. For ex situ XRD, sXAS, scanning electron microscopy (SEM), and XRF studies, the recovered electrodes after electrochemical cycling were rinsed with deionized water and dried overnight at room temperature.

2.2.2 *Electrochemical Test*

Electrochemical tests were carried out in both coin cells and three-electrode open cells. The cathodes were assembled in 2032 type coin cells with selected electrolytes and 0.5 mm thick excess Zn foil as the anode. Glass fiber membrane filters (Whatman) were used as the separators. The electrolyte used is a 0.2 M $MnSO_4$ + 1 M $ZnSO_4$ aqueous solution.[43] The coin cells were cycled galvanostatically between 1.0 and 1.8 V (vs Zn^{2+}/Zn) at 30 °C, using a multifunction model 4200 battery tester (Maccor). Cyclic voltammetry (CV) tests were carried out using a Reference 600 Potentiostat (Gamry) at a scan rate between 0.1 and 1.0 mV s^{-1}. In the CV cells, the cathodes were used as the working electrodes, silver chloride electrodes as the reference electrodes, and Pt foil as the counter electrodes. Electrochemical impedance spectroscopy (EIS) tests were carried out using a VersaSTAT 4 potentiostat (Ametec Scientific Instruments) with a frequency range from 1 MHz to 0.01 Hz and an alternating current amplitude of 5 mV. For each electrochemical test, at least six cells were simultaneously examined to acquire the typical results and the degree of variation.

2.2.3 *First-Principles Calculations*

All calculations in the present study were performed within the generalized gradient approximation (GGA) using the Perdew, Burke, and Ernzerhof (PBE) exchangecorrelation functional.[84] A plane wave basis set and the projector augmented wave method as implemented in the Vienna Ab initio Simulation Package (VASP) were used,[85–88] based on the density functional theory (DFT). Furthermore, to account for the strong onsite Coulombic repulsion of the Mn 3d electrons, the GGA + U method was used for the Mn-containing compounds.[89,90] The effective onsite Coulombic term U_{eff} of the Mn 3d electrons was chosen to be 3.9 eV, according to a previous reference.[91] The theoretical calculations of Zn-inserted MnO_2 were performed in fully relaxed 2 × 2 × 1 supercells, as shown in Figure 2.6. The Monkhorst−Pack scheme 5 ×5 × 2 k-point sampling was used for the integration in the irreducible Brillouin zone.[92] The cutoff energy for the plane waves is set to be 520 eV. The total ground-state energy converged within 10^{-5} eV. The lattice parameters and the ionic position were fully relaxed, and the final forces on all atoms were less than 0.01 eV $Å^{-1}$.

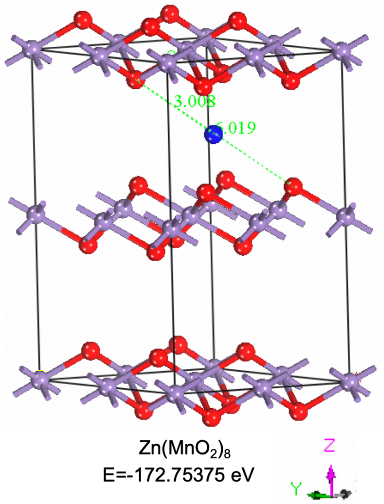

Figure 2.6. Supercells used for calculating the Gibbs free energy of Zn-inserted MnO_2 (Zn in blue, Mn in purple, and O in red).

2.3 RESULTS AND DISCUSSION

2.3.1 *Electrochemical Performance of in Situ Deposited Zn/MnO_2 Cells*

The active MnO_2 cathode materials were electrodeposited in situ from the $MnSO_4$-based electrolyte onto the substrate, which is inspired by the electrodeposition of electrolytic MnO_2 used in the alkaline primary batteries and has been adopted in latest reports.[77,78,93,94] Carbon black was used as the MnO_2 electrodeposition substrate due to its high electrical conductivity, porous structure, and large surface area. To evaluate the energy storage capability of the in situ Zn|$MnSO_4$, $ZnSO_4$|carbon black cells, coin cells were tested in the potential range of 1.0−1.8 V versus Zn^{2+}/Zn (Figure 2.7). Figure 2.7a shows the initial electrodeposition of MnO_2 at a current density of 0.01 mA cm^{-2} for 30 h and the subsequent galvanostatic discharge/charge profiles of the cell at C/3 (C = 0.344 A g^{-1}). The typical loading of MnO_2 deposits is ~0.54 mg cm^{-2} based on the electrodeposition charge, which is consistent with the average loading of ~0.5 mg cm^{-2} derived from the ICP measurements. This loading is similar to the previously reported Zn/MnO_2 cells.[77]

Here, utilizing a low material loading aims at isolating other extrinsic factors such as poor electrical conductivity and limited accessible surface area of the MnO_2 cathode,[95] which might contaminate the electrochemical reactions of Zn/MnO_2 cell and thereby hinder our main focus on the intrinsic reaction mechanisms of Zn/MnO_2.

The initial electrodeposition plateau is at ~1.73 V and the two discharge plateaus are at ~1.40 and ~1.26 V. On the subsequent cycles, new charge plateaus appear at ~1.51 and ~1.58 V. The appearance of 1.40/1.26 V discharge and 1.58/1.51 V charge plateaus was also observed in previous reports, which were assigned as either Zn intercalation or proton conversion reactions associated with the crystallographic evolution of MnO_2 during the cycling processes.[43,46,47,76,96] In this work, we will show that the two discharge plateaus at 1.40 and 1.26 V represent more complicated reactions, which incorporate both H^+ and Zn^{2+} into the MnO_2 host and reduce Mn(4+) into Mn(3+)/Mn(2+).

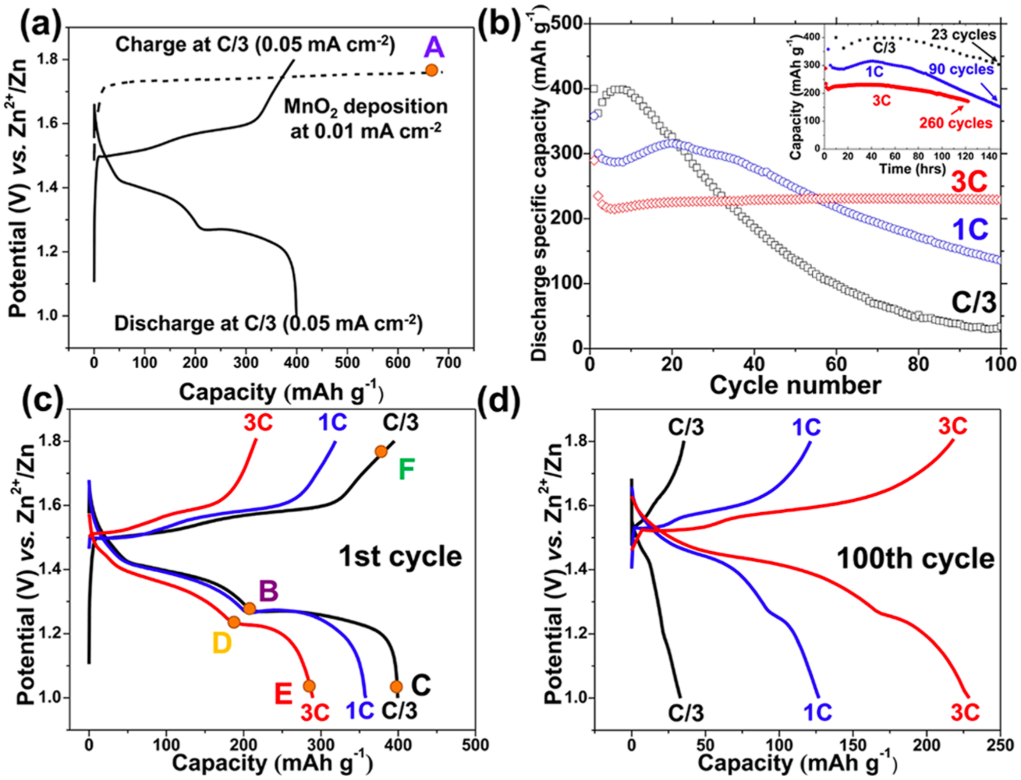

Figure 2.7. Electrochemical behavior of in situ electrochemically deposited Zn/MnO_2 cells. (a) Electrodeposition of MnO_2 and its discharge/charge profiles at C/3 (0.115 A g^{-1}); (b) cycle performance of in situ Zn/MnO_2 cell vs cycle number at different rates (C/3, 1C, and 3C) and their discharge/charge profiles at the (c) 1st cycle and (d) 100th cycle. The inset in (b) is the cyclic data vs time.

The cycling performance at C/3 is shown in Figure 2.7b. The capacity increase in the first few cycles is due to a gradual activation of the deposited MnO_2 (electrolyte wetting, surface stabilization, etc.). After the activation, the cell suffers severe capacity, fading from 400 to 30 mAh g^{-1} within 100 cycles. The poor cycle stability led us to speculate that there might exist irreversible reactions (e.g., conversion reaction or other side reactions) during discharge that cause significant disruption of the original electrode architecture or material crystal structures. Interestingly, the capacity retentions are significantly better at higher discharge/charge rates, as shown in Figure 2.7b, e.g., ∼35 and ∼80% discharge capacity retentions at 1C and 3C after 100 cycles, respectively.

Figure 2.7c shows the initial discharge/charge profiles of the Zn/MnO_2 cells at C/3, 1C, and 3C. Upon close examination of the discharge plateaus, we find that the first discharge plateau at ∼1.40 V shows comparable specific capacities among different rates (∼191 mAh g^{-1} for 3C and ∼212 mAh g^{-1} for C/3), whereas the capacity pertaining to the second discharge plateau at ∼1.26 V decreases significantly from ∼188 mAh g^{-1} at C/3 to ∼108 mAh g^{-1} at 3C. This clearly indicates that these two plateaus have distinctive rate-dependent kinetics such that the electrochemical reactions at 1.26 V are kinetically limited at high rates, whereas those at 1.40 V are only slightly dependent on the rate.

The voltage curves at the 100th cycle are plotted in Figure 2.7d, as such; the discharge/charge profiles for the 100th cycle at the 3C rate show that the cells retain ∼89 and ∼55% of the discharge capacities of the 1.40 and 1.26 V plateaus, respectively. The cell cycled at the 1C rate, however, mostly displays a capacity corresponding to the 1.40 V discharge plateau after 100 cycles. Therefore, these data seem to suggest that the high-capacity retention at high rates is mainly due to the reversible reactions occurring at the 1.40 V discharge plateau as well as the significantly kinetically limited irreversible reactions at 1.26 V. The inset of Figure 2.7b shows the capacity versus time at different rates; the capacity retention versus time is comparable among the three rates. This is reasonable because, even though the capacity losses for the kinetically limited irreversible reactions at 1.26 V are relatively smaller at higher rates, in a given time period, the high-rate (3C) cycling would go through the 1.26 V plateau many more times than that of the low rate (C/3). This behavior is merely a combined effect of capacity losses and the number of times that the cell experiences the irreversible reactions at 1.26 V.

2.3.2 *Redox Reaction Mechanisms*

XRD and XRF. To elucidate the reaction mechanisms in the in situ Zn/MnO_2 cells, the structure and composition of the in situ formed MnO_2 cathode and its evolution during discharge/charge were examined by ex situ XRD and XRF. The XRD pattern was carefully collected for the original MnO_2 deposits (**A** in Figure 2.7a and Figure 2.8a). The originally deposited MnO_2 cathode (**A**) can be indexed to the hexagonal structure birnessite δ-MnO_2 (JCPDS # 18-0802), which can be viewed as a layered MnO_2. The standard XRD pattern of δ-MnO_2 is shown in Figure 2.9. The crystal structure of the birnessite δ-MnO_2 consists of sheets of edge-sharing [$Mn^{4+/3+}O_6$] octahedra with some Mn vacancies and interlayer [$Mn^{3+/2+}O_6$] octahedra located above or below the in-sheet Mn vacancies.[97] The charge of in-sheet Mn vacancies is compensated by the interlayer $Mn^{3+/2+}$ or other cations such as Zn^{2+} and H^+.

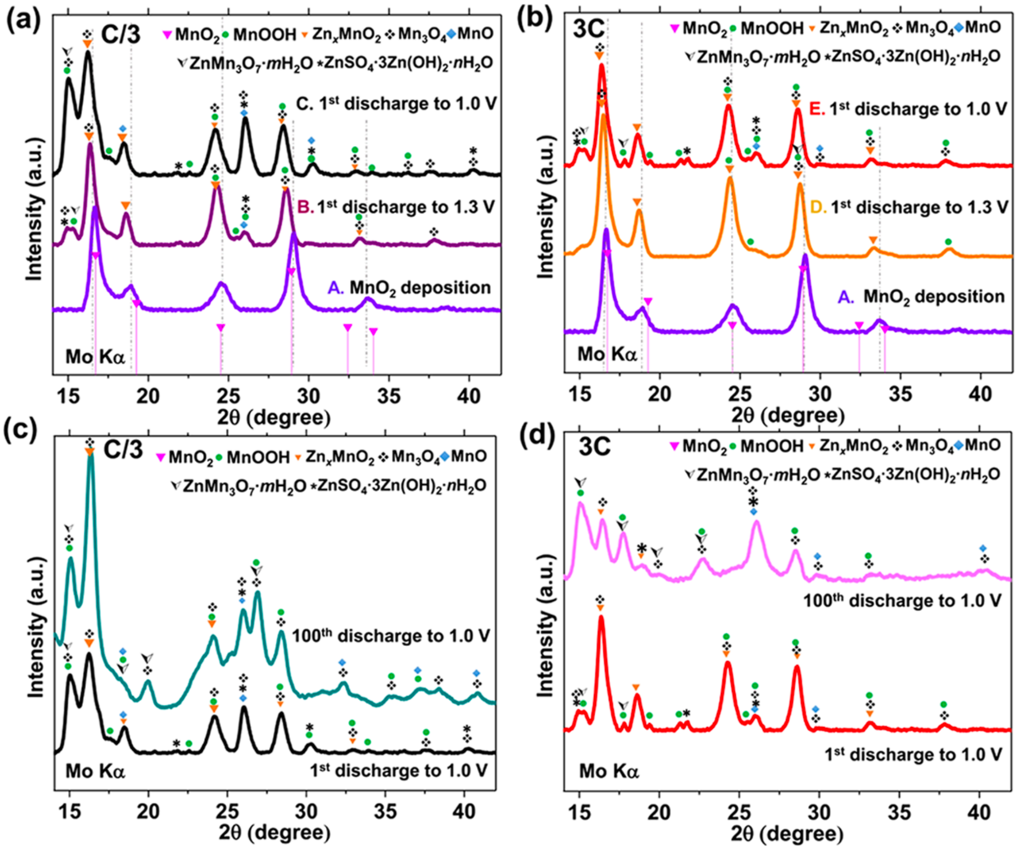

Figure 2.8. Comparison of XRD patterns of MnO_2 electrodes during the electrochemical processes. The initially deposited MnO_2 and the partially and fully discharged cathodes at the current densities of (a) C/3 and (b) 3C. XRD patterns of fully discharged cathodes after the 1st and 100th cycles at (c) C/3 and (d) 3C.

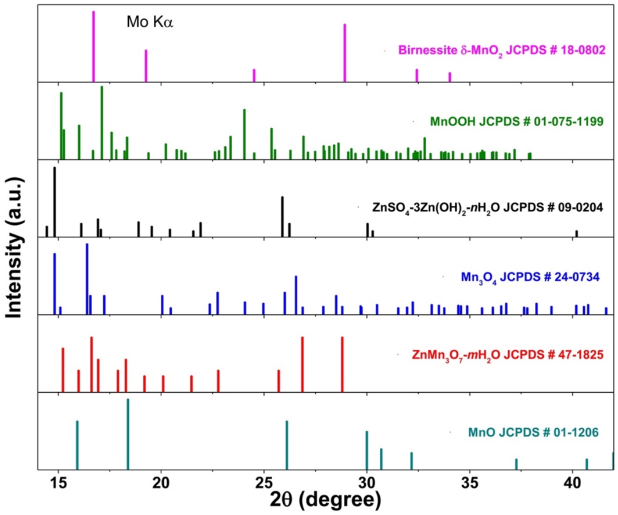

Figure 2.9. Standard XRD patterns of compounds that are identified and labelled in the XRD patterns of the initially deposited MnO_2 and cycled cathodes.

Compared with the originally deposited MnO_2, the diffraction patterns of MnO_2 cathodes discharged to 1.3 V at C/3 (**B** in Figure 2.7c and Figure 2.8a) and 3C (**D** in Figure 2.7c and Figure 2.8b) shift ~0.5° (2θ) toward lower angles. This clearly indicates a lattice expansion, likely caused by cation insertion, such as H^+/Zn^{2+} intercalation (e.g., Zn_xMnO_2).[46,96] Meanwhile, some characteristic reflections of MnOOH (JCPDS # 01-075-1199, standard XRD pattern in Figure 2.9) appear, presumably formed during the H^+ insertion accompanied by a structural relaxation (e.g., vacancy redistribution and/or rearrangement of Mn−O bonds).[48,98,99] The same reflection shift and the appearance of MnOOH at both points **B** and **D** suggest similar H^+/Zn^{2+} intercalation processes in the first discharge plateau (1.40 V) at high (3C) and low (C/3) rates.

After fully discharging to 1.0 V at C/3 (**C** in Figure 2.7c and Figure 2.8a), the XRD of point **C** clearly shows the formation of massive basic zinc sulfate $ZnSO_4{\cdot}3Zn(OH)_2{\cdot}nH_2O$ (mainly n = 4 with JCPDS # 09-0204, standard XRD pattern in Figure 2.9). Additionally, new reflections appearing at 26.1° (2θ), 36.2° (2θ), and 37.6° (2θ) are indexed to be Mn_3O_4 (JCPDS # 24-0734, standard XRD pattern in Figure 2.9), whereas the reflection at 26.1° (2θ) can be assigned to MnO (JCPDS # 01-1206, standard XRD pattern in Figure 2.9) as well. The XRD pattern of the fully charged state (**F** in Figure 2.7c and Figure 2.10a) is quite similar to that of the originally deposited MnO_2 electrode (**A**), implying that the parent MnO_2 phase is largely recovered after the initial recharge. The long-term cycling at low rates, however, will irreversibly accumulate Mn_3O_4 and $ZnSO_4{\cdot}3Zn(OH)_2{\cdot}nH_2O$ from the conversion reactions, evident by the apparent reflections of Mn_3O_4 and $ZnSO_4{\cdot}3Zn(OH)_2{\cdot}nH_2O$ appearing in the XRD of point **B** equivalent for the 10th cycle (Figure 2.10b) and point **C** equivalent for the 100th cycle (Figure 2.8c). After 100 cycles, the irreversible conversion products Mn_3O_4, MnO, and $ZnSO_4 \cdot 3Zn(OH)_2 \cdot nH_2O$ predominate on the electrodes, eventually disrupting the electrode structure and resulting in poor capacity retention, as will be discussed in more details below.

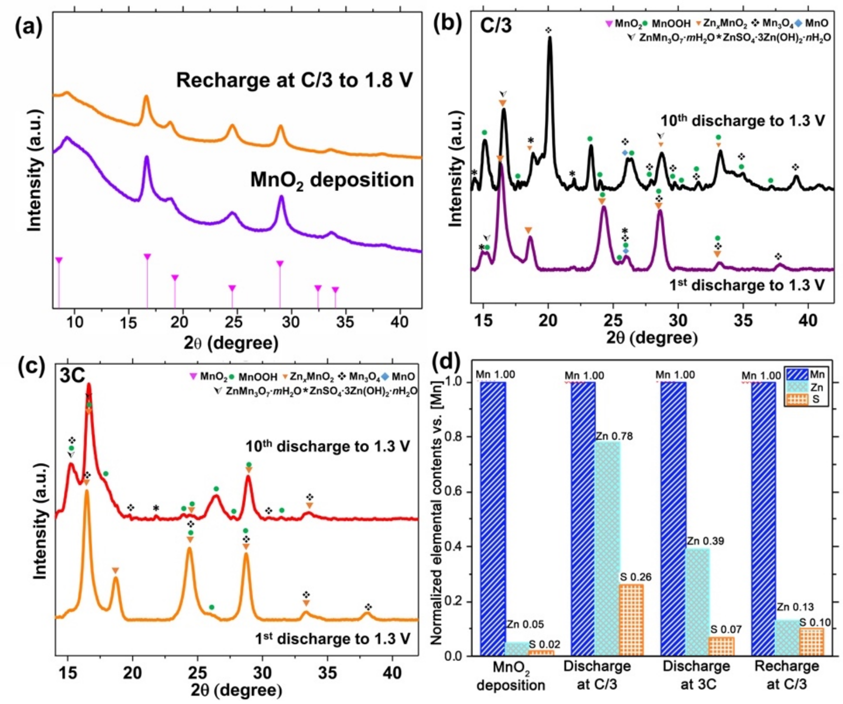

Figure 2.10. (a) XRD patterns of the initially deposited MnO_2 and fully recharged cathodes at C/3. XRD patterns of partially discharged cathodes after 1st and 10th cycles at (b) C/3 and (c) 3C. (d) The corresponding XRF analysis results of electrodes at different stages.

The XRD of the cathode discharged to 1.0 V at a high rate of 3C is shown in Figure 2.8b. The apparently lower peak intensities of $ZnSO_4 \cdot 3Zn(OH)_2 \cdot nH_2O$, Mn_3O_4, and MnO reflections for the fully discharged cathode (point **E**) suggest a significant suppression of the conversion reactions occurring at 1.26 V, well consistent with the largely decreased capacity of the second discharge plateau at 3C. Furthermore, after 10 cycles, $ZnSO_4 \cdot 3Zn(OH)_2 \cdot nH_2O$, Mn_3O_4, and MnO scarcely accumulate in the partially discharged cathode (Figure 2.10c). Only weak reflections of the Zn^{2+} conversion product $ZnMn_3O_7 \cdot mH_2O$ at 15.4° (2θ, Figure 2.8b) were observed in the initial discharge processes; however, these reflections were largely intensified during cycling. Figure 2.8d compares the XRD patterns of fully discharged electrodes at 3C after the 1st and 100th cycles. The original H^+/Zn^{2+}-inserted MnO_2 phases nearly disappear after 100 cycles. Instead, conversion products $ZnMn_3O_7{\cdot}mH_2O$, the tunneled Zn-woodruffite [T(3, 4)] (JCPDS # 47-1825, standard XRD pattern in Figure 2.9), and Mn_3O_4 dominate.

In short, abundant reflections were observed in the XRD patterns (Figure 2.8 and Figure 2.10). They were carefully analyzed and indexed to all possible compounds, which conveys more information about the discharged products and the reaction mechanisms as compared with previously reported ZIBs.[43,44] The XRD patterns with high resolution and low noise were made possible because a massive solid angle of data could be collected in a single exposure by the XRD device that has a large area curved image plate detector. This device is beneficial for measuring weakly diffracting disordered materials. Even so, the low crystallinity for many possible reaction products and their significant reflection overlap are still inevitable. Meanwhile, some discharge products are polymorphic and mutually transformable through various intermediate phases, depending on the local pH value, humidity, temperature, etc., which is really hard to control in the ex situ XRD tests.[49,50] Therefore, it is very challenging to exactly distinguish and confirm the phases in the electrode via XRD only, but XRD results are insightful for unraveling the trend in phase transitions from MnO_2 to MnOOH and Zn_xMnO_2 and finally to Zn^{2+}/H^+ conversion products to clarify the origin of capacity fade.

XRF analysis results of the cathodes at different stages of the first discharge/charge are shown in Figure 2.10d. The signals of Zn and S are normalized to the Mn signal. The initially deposited cathode is mainly composed of Mn as expected (O is not resolved here), with slight $ZnSO_4$ contamination from the electrolyte. The Zn and S contents, attributable to Zn_xMnO_2,

$ZnSO_4 \cdot 3Zn(OH)_2 \cdot nH_2O$ and $ZnMn_3O_7 \cdot mH_2O$, increase significantly for the fully discharged cathodes and nearly revert to the original values after recharging, indicating the near-reversible electrochemical processes in the first discharge/charge. The cathode discharged at C/3 shows double the Zn content and almost quadruple the S content compared to those discharged at 3C, which are consistent with their distinct discharged capacities (~400 vs ~290 mAh g^{-1}). More specifically, based on the Zn content of the discharged cathode at 3C, we can confirm the existence of Zn^{2+}-incorporated products, since at least 11% Zn (of the overall 39% Zn) in the cathode comes from Zn_xMnO_2 or $ZnMn_3O_7 \cdot mH_2O$, whereas the rest (28% Zn based on 7% S) is from $ZnSO_4 \cdot 3Zn(OH)_2 \cdot nH_2O$.

sXAS. To directly detect the chemical states of Mn, Mn *L*-edge sXAS was performed on electrodes at the representative electrochemical stages (Figure 2.11). Compared with the hard X-ray XAS of Mn *K*-edge that has been extensively applied to study the structure and valence of Mn in rechargeable Zn/MnO_2 cells,[46,100] soft X-ray-based sXAS is a more direct and sensitive probe to determine the valence 3d states of transition metals (TMs) through the dipole-allowed 2p−3d transitions.[101] For TM oxide-based battery materials, TM *L*-edge sXAS has been demonstrated as a sensitive and quantitative technique for fingerprinting the formal valence of the TM redox center.[102] Because TM *L*-edge sXAS probes the localized 3d states directly, the Mn *L*-edge sXAS spectral line-shape is insensitive to specific structural differences if a local octahedral structure is maintained.[103] The spectroscopic features could be well interpreted by comparing with reference spectra of different Mn states,[104] as indicated in Figure 2.11 by the vertical dashed lines.

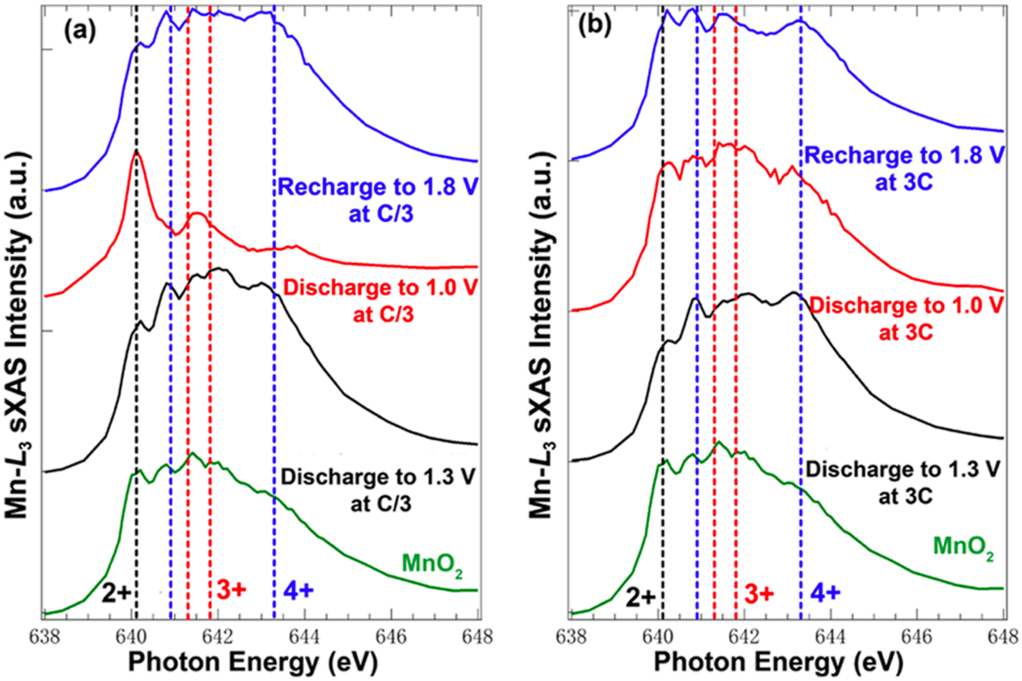

Figure 2.11. Mn L-edge sXAS of MnO_2 electrodes during the electrochemical process. Spectra are collected from the initially deposited MnO_2, the partially and fully discharged, and the fully recharged cathodes at current densities of (a) C/3 and (b) 3C.

Figure 2.11 focuses on Mn L_3-edge features that are much sharper compared with L_2 line-shape due to the intrinsic Coster−Kronig broadening. The spectra show that the as deposited MnO_2 electrode (**A** in Figure 2.7a) contains Mn^{4+} (641 and 643.5 eV), Mn^{3+} (641.5 and 642 eV), and Mn^{2+} (640 eV), supporting the existence of birnessite δ-MnO_2 composed of [$Mn^{4+/3+}O_6$] and [$Mn^{3+/2+}O_6$] octahedra, as well as interlayer $Mn^{3+/2+}$ ions. More interestingly, the MnO_2 electrodes, partially discharged to 1.3 V, display a slightly increased Mn^{4+} signal. This could occur especially on the surface, as δ-MnO_2 is reduced from Mn^{4+} to Mn^{3+} upon the electrochemical co-intercalation of Zn^{2+} and H^+, and subsequently, Mn^{3+} disproportionates into solid Mn^{4+} and soluble Mn^{2+}, resulting in Mn^{4+}-rich surface.[45] After discharging to 1.3 V, the $Mn^{4+/3+/2+}$ mixtures are well retained at both low (C/3, **B** in Figure 2.7c) and high (3C, **D** in Figure 2.7c) rates. This is consistent with the XRD results that show the current density (C-rate) exerting a minor effect on the H^+/Zn^{2+}

intercalation reactions at 1.40 V and thus similar H^+/Zn^{2+}-inserted δ-MnO_2 phases appearing at C/3 and 3C. However, a striking sXAS contrast between different rates is clearly seen when the electrodes are fully discharged to 1.0 V. Mn^{2+} peak, dominating the sXAS line-shape of the electrode at C/3 (**C** in Figure 2.7c), whereas Mn^{3+} and Mn^{2+} peak intensities only moderately increase with the 3C samples (**E** in Figure 2.7c).

This result clearly reveals an almost complete reduction of $Mn^{4+/3+}$ into Mn^{2+} after full discharge at C/3, accounting for the comparable discharge capacity of 190 mAh g^{-1} at 1.26 V reactions to that of 1.40 V reactions (210 mAh g^{-1}). For electrodes cycled at high rates (e.g., 3C), the kinetic-limited conversion reactions at 1.26 V are largely suppressed, resulting in a slight evolution of the Mn valences and thus smaller contribution to the overall discharge capacity. The intensity of Mn^{4+} peaks recovers and becomes stronger when fully recharged, signifying reversible Mn valence transitions between Mn^{4+} and $Mn^{3+/2+}$. The stronger Mn^{4+} peaks in the recharged cathode might correspond to the activation of MnO_2 deposits in the first few cycles. The finite amount of intensity variation here is likely a surface effect from the surface/bulk charge redistribution in the ex situ samples and the limited sXAS probe depth of about 10 nm. In short, the sXAS results not only present the overall Mn valence evolution upon electrochemical cycles but also reveal directly the sharp contrast on the 1.26 V discharge plateau in electrodes cycled at different rates.

SEM. Figure 2.12 show the surface morphology of the cathode at various cycling stages. The morphology of the originally deposited MnO_2 on carbon black surface shows hydrangea-shaped clusters that are several micrometers in diameter with petal-like nanosheets that are tens of nanometers in thickness (Figure 2.12a). After being discharged to 1.3 V at C/3 or 3C (Figure 2.12b,e), the electrodes primarily retain the original morphology of petal-like nanosheets. For the fully discharged cathode (1.0 V at C/3), however, large flake shaped crystals of ∼10−20 μm in size, as shown in Figure 2.12c, are formed and were found to be $ZnSO_4 \cdot 3Zn(OH)_2 \cdot nH_2O$ by means of EDS (Figure 2.13). These flakes, covering and growing across the MnO_2 clusters, would block the ion diffusion, disrupt the cathode structure, and thus result in a serious capacity loss in prolonged cycling. In contrast, for the cathode discharged at 3C, as shown in Figure 2.12f, the intergrowth between MnO_2 nanosheets and $ZnSO_4 \cdot 3Zn\text{-}(OH)_2 \cdot nH_2O$ flakes provides a stable and percolating microstructure, which is beneficial for the electrochemical reactions. Moreover, the sizes of $ZnSO_4 \cdot 3Zn(OH)_2 \cdot nH_2O$ flakes in 3C discharged electrode are less than 2 μm and are present in smaller amounts than those discharged at low rates. For the charged cathode shown in Figure 2.11d, the electrode reverts to the morphology of the original MnO_2 electrode, and only a few $ZnSO_4 \cdot 3Zn(OH)_2 \cdot nH_2O$ flakes are observed, which indicates the reversible precipitation/dissolution of $ZnSO_4 \cdot 3Zn(OH)_2 \cdot nH_2O$ during the cycling, accompanied by the local pH changes in the cathode/electrolyte interface as reported.[43,78] The petal-shaped MnO_2 nanosheets are retained during the whole electrochemical reaction processes, implying a stable and reversible microstructure for the concurrent intercalation and conversion reactions in the first few cycles. This also agrees with the reversible behavior inferred by the XRD results.

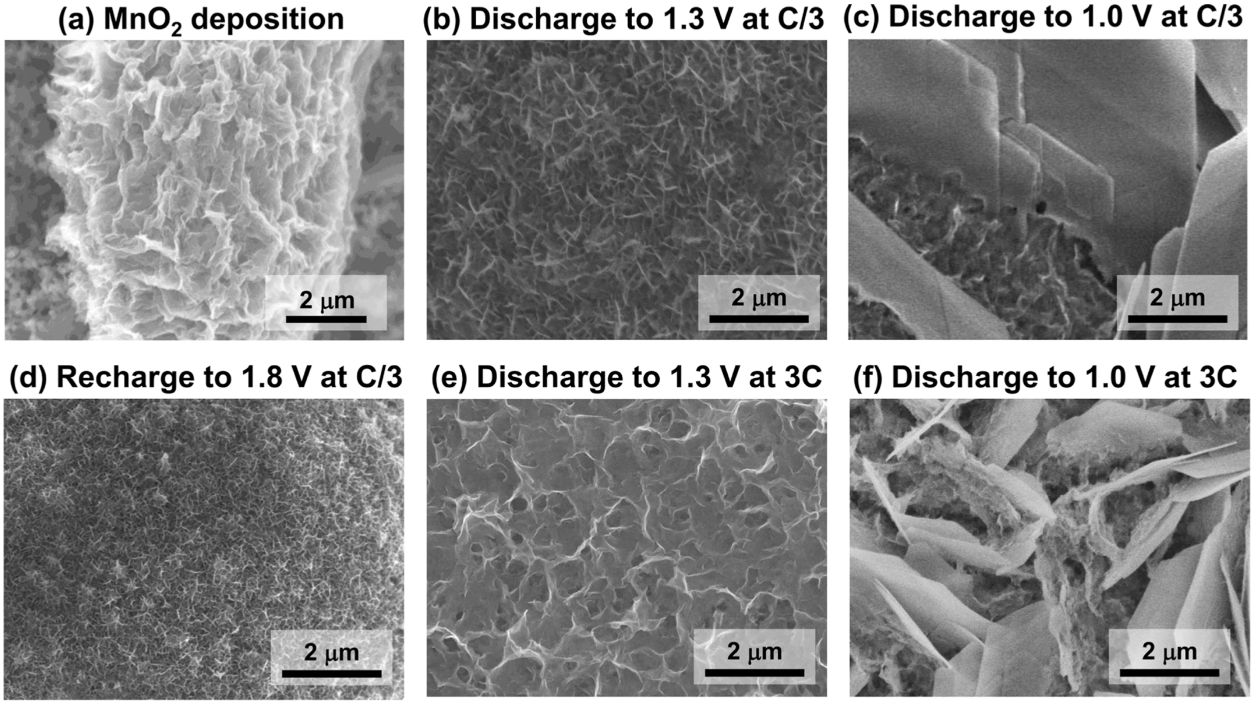

Figure 2.12. SEM images of MnO$_2$ cathodes. The cathodes recovered from the test cells after (a) MnO$_2$ deposition, discharged to (b) 1.3 V and (c) 1.0 V at C/3, (d) fully charged at C/3 and discharged to (e) 1.3 V and (f) 1.0 V at 3C.

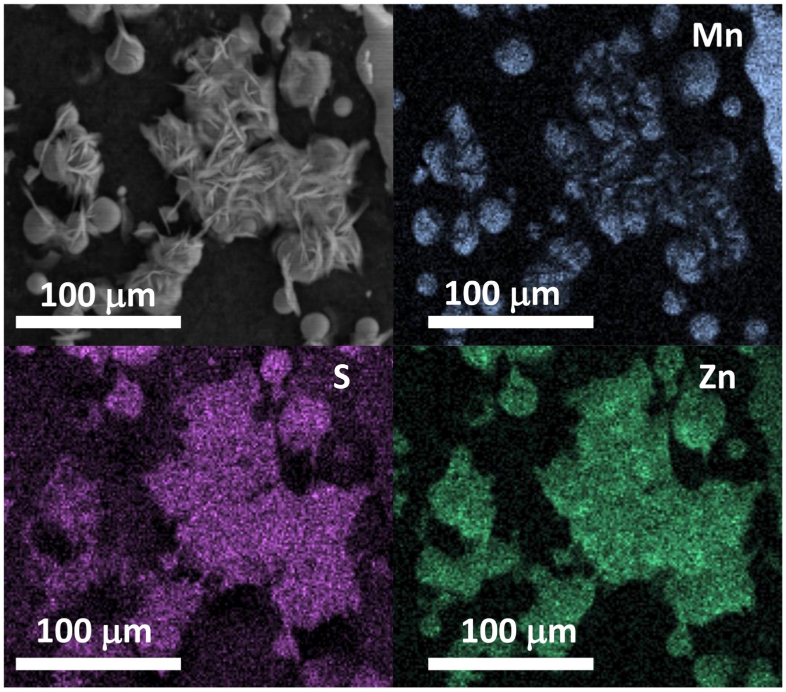

Figure 2.13. SEM image and corresponding EDS mappings of MnO$_2$ cathodes after fully discharged to 1.0 V at C/3.

In addition, the high reversibility of the Zn anode also contributes to the good cycling performance. SEM images of Zn anodes before and after 20 cycles are shown in Figure 2.14. The laminated Zn was well deposited with no sign of Mn contamination and no significant surface oxidation (EDS).

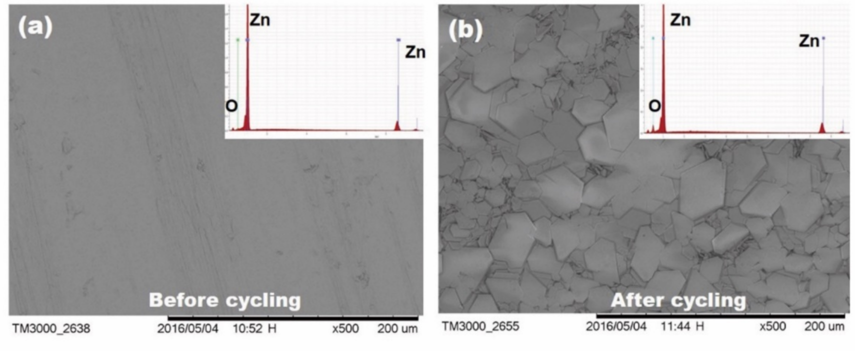

Figure 2.14. SEM images of Zn anode (a) before and (b) after 20 cycles.

2.3.3 *Summary of the Reaction Mechanisms and DFT Simulation*

Based on the above experimental analyses of electrochemical behavior, XRD, XRF, sXAS, and SEM, we can summarize the redox reactions and structural transformations occurring in the in situ Zn/MnO_2 cell, as shown in Figure 2.15.

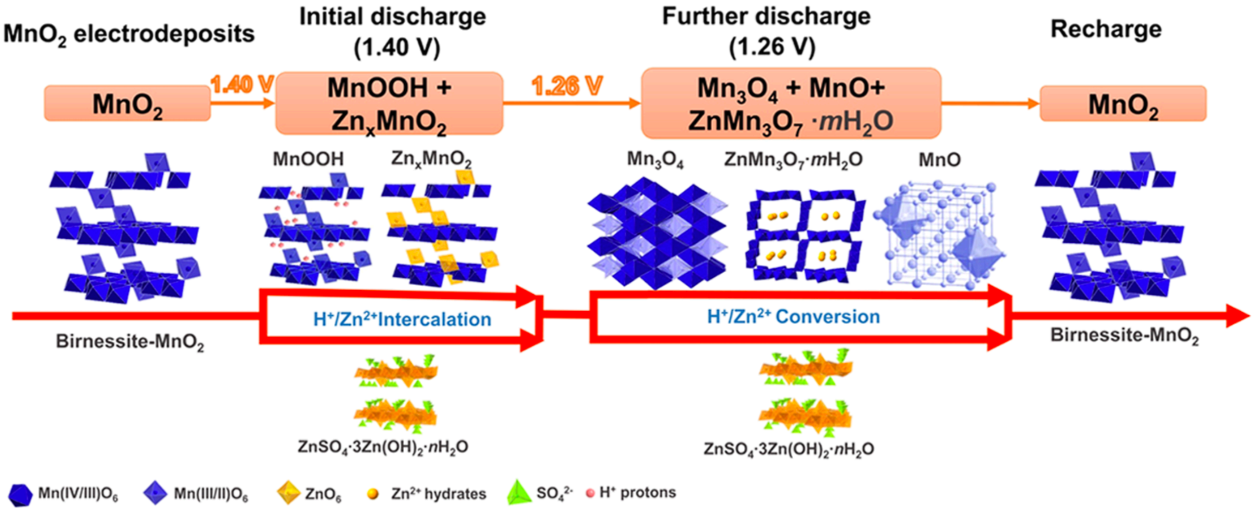

Figure 2.15. Schematic illustration of the redox reactions and crystal structures of related compounds in the Zn|0.2 M $MnSO_4$ (aq), 1 M $ZnSO_4$ (aq)|carbon black cells.

To further confirm our proposed reaction pathway, we used DFT simulations to calculate the voltages of the two redox reactions occurring at 1.40 and 1.26 V. Our calculations considered various H^+/Zn^{2+} intercalation and conversion reactions with MnO_2. The voltage of a redox reaction can be obtained from the difference in the total Gibbs free energy between the products and reactants, and the Gibbs free energies and structures of all compounds were computed based on fully relaxed structures (Table 2.1).

Table 2.1. The Gibbs free energy of all possible compounds.

System	Energy/formula (eV)
MnO_2	-21.205
$Zn(MnO_2)_8$	-172.75
MnOOH	-26.167
Mn_3O_4	-53.315
MnO	-15.538
$ZnMn_3O_7$	-69.379
$Zn(OH)_2$	-23.827
Zn	-1.106
H_2O	-14.889

Based on the DFT results, the major redox reactions can be formulated as below

1). H^+/Zn^{2+} intercalation reactions at ~ 1.40 V

$$84MnO_2+33Zn+10ZnSO_4+100H_2O$$

$$\xrightarrow{H^+/Zn^{2+}\text{intercalation}} 60MnOOH+24Zn_{0.125}MnO_2+10[ZnSO_4\cdot 3Zn(OH)_2\cdot 4H_2O], \tag{2.1}$$

2). H^+/Zn^{2+} conversion reactions at ~ 1.26 V

$$8Zn_{0.125}MnO_2+16MnOOH+4Zn+ZnSO_4+3H_2O$$

$$\xrightarrow{H^+/Zn^{2+}\text{conversion}} 5Mn_3O_4+3MnO+2[ZnMn_3O_7\cdot 2H_2O]+ZnSO_4\cdot 3Zn(OH)_2\cdot 4H_2O. \qquad (2.2)$$

The calculated voltages for Eqs. 2.1 and 2.2 are 1.39 and 1.26 V, respectively, agreeing very well with the experimental results. Here, we took $Zn_{0.125}MnO_2$ as the Zn insertion compound for simplicity[105] and MnOOH as the H insertion compound. We also calculated the voltages of other possible redox reactions, such as Zn^{2+} intercalation as the exclusive reaction at the initial discharge stage; however, the calculated voltages are significantly different from the experimental values that oblige us to rule out these scenarios, as shown in Table 2.2. Due to the complexity of Zn/MnO_2 system, there might be some minor side reactions, which will neither significantly contribute to the capacity nor influence the electrochemical behavior. It is worth noting that although Eq. 2.1 is primarily denoted as the intercalation reaction due to the H^+/Zn^{2+} insertion into MnO_2 at 1.40 V, it is also accompanied by a conversion reaction that forms $ZnSO_4\cdot 3Zn(OH)_2\cdot nH_2O$ as a discharge byproduct.

Table 2.2. The Gibbs free energies and resulting voltages of representative reaction equations.

Reaction Equations	**ΔG(eV)**	**Voltage (V)**
(1) $6MnO_2 + 3Zn + ZnSO_4 + 10H_2O \rightarrow 6MnOOH + ZnSO_4\bullet 3Zn(OH)_2\bullet 4H_2O$	-8.604	1.43
(2) $8MnO_2 + Zn \rightarrow 8Zn_{0.125}MnO_2$*	-2.009	1.01
(3) $84MnO_2 + 33Zn + 10ZnSO_4 + 100H_2O \rightarrow 60MnOOH + 24Zn_{0.125}MnO_2 + 10[ZnSO_4\bullet 3Zn(OH)_2\bullet 4H_2O]$	-92.067	1.39
(4) $18MnOOH + 3Zn + ZnSO_4 \rightarrow 6Mn_3O_4 + ZnSO_4\bullet 3Zn(OH)_2\bullet 4H_2O + 2H_2O$	-6.381	1.06
(5) $6MnOOH + 3Zn + ZnSO_4 + 4H_2O \rightarrow 6MnO + ZnSO_4\bullet 3Zn(OH)_2\bullet 4H_2O$	-4.390	0.73

(6)	$72Zn_{0.125}MnO_2 + 39Zn + 16ZnSO_4 + 112H_2O \rightarrow 24Mn_3O_4 + 16[ZnSO_4{\bullet}3Zn(OH)_2{\bullet}4H_2O]$	-110.655	1.42
(7)	$24Zn_{0.125}MnO_2 + 21Zn + 8ZnSO_4 + 56H_2O \rightarrow 24MnO + 8[ZnSO_4{\bullet}3Zn(OH)_2{\bullet}4H_2O]$	-45.948	1.09
(8)	$8Zn_{0.125}MnO_2 + Zn + 4H_2O \rightarrow 2MnO + 2[ZnMn_3O_7{\bullet}2H_2O]$	-4.026	2.013
(9)	$8Zn_{0.125}MnO_2 + 16MnOOH + 4Zn + ZnSO_4 + 3H_2O \rightarrow 5Mn_3O_4 + 3MnO + 2[ZnMn_3O_7{\bullet}2H_2O] + ZnSO_4{\bullet}3Zn(OH)_2{\bullet}4H_2O$	-10.075	1.26
(10)	$48Zn_{0.125}MnO_2 + 74MnOOH + 41Zn + 10H_2O \rightarrow 38Mn_3O_4 + 8MnO + 47Zn(OH)_2$	-103.02	1.26
*	Zn_xMnO_2 takes x=0.125 as an example		

2.3.4 *Kinetic Behavior*

To discern the different kinetic behaviors of the two separate redox reactions at 1.40 and 1.26V, the standard reaction constants $k^\circ_{1.40V}$ and $k^\circ_{1.26V}$ were derived by CV, along with the EIS results of a Zn/MnO_2 cell discharged to two different statuses (1.40 and 1.26 V).

Figure 2.16a shows a series of cyclic voltammograms obtained at different scan rates (0.1−1 mV s^{-1}). The CV curves display two pairs of redox peaks. The two pairs of cathodic/anodic peaks in the CV curve at 0.1 mV s^{-1} locate at ~1.39/1.58 and ~1.26/1.56 V, respectively. It is clear that the former redox pair (~1.39/1.58 V) is more reversible than the latter one (~1.26/1.56 V), due to its smaller voltage polarization (190 vs 300 mV). The peak current is expressed as[106]

$$i_{pc} = 0.227nFACk^0 \exp\left[-\frac{(\alpha n_a F)}{(RT)}\left(E_{pc} - E^{O'}\right)\right], \tag{2.3}$$

where i_{pc} is the peak cathodic current; n is the number of electrons involved in the overall electrode processes; A is the electrode area; C is the maximum concentration change of H^+/Zn^{2+} in the cathode materials; α is the charge-transfer coefficient; n_a is the number of electrons involved in the redox steps; E_{pc} is the peak cathodic potential; and $E^{\circ\prime}$ is the formal potential. The average formal potential values of 1.48 and 1.40 V are used to plot the ln i_{pc} versus ($E_{pc} - E^{\circ\prime}$) relations for the two reactions at 1.40 and 1.26 V, respectively.

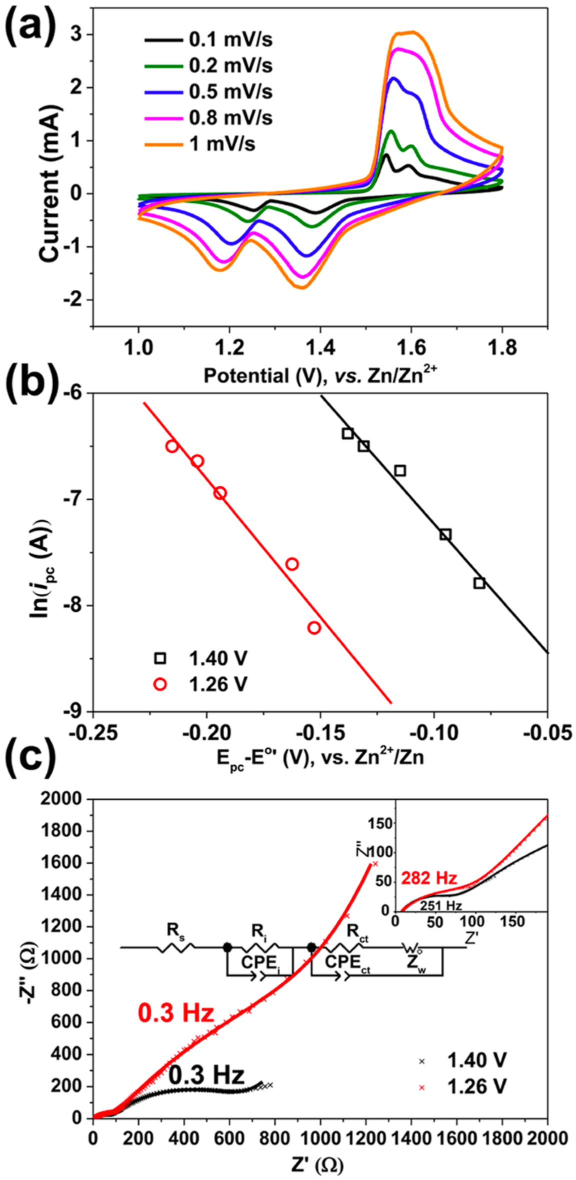

Figure 2.16. Kinetic behavior of Zn/MnO$_2$ cells. (a) Cyclic voltammograms of in situ deposited MnO$_2$ cathode at various scan rates (0.1, 0.2, 0.5, 0.8, 1.0 mV s^{-1}). (b) Plots of ln i_{pc} vs ($E_{pc} - E^{\circ\prime}$) for the 1.40 and 1.26 V reductions. (c) EIS analysis of MnO$_2$ cathode discharged to 1.40 and 1.26 V.

Figure 2.16b presents the plots of ln i_{pc} versus ($E_{pc} - E^{\circ\prime}$) obtained from the cyclic voltammograms. From the intercepts of the straight lines, the standard reaction rate constants $k^{\circ}_{1.40V}$ and $k^{\circ}_{1.26V}$ are calculated as 1.26 Å~ 10^{-7} and 1.58 Å~ 10^{-8} cm s^{-1}, respectively. The standard reaction rate constant at 1.40 V ($k^{\circ}_{1.40V}$) is near 10 times larger than that at 1.26 V ($k^{\circ}_{1.26V}$) and is also comparable to that of $LiNi_{1/3}Co_{1/3}Mn_{1/3}O_2$ (NMC111) in LIBs for intercalation reaction (~2.5 Å~ 10^{-7} cm s^{-1}).[107]

The kinetic behavior was also studied by EIS. Figure 2.16c shows the EIS results of a Zn/MnO_2 cell discharged to two different statuses (1.40 and 1.26 V). The discharged cell displays two semicircles in high- and middle frequency regions, representing the interfacial and charge transfer resistances, respectively, and a diffusion tail in the low frequency region due to the ion diffusion processes in solids.[77,108] The EIS data can be fit using the equivalent circuit shown in the inset, and the fitted data are shown in Table 2.3. After being discharged to 1.3 V at C/3, fitting the EIS data gives an internal resistance ($R_{s,1.40V}$, 7.3 Ω), an interfacial resistance ($R_{i,1.40V}$, 66.3 Ω), and a charge-transfer resistance ($R_{ct,1.40V}$, 646.5 Ω). In comparison, the cell fully discharged to 1.0 V at C/3 shows a much higher $R_{ct,1.26V}$ (2019.2 Ω) but similar $R_{s,1.26V}$ (6.6 Ω) and $R_{i,1.26V}$ (93.2 Ω). The largely increased charge-transfer resistance is primarily due to the irreversible conversion products, which disrupt the electrode structure and thus largely hinder the ion and electron transports, consistent with the above XRD and SEM analyses.

Table 2.3. Impedance fitting parameters of MnO_2 cathode discharged to 1.40 V and 1.26 V

	1.40 V		1.26 V	
	Value	Error (%)	Value	Error (%)
R_s	7.3	2.70	6.6	1.01
R_i	66.3	5.19	93.2	3.12

R_{ct}	646.5	3.35	2019.2	6.94
Z_w	102.5	3.51	1386.0	10.66

In general, a kinetic-limited reaction has a small $k°$, a small exchange current density i_0, and thus a high R_{ct}. For a small i_0, a large current density will require a large activation energy E_a, leading to a large overpotential to allow the reaction to proceed. In this case, only a small fraction of the initial reactants has enough energy to overcome the energy barrier and form the final products, leading to a small measurable capacity.

As a result, reaction energetics are plotted in Figure 2.17 to illustrate the different kinetic behaviors of the two redox reactions. For the H^+/Zn^{2+} intercalation reactions at ~1.40 V, a smaller energy barrier will allow for a higher reaction rate, and an increase in current will not significantly increase the energy barrier due to its large rate constant $k°_{1.40V}$ and low charge-transfer resistance $R_{ct,1.40V}$. On further discharge at ~1.26 V, however, the rate-limiting process possesses a high activation barrier due to its small $k°_{1.26V}$ and high $R_{ct,1.26V}$, especially at high rates. The concurrence of conversion reactions with both H^+ and Zn^{2+} at 1.26 V is responsible for the undesirable rate performance, since these conversion reactions cause a large volume change, sluggish phase transformation, the formation of electrochemically inactive $ZnSO_4 \cdot 3Zn(OH)_2 \cdot nH_2O$, etc.[96,99,105] Therefore, at large current densities, the slow conversion reactions will be largely suppressed, causing a smaller capacity reduction and thereby significantly improving the overall capacity retention. Even though the reaction mechanisms demonstrated here are for our in situ formed Zn/MnO_2 cells, we believe that the concomitant intercalation and conversion reactions of H^+/Zn^{2+} could be ubiquitous to other aqueous Zn/MnO_2, considering the similar electrochemical behavior (discharge profiles, cycling properties) and similar cell structure (same electrodes and electrolytes).[43,47,109]

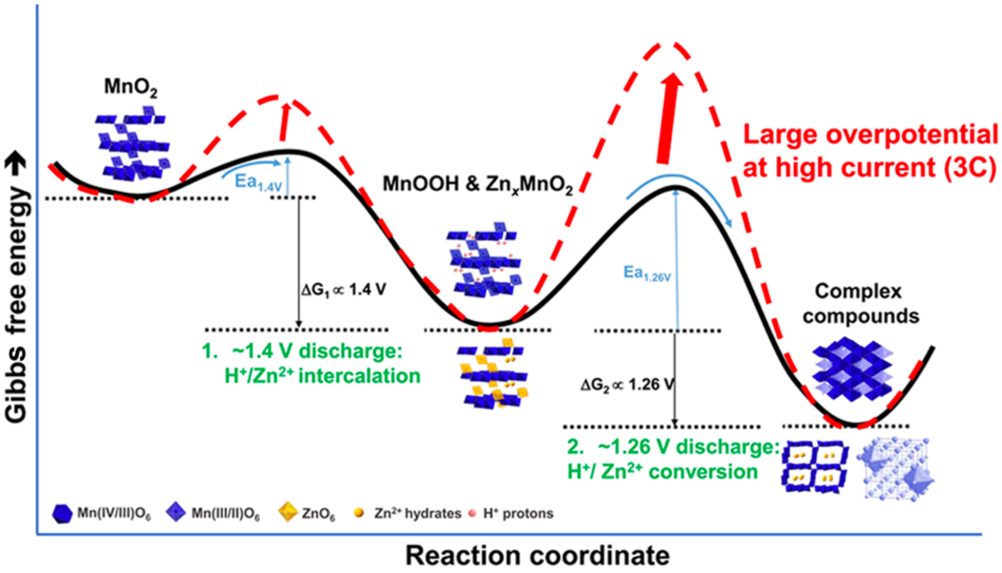

Figure 2.17. Gibbs free energy vs. reaction coordinate showing the thermodynamic and kinetic properties of the redox reactions in Zn/MnO_2 cells with different rates.

2.3.5 *Optimizing the Power Capability and Cycling Stability*

According to our understanding of the reaction mechanisms and kinetic behavior in Zn/MnO_2 cells, to improve the cycle stability, it is desirable to mitigate/eliminate the rate-limiting, irreversible, and electrode-disrupting conversion reactions occurring at ∼1.26 V. As the first example, the in situ Zn/MnO_2 cells were designed to be cycled at higher rates, e.g., 9C and 30C, to restrain the irreversible H^+/Zn^{2+} conversion reactions at ∼1.26 V, as shown in Figure 2.18a,b. As expected, a higher current density largely restrains the capacity of the second discharge plateau as compared to that of the discharge/charge profiles at C/3 (Figure 2.18a). Consequently, high-rate cycling between 1.0 and 1.8 V largely improves the cycle stability (Figure 2.18b). For instance, the 9C and 30C cells deliver discharge capacities of 175 and 75 mAh g^{-1} after 1000 cycles, respectively. More importantly, there is no significant capacity fading for the two cells after several initial cycles (to stabilize the cathode).

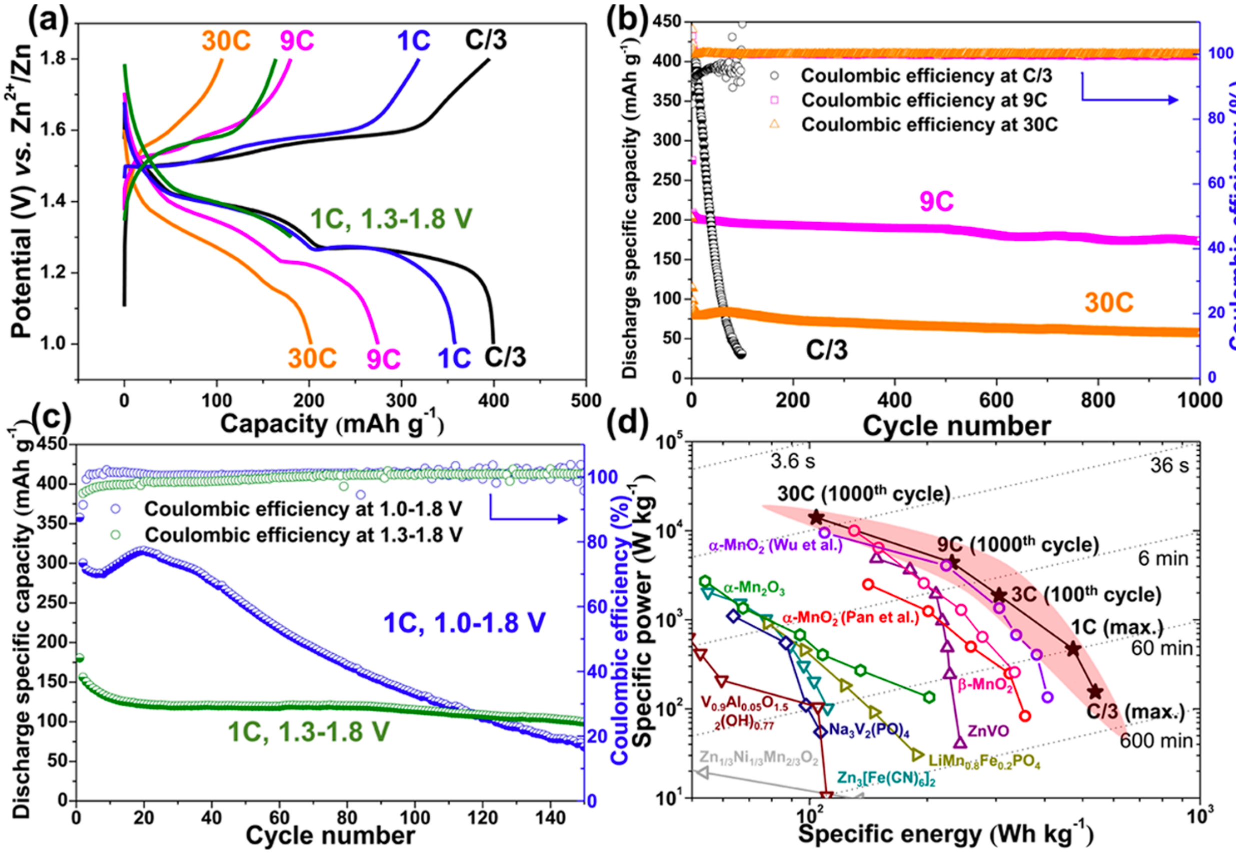

Figure 2.18. Improved electrochemical performance of the in situ Zn/MnO$_2$ cells. (a) Discharge/charge profiles and (b, c) cycling performance of the cells at different current densities (C/3, 9C, and 30C) and different voltage ranges (1.0−1.8 and 1.3−1.8 V). (d) Ragone plot (power vs energy densities) of the in situ Zn/MnO$_2$ cells as compared with that of the previously reported ZIBs with ex situ MnO$_2$ and other cathode materials.

In the second example, by increasing the low cutoff voltage from 1.0 to 1.3 V, the irreversible conversion reactions at 1.26 V can be eliminated (Figure 2.18a). The cell has an initial capacity of 175 mAh g^{-1} at 1C, about half of that of the cell discharged to 1.0 V. After a rapid capacity fade in the initial 10 cycles, the cell discharged to 1.3 V shows negligible fading after 150 subsequent cycles (Figure 2.18c). To acquire the typical cycling performance in Figure 2.18a−c, at least six cells were simultaneously examined under each discharge condition (C/3−30C, 1.0−1.8 V or 1C, 1.3−1.8 V). The deviation of delivered capacities in the six cells is within 50 mAh g^{-1}. The reason for the large initial capacity drop in the cells at different current densities, as shown in Figure 2.7 and Figure 2.18, is unclear and will be investigated in the future. Of note, we caution that increasing the lower limit of the discharge voltage would decrease the overall energy density. Nonetheless, the irreversible reactions at 1.26 V are clearly revealed and corroborated here. For large-scale energy storage applications, the cycling stability is more critical than the energy density, and thus for practical use, increasing the cutoff voltage to 1.3 V is still a reliable way to improve the cycling stability of Zn/MnO_2 batteries. Studies to modify the irreversible reactions at 1.26 V are planned in an effort to increase the overall energy density of the Zn/MnO_2 cell.

Figure 2.18d shows the Ragone plot (power density vs energy density for cathode only similar to those reported previously) of in situ Zn/MnO_2 cells as compared to that of the previously reported Zn/MnO2 cells and ZIBs with other cathode materials (α-MnO_2,[43,77] β-MnO_2,[42] $Zn_{0.25}V_2O_5 \cdot nH_2O$,[110] α-$Mn_2O_3$,[111] $V_{0.9}Al_{0.05}O_{1.52}(OH)_{0.77}$,[112] $Na_3V_2(PO_4)_3$,[113] $LiMn_{0.8}Fe_{0.2}PO_4$,[114] $Zn_3[Fe(CN_6)]_2$,[115] $Zn_{1/3}Ni_{1/3}Mn_{2/3}O_2$[116]). Our cell cycled at 9C exhibits gravimetric energy and power density up to 231 Wh kg^{-1} and 4 kW kg^{-1}, respectively. These values, achieved after 1000 cycles, are much higher than those of conventional Zn/MnO2 and ZIBs with other cathode materials published recently. In particular, the cell cycled at 30C has a power density of 15 kW kg^{-1}, close to that of supercapacitors.[117] Overall, our in situ aqueous Zn/MnO_2 cells show very competitive electrochemical performance suitable for stationary grid storage, especially taking into account their low cost and superior safety. The electrochemical performance of the in situ Zn/MnO_2 cells could be further improved by optimizing the MnO_2 deposition (morphology, porosity, composition, loading mass, surface coating, etc.)[118] or by optimizing the electrolyte to improve the rate and reversibility of the conversion reactions.

2.4 CONCLUSION

In this work, in situ formed Zn/MnO_2 cells with Zn and carbon black electrodes in the $MnSO_4$−$ZnSO_4$ electrolyte are developed. Our coupled experimental and theoretical study clarifies the complex redox reactions in Zn/MnO_2 system, as such; there exists a concurrence of Zn^{2+} and H^+ intercalations and conversion reactions corresponding to the two discharge plateaus at ∼1.40 and ∼1.26 V, respectively. These two types of reactions show quite different kinetics and thus distinct rate dependent capacities and capacity retention. The capacity of H^+/Zn^{2+} intercalation reactions is well retained and rate insensitive, whereas that of the subsequent H^+/Zn^{2+} conversion reactions is highly dependent on the discharge/charge rate. The proposed reaction mechanisms in our in situ Zn/MnO_2 cell could be applied to ex situ Zn/MnO_2 systems or other ZIBs, opening an avenue to further improve their cycling and power performance.

Chapter 3. REACTION MECHANISMS OF LI/S BATTERIES WITH A THIOL-MODIFIED MESOPOROUS CARBON*

3.1 INTRODUCTION

3.1.1 *Advantages of Li/S Batteries*

Energy batteries with high energy density are of increasing importance due to the growing demand for long-range EVs.[8,120] Li/S batteries have attracted broad interest due to their high theoretical specific capacity (1672 mA h g^{-1}, an order of magnitude greater than that of the current commercial $LiCoO_2$ cathode material), high theoretical energy density of 2600 Wh kg^{-1}, low environmental impact, and low cost.[121]

3.1.2 *General Reaction Mechanisms and Relevant Challenges in Li/S Batteries*

Generally, in the Li/S, the voltage profile features of the electrodes reflect two discharge plateaus at 2.3 V and 2.1 V as shown in Figure 3.1.[122123] It is accepted that the upper plateau is related to a solid–liquid two phase conversion from elemental S_8 to long-chain $Li_2S_{(8,6)}$, while the lower is associated with a transition from liquid to solid-phase species as soluble chains are reduced to insoluble discharge products, $Li_2S_{(2,1)}$.[122,124]

---

*This chapter is reproduced from the article, Li, Y. et al. "A multi-functional interface derived from thiol modified mesoporous carbon in lithium–sulfur batteries" *J. Mater. Chem. A, 2019,* **7**, 13372.[119] Copyright (2019) Royal Society of Chemistry. This is an unofficial adaptation of an article that appeared in an RSC publication. RSC has not endorsed the content of this adaptation or the context of its use.

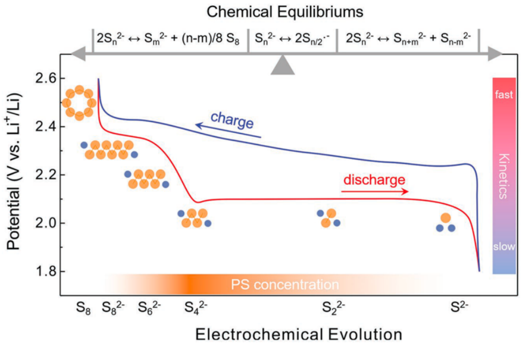

Figure 3.1. The compendium of lithium polysulfide (LiPS) composition and evolution in Li/S batteries.[122]

The dissolution of soluble lithium LiPS redox intermediates (*e.g.,* $Li_2S_{(8,6)}$) generated during the complex multi-step charge/discharge reactions results in rapid capacity fading upon extended cycling,[55] which is one of the failure mechanisms hindering the commercialization of Li/S batteries. Approaches that aim simply to lower LiPS solubility would introduce new performance deficits such as reduced reaction kinetics and poor active material utilization.[125,126] In order not to sacrifice the general performance for the sake of cyclability, the design of cathode host materials which can better retain solvated LiPSs has become an area of intense research.[127]

3.1.3 *Efforts on Physical and Chemical Trapping of LiPSs*

Initial work on LiPS-trapping were focused on designing nanostructured carbon materials such as mesoporous carbon particles, carbon nanotubes (CNTs), and graphene/graphene oxide sheets, as shown in Figure 3.2.[58,128–140] Carbon materials were preferentially investigated as a means to physically confine solvated LiPSs in the host matrix due to their high electrical conductivity, large specific surface area, and ability to modulate the pore volume available for sulfur infiltration. Although these materials greatly improve cell performance, it has been found that physical confinement alone is not sufficient to prevent large capacity losses, as LiPSs will still gradually diffuse out of the porous network due to the polarity difference between non-polar carbon and polar LiPSs.[141] The non-polar carbon also introduces a new challenge, namely poor electrolyte wetting for thick electrodes.[141,142]

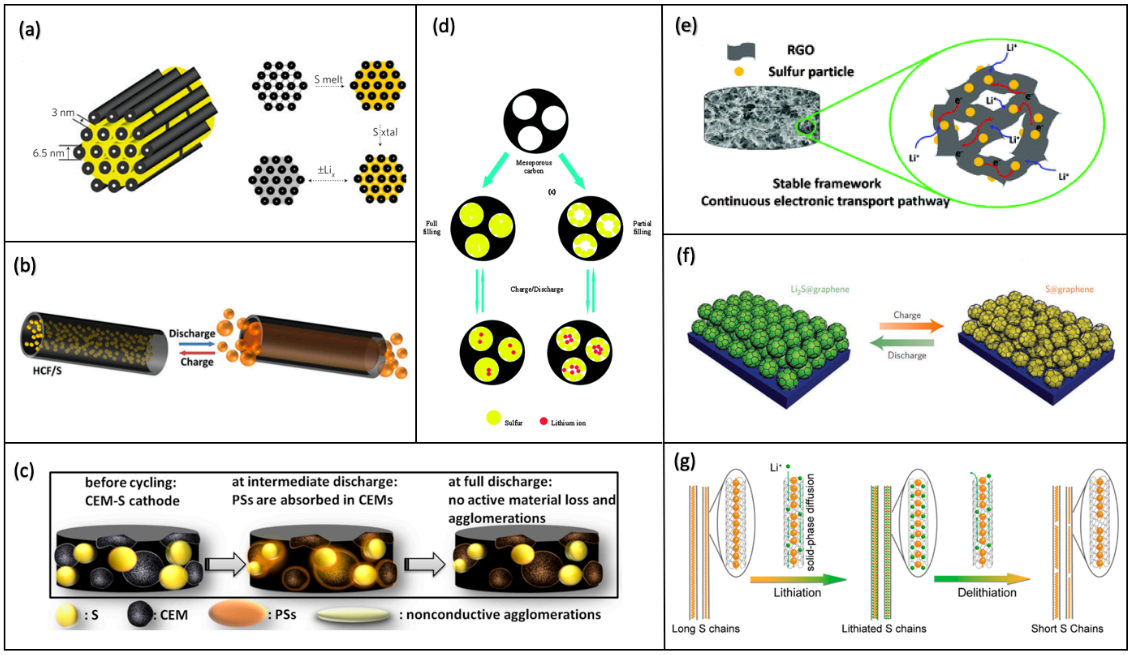

Figure 3.2. Schematic diagrams of the sulfur physically confined in (a) mesoporous carbon CMK-3,[58] (b) hollow carbon nanofibers (HCFs),[139] (c) carbonized eggshell membrane (CEM),[140] (d) mesoporous carbon,[129] (e) 3D graphene sponge,[130] (f) graphene nano-capsules,[131] (g) 1D carbon nanotubes (CNTs).[132]

Thus, research efforts have been made towards implementing chemical functionalities to further improve a host material's ability to trap LiPSs. Most approaches implement inherently polar materials such as heteroatom-doped carbon structures,[143–146] polymer coatings,[59,60,147] metal–organic frameworks,[144,148,149] and metal-chalcogenide blends,[150–152] as shown in Figure 3.3. Although these approaches have realized some success in improving cyclability, they often rely only on limited and single electrostatic interactions, suffer from reduced electrical conductivity, or involve heavy/expensive nanostructures, which sacrifice the potential advantages of Li–S chemistry.[128,153,154]

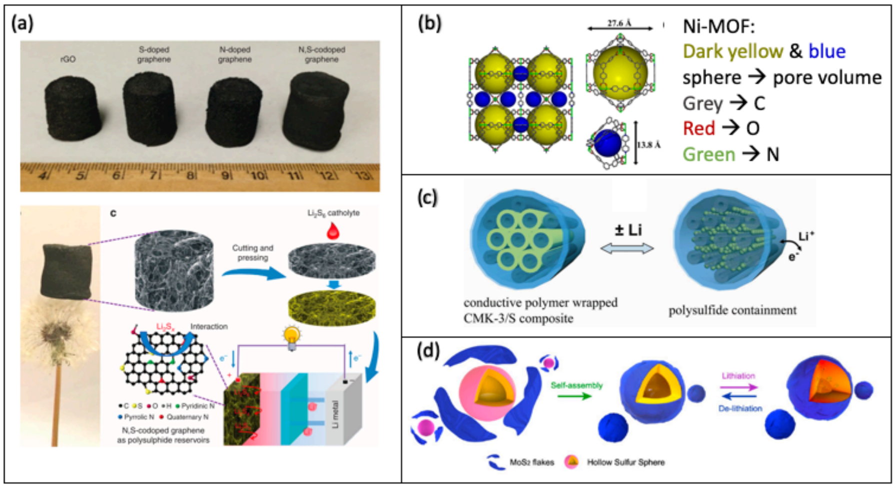

Figure 3.3. Schematics of (a) N,S-codoped graphene sponge,[146] (b) Ni-MOF,[149] (c) conductive polymer wrapped CMK-3/S composite,[147] (d) MoS_2-encapulated hollow sphere,[152] which can chemically interact with LiPSs.

3.1.4 *New Strategy for LiPS-Trapping*

With all the challenges in mind, a light-weight sulfur host material with good electrical conductivity and improved wettability to the electrolyte, that not only confines LiPSs physically but also contains a very high accessible fraction of LiPS chemisorption sites, is well suited to realize long-life and high-loading Li–S batteries. To achieve the goal, in this thesis, we suggest to chemically functionalize the nonpolar surface of nanostructured carbon materials with a thin layer of phenylthiol small molecules via a one-pot reaction where we in situ generate aryl-diazonium ions.[155] This approach has many benefits including simplicity, scalability, tunability, and general applicability to any surface with the sp^2 hybridized carbon functionality. Here we selected commercially available mesoporous carbon materials as the platform to study the features of phenylthiol surface modification. Graphene materials and CNTs were not considered due to their complexity such as the random orientation and discrepant defects of graphene sheets and the tedious synthetic and harsh reaction conditions to modify CNTs.[156–162] These obstacles make it difficult to stabilize and control the functionality of graphene materials and introduce large amounts of structural damage in CNTs.[159]

In the past few years, hydroxyl and epoxide functional groups have been reported to possess a single chemical interaction (O–Li) with LiPSs.[146,163,164] In this thesis, we for the first time designed phenylthiol modifiers at the molecular level on the surface of the carbon matrix to facilitate multiple interactions with LiPSs. Due to the widely studied interconversion between the thiol (S–H) and disulfide (S–S) bonding modes through intermediate thiolates (–S$^-$) and thiyl radicals (–S•),[165–168] thiol groups are chosen to potentially allow for covalent tethering of LiPSs to the surface of mesoporous carbon hosts. Furthermore, the thiol modifier could enhance the electrolyte wettability of electrodes by creating a more polar electrode surface, inducing electrostatic interactions with the solvated Li$^+$ ions of dissolved LiPSs, as well as lithium bis(trifluoromethanesulfonyl)imide (LiTFSI) salt in 1,3-dioxolane/1,2-dimethoxyethane (DOL/DME) based electrolytes. This effect has important implications for high sulfur-loading cathodes, which are required for commercially viable cells and is often overlooked when discussing cathode additives/strategies.[141,142] The thiol-functionalized carbon host has not been studied probably because the thiol functionality was predominantly consumed as reactive groups to prepare crosslinked organosulfur polymers in Li/S batteries.[169–171] These sulfur-rich polymers as new cathodes are chemically distinct from the conventional melt-infiltrated carbon–sulfur composites used in this thesis. The vulcanized co-polymers usually suffer from inherently low conductivity and require larger amounts of inert conductive additives, in addition to the inert mass added by the organic structures themselves, which detracts from the overall energy density.

3.1.5 *Investigation of The Reaction Mechanisms of LiPSs with The Thio-Functional Interface via Spectroscopic Characterizations*

In Li/S batteries, for most materials, it is quite challenging to identify the specific role of individual species in cell function owing to the complexity in characterizing amorphous structures and versatile ionic species.[61] In this thesis, we successfully utilize solid-state nuclear magnetic resonance (NMR) spectroscopy, X-ray photoelectron spectroscopy (XPS), and electrochemical impedance spectroscopy (EIS) to monitor the molecular motion and surface interactions of the thiol groups with active materials inside the cathodes upon cycling. We studied the effects of the functionality on the electrochemically produced LiPSs from the cycled cells, different from theoretical calculations or alternative investigation of the functionality with pre-made LiPS solutions of defined compositions.[146] Moreover, we conduct a systematic study of the influence of multi-functional thiol surfaces on high-sulfur-loading (4 mg cm^{-2}) cathodes by controlling the concentration of thiol groups on the surface. Though ultimately successful in improving cyclability, our analysis reveals some inherent limitations of this particular surface modification strategy, including a slight increase in cell overpotential and kinetic limitations during discharge. We thus present future steps that might be taken to mitigate these challenges.

3.2 EXPERIMENTAL SECTION

3.2.1 *Preparation of [SH]-Thiol MJ430 Carbon*

As-received MJ430 (Porous Carbon CNovel™; TOYO TANSO USA, INC.) was purified by acid wash with 2 M HCl in ethanol. Purified carbon powders were mixed with 5, 10, 15, 20, and 50 mol% 4-aminophenylthiol (Sigma Aldrich) and sonicated in anhydrous tetrahydrofuran for 20 min. This mixture was then placed in an ice bath before adding a stoichiometric equivalent of isoamylnitrite (Sigma Aldrich) and double stoichiometric equivalent of HCl to initiate in situ diazotization. Initiation of the reaction should produce N_2 gas, which bubbles out of the solution. Once the gas generation ceased, the reaction mixture was heated to 70 °C and stirred vigorously for 12 h. Reaction products were cleaned and filtered with subsequent washes of (2 : 1) ethanol : ammonium hydroxide, tetrahydrofuran, water, and finally acetone. Cleaned products were then vacuum dried under high-vacuum at 90 °C for 12 h.

3.2.2 *Material Characterization*

Thermogravimetric analysis (TGA) was performed under a nitrogen flow of 50 mL min$_{-1}$with a heating rate of 10 ºC min$_{-1}$ to 800 ºC by using a Mettler Toledo TGA/DSC 3+. The surface area of the samples was determined from the isotherms collected with a QUANTACHROME NOVA 2200e gas sorption system by using the BET method. The BJH method was used for the porosity and pore size analyses. Surface chemical characteristics of the samples were examined using XPS. The physicochemical structures were examined using a Renishaw inVia Raman microscope. Electrical conductivity was measured by the four-point method using an IV Source Meter (2450, Keithley). TheMJ430-S and SHMJ430-S films were fabricated by the slurry casting method on polyethylene naphthalate (PEN). The morphology and elemental distribution of the materials were characterized using SEM-EDS (Phillips XL-30 Sirion FE-SEM with EDAX EDS). Microstructures and compositions were analyzed by S/TEM (FEI Titan 80–300 kV, USA).

3.2.3 *Preparation of MJ430-S and [SH]-MJ430-S Composites*

To impregnate sulfur into MJ430 or [SH]-MJ430 carbon for preparing MJ430-S or [SH]-MJ430-S, a mixture of 100 mg carbon and 100 mg sulfur was heated at 155 ºC for 24 h in a sealed vacuum tube.

3.2.4 *Electrochemical Measurements*

The MJ430-S or [SH]-MJ430-S composite was mixed with carbon nanotubes (CNTs, Sigma-Aldrich) and poly(vinylidene difluoride) (PVDF; MTI Cop.) as the binder in a weight ratio of 80 : 10 : 10, in N-methyl-2-pyrrolidone (NMP; Sigma-Aldrich) as a dispersant. The slurry was cast on an Al foil current collector and dried overnight at 60 ºC under vacuum. A thick cathode with 4mg S cm^{-2} loading was prepared similarly. The slurry was cast on a C-coated Al foil current collector (MTI Corp.). 2032 coin-type cells were assembled using lithium metal (250 mm thick, Alfa Aesar) as the anode, polypropylene (PP) Celgard2500 (Celgard, LLC Corp.) as the separator, and 1 M LiTFSI (Sigma-Aldrich) and 1 wt% $LiNO_3$ (Alfa Aesar) in DOL/DME (Sigma-Aldrich, v/v . 1 : 1) as the electrolyte for each cell. The electrochemical performances of the cells were evaluated at 30 ºC in a voltage window of 1.9–2.8 V vs. Li^+/Li at various C-rates using a battery tester (BT-2043, Arbin).

3.2.5 *Spectroscopic Characterization*

EIS. Electrochemical impedance spectroscopy (EIS) of Li–S cells at different discharge stages was performed using an AMETEK VersaSTAT4 potentiostat/galvanostat in the frequency range of 10^{-2} to 10^{-6} Hz by applying a 5 mV ac oscillation.

NMR. ^7Li, ^{19}F, and ^{13}C MAS NMR were performed on a Varian Inova spectrometer with a 600MHz (14.1 T) magnet, using 1.6mm rotors operating at a spinning speed of 36 kHz. The 90˚ pulse width was 3 μs for ^7Li, 1.5 μs for ^{13}C, and 5 μs for ^{19}F. The ^7Li spectra were obtained with 640 scans, using a flip angle of 9° (a pulse width of 0.3 μs) with a recycling delay of 5 s for quantitative comparison. The ^{19}F spectra were obtained using a spin-echo pulse sequence with 48 scans and a recycling delay of 5 s. Due to the low sensitivity of ^{13}C in the naturally abundant materials, 10240 scans were used with a 30˚ pulse and a recycling delay of 5 s. Temperature was maintained at 25 ºC for all NMR measurements. For the preparation of the first set of samples, concentrated Li_2S_8 in DME with MJ430/20% SH-MJ430 particles was packed into the NMR rotors. For the second series of samples, the cycled coin cells were disassembled at different voltage stages in a glovebox, and the composites were scratched off from the cathodes immediately and filled into the NMR router.

XPS. All XPS spectra were recorded on a Surface Science Instruments S-Probe photoelectron spectrometer. This instrument has a monochromatized Al Kα X-ray source which was operated at 20 mA and 10 kV, and a low energy electron flood gun for charge neutralization. The samples were mounted on double-sided tapes that run as insulators. X-ray analysis area for these acquisitions was approximately 800 μm across. Pressure in the analytical chamber during spectral acquisition was less than 5×10^{-9} torr. The take-off angle (the angle between the sample normal and the input axis of the energy analyzer) was 0°, (0° take-off angle ≅ 100 Å sampling depth). Pass energy for survey and detailed spectra (to calculate composition) was 150 eV. Data point spacing was 1.0 eV per step for survey spectra, and 0.4 eV per step for detailed spectra. Pass energy for high-resolution spectra was 50 eV, with a data point spacing of 0.065 eV. Service Physics Hawk version 7 data analysis software was used to calculate the elemental compositions from peak areas measured above an inelastic scattering background. Powder samples were transported to instrument in air. Cycled cathode samples were disassembled and washed in an Ar atmosphere glovebox, transferred to the instrument in sealed vials, and then mounted under ambient conditions.

3.3 RESULTS AND DISCUSSION

3.3.1 *Introduction of SH-MJ430 Carbon*

As a platform to investigate our multifunctional interface, a commercially available mesoporous carbon host referred to as MJ430 was utilized, with an average surface area of 689 $m^2\ g^{-1}$. A schematic depiction of our approach to confine active materials in the MJ430 pores using a multifunctional thiol surface modifier (SH-MJ430) is shown in Figure 3.4. In our proposed strategy, there are three unique interactions occurring at the cathode interface which contribute to an increase in cell performance. The first is an electrostatic "lithium bond" between solvated Li^+ in the LiTFSI electrolyte and lone pairs on the reduced phenylthiolate moiety ($–S^-$). The second is a similar lithium bond involving the solvated Li^+ tails of dissolved LiPS. Finally, the third interaction is described as covalent disulfide bonding that is formed between $–S^-$ (or phenylthiyl radicals $–S•$) and LiPSs. Evidence supporting each of these proposed interactions is presented in the following sections.

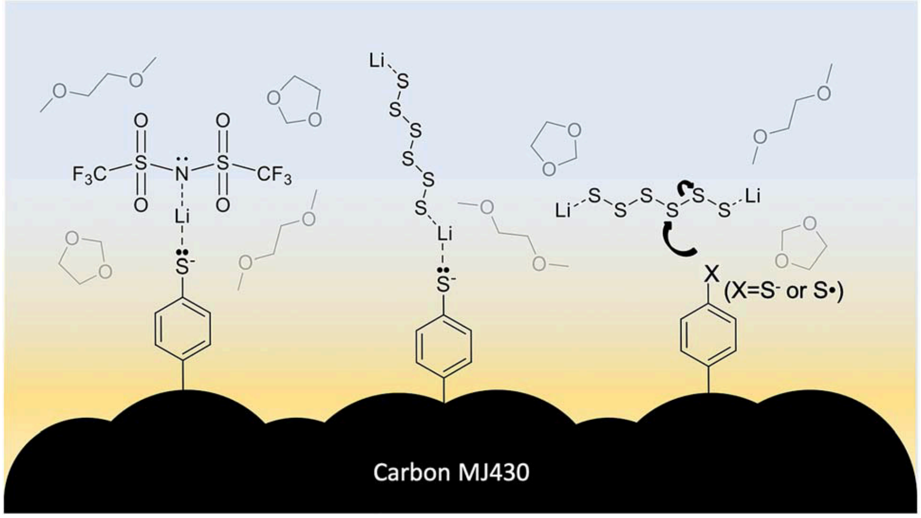

Figure 3.4. Schematic depiction of the multiple interactions of thiol surface modifiers with solvated active materials. Proposed mechanisms include electrostatic interactions with Li^+ (left, middle),

covalent disulfide bonding (right), and the subsequent attraction of solvent molecules to these aggregated charges.

3.3.2 *Characterization of Functionalized SH-MJ430 Carbon*

The functionalization of conductive carbon surfaces is made possible by a one-pot synthetic strategy that utilizes in situ generated diazonium ions from common and inexpensive organic precursors.[124] We prepared a series of samples in which the concentration of surface modifiers was varied between 0 and 20 wt%. A mechanistic schematic of this reaction is shown in Figure 3.5. We sought to confirm the functionalization by both physical and spectroscopic analyses, all of which are reported below. For these experiments, all "pristine" control samples were exposed to the same reaction conditions, barring the organic nitrite reagent which is necessary for diazotization. This was done to ensure that the presence of functional groups was due to covalent anchoring to the surface, rather than physisorption or trapping of thiol precursors in the carbon pores.

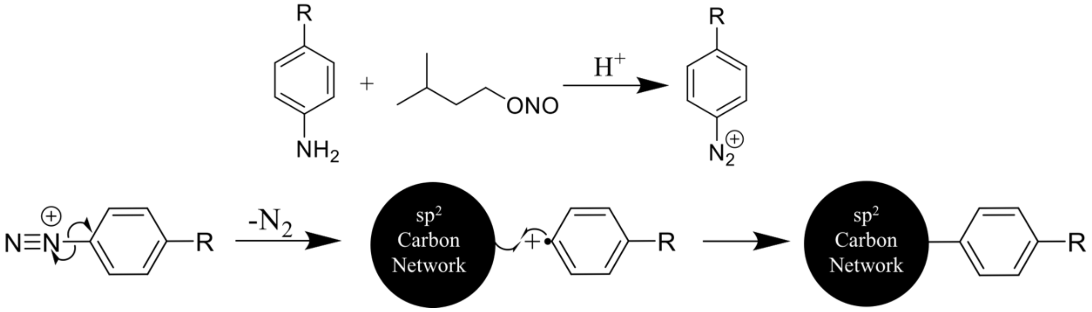

Figure 3.5. Schematic of in-situ functionalization of modifiers ("R"=SH) onto the surface of MJ430 carbon via diazotization. The diazonium ions dissociate into N_2 gas and a phenylthiol radical, which can react with sp^2-hydridized carbon frameworks to form sp^3 C-C bonds. This approach is advantageous for many applications because of the ability to tune the functionality of grafted small molecules, as well as controlling the degree of functionalization.

The addition of mass to carbon particles after a series of surface modifications was tested by TGA (Figure 3.6a). It was found that a maximum of ~ 20 wt% of mass could be added to the pristine particles, as attempts to push reaction equilibrium even further towards functionalization (e.g., by adding 50 mol% diazonium precursors, instead of 20 mol%) yielded inconsequentially increase in mass loss (Figure 3.7). This finding may be attributed to a combination of precursor reactivity and the finite surface area readily available for attachment,[172] which would be optimized in the future such as by selecting other promising nanostructured carbons.

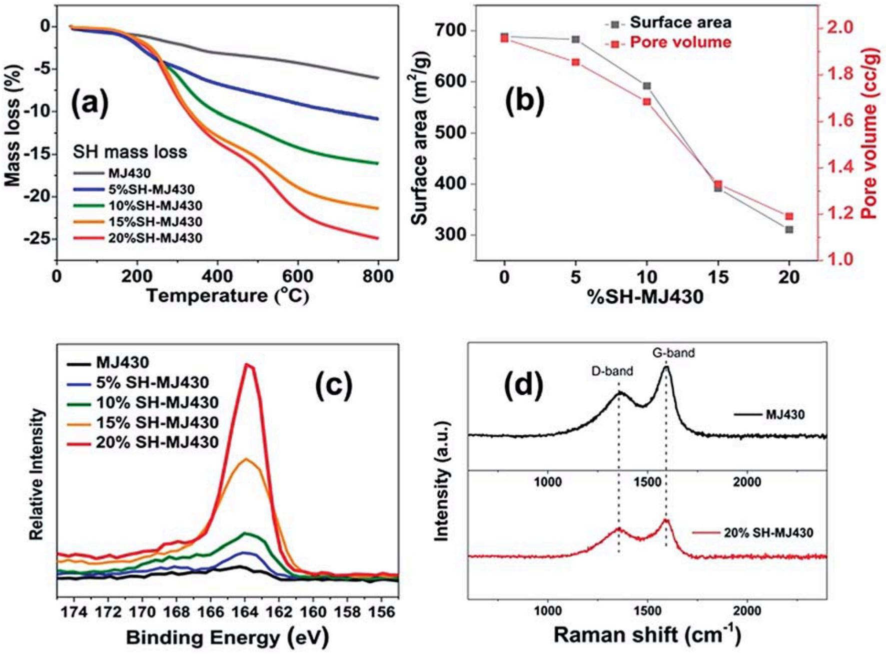

Figure 3.6. Characterization of functionalized [SH]-MJ430 carbons ([SH]= 0, 5, 10, 15, and 20 wt% SH), controlled via reaction conditions. (a) TGA analysis, (b) surface area and total pore volume calculated from the N_2 isotherms analysis, and (c) XPS S_{2p} spectra of a series of [SH]-MJ430 carbons. (d) Raman spectra of MJ430 and 20% SH-MJ430 carbons.

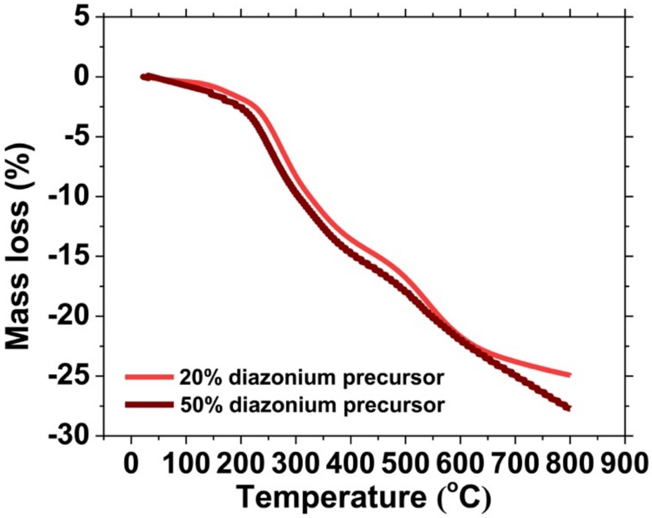

Figure 3.7. TGA of resultant modified MJ430 carbons from mixing purified MJ430 with 20 and 50 mol% diazonium precursors, respectively. The former displays a 25 wt% of overall mass loss (20 wt% among which comes from the modifiers), while the latter only shows a 3% increase of overall mass loss with overwhelming increase of diazonium precursors.

Next, we confirmed that modifiers lined the pores of the host substrate through analysis of N_2 adsorption/desorption isotherms at 77 K (Figure 3.8). From these N_2 isotherms with the Brunauer–Emmett–Teller (BET) and Barrett–Joyner–Halenda (BJH) analysis, an average surface area decrease from 689 to 310 m^2 g^{-1} and a total pore volume (including all types of pores) decrease from 1.96 to 1.19 cm^3 g^{-1} were observed after the maximum modification (Figure 3.7b). The pore size distribution plots reveal a gradual decrease in the primary mesopore size from 7.4 to 5.4 nm (Figure 3.8f).

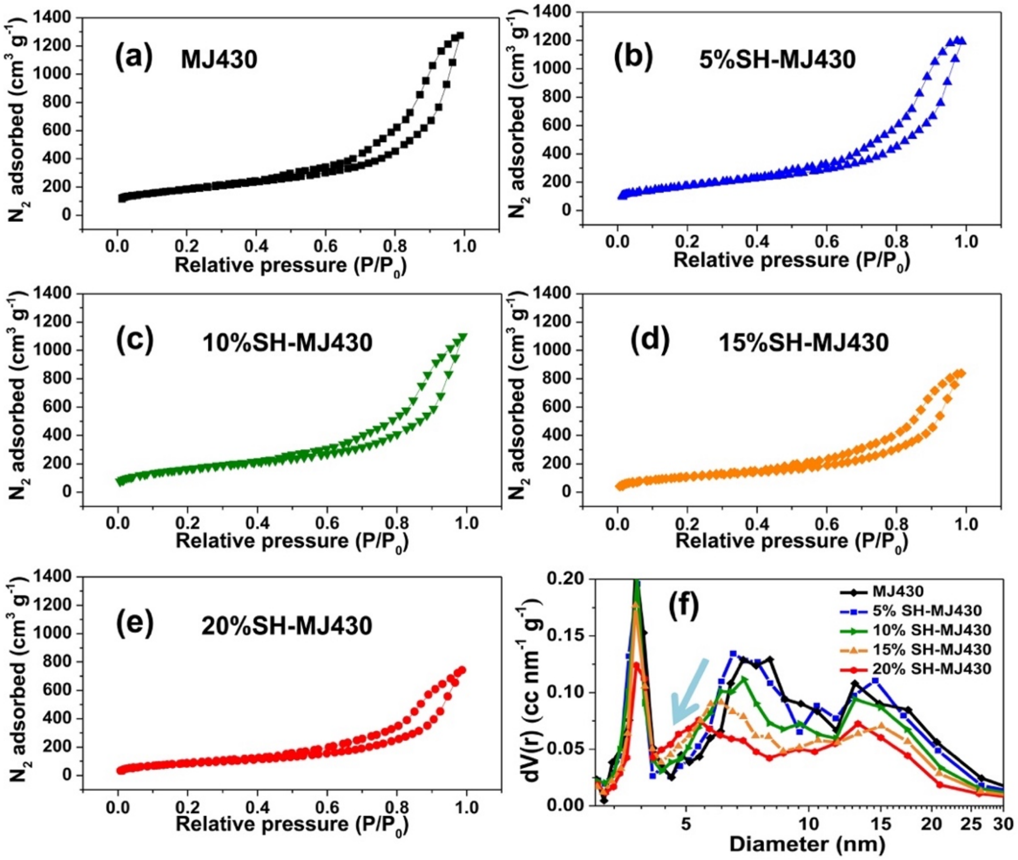

Figure 3.8. The N_2 isotherms at 77 K for the (a) MJ430, (b) 5% SH-MJ430, (c) 10% SH-MJ430, (d) 15% SH-MJ430, (e) 20% SH-MJ430 carbon and (f) their related pore size distribution. The distribution plot of MJ430 reveals that mesoporous carbon MJ430 has three pore types. These pore types originated from capillary condensation in micropores (from the carbon walls), primary mesopores, and secondary mesopores (from interparticle capillary condensation), [173] with pore diameters of approximately 3.8, 7.4, and 14 nm, respectively. After surface modification, the primary mesopores decrease from 7.4 to 5.4 nm, as shown with the arrow.

Moreover, the surface chemical composition of [SH]-MJ430 carbons was determined by XPS. The comparison of S_{2p} XPS spectra (Figure 3.6c) clearly shows an increase in the S signal (observed at 164 eV) as the concentration of precursors is increased, which corresponds to the thiol species.[174] Figure 3.6c is a detailed scan with a relatively low resolution (150 eV pass energy), which is meant to illustrate the intensity of the S signal. The high-resolution S_{2p} spectra (50 eV pass energy) are shown in Figure 3.9c and e. They suggest that only after exposure to the diazonium ions, a doublet peak centered at 164 eV can be observed, reflecting the anticipated spin–orbit splitting of aryl-thiol species after modification.51 In Figure 3.9a, characteristic peaks of C and O atom clearly appear in both MJ430 and 20% SH-MJ430 spectra. Upon further analysis of high-resolution C_{1s} spectra (Figure 3.9b and d), the larger contribution of the C–C signal in the 20% SH-MJ430 sample presumably results from the addition of C–C bonds from the phenylthiol modifiers to MJ430.

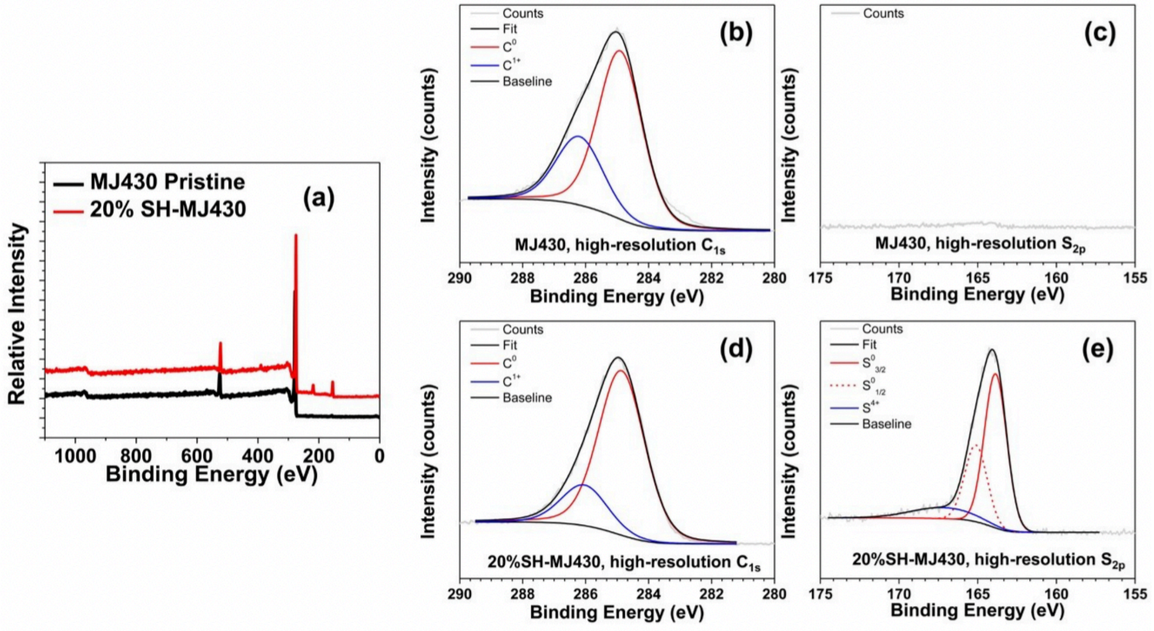

Figure 3.9. (a) XPS wide spectra of MJ430 and 20% SH-MJ430 (O_{1s} 529-535 eV, C_{1s} 284-289 eV, S_{2s} ~ 220 eV, S_{2p} 161-169 eV). High-resolution C_{1s} and S_{2p} spectra of (b,c) MJ430 and (d,e) 20%SH-MJ430 carbon.

Finally, we tested for the degree of defects or disorder in the MJ430 mesoporous carbon before/after thiol modification using the Raman spectrum shown in Figure 3.6d. The intensity ratio of the D (~ 1357 cm^{-1}) and G (~ 1590 cm^{-1}) bands, I_D/I_G, slightly increases from 0.54 to 0.76 after the thiol modification, representing increased defects/disorder of the mesoporous carbon and a decreased average size of the sp^2 conjugated domains in the carbon.[162,175] The relatively low increase in the I_D/I_G value implies that our method results in limited damage to the conjugated structure of the pristine carbon matrix.[155,159] After thiol functionalization, the electrical conductivity of the cathode decreased slightly from 1.51 to 0.50 S cm^{-1}, but this value is still sufficiently high to make an electrochemically active electrode.[176]

Additional insight into how modification affects the physical nature of carbon particles was gained by imaging them using scanning electron microscopy (SEM) and scanning/transmission electron microscopy (S/TEM). No significant difference in carbon morphology was observed by SEM after modification, as shown in Figure 3.10a and d. TEM images show that the transparent mesopores in MJ430 (Figure 3.10b and c) have turned into slightly turbid mesopores with thicker carbon walls after the thiol modification (Figure 3.10e and f), revealing successful implementation of phenylthiol modifiers on the carbon surface. The average thickness of the carbon walls increases by about 1.4 nm after modification, from 1.82 nm to 3.22 nm, which agrees reasonably well with the reduced pore size presented in Figure 3.8f. The 1.4 nm increase of the carbon walls indicates a multi-layer structure of phenylthiol modifiers since the size of the monolayer structure is estimated to be ~ 0.67 nm.[177] This multi-layer structure likely results from hyper-branching of diazonium intermediates during modification, a known process in this type of reaction.[178]

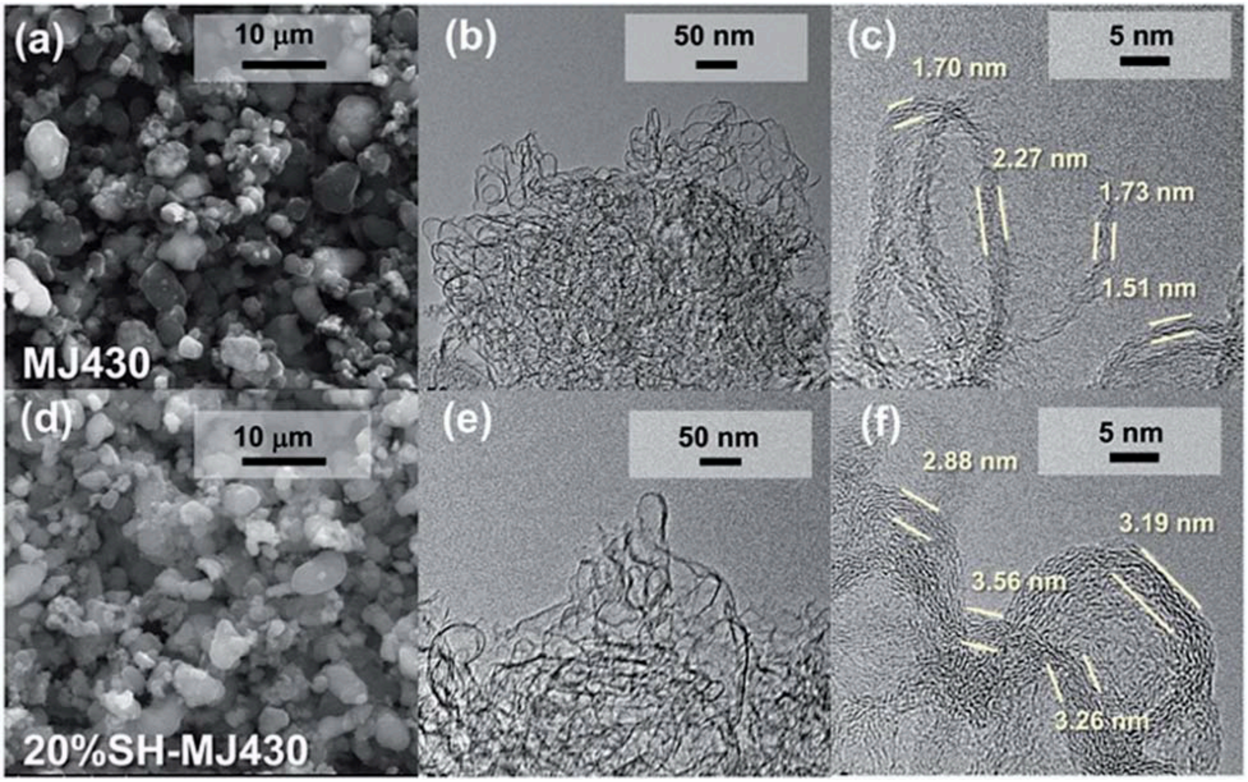

Figure 3.10. SEM and TEM images of (a–c) MJ430 and (d–f) 20% SH-MJ430.

3.3.3 *Electrochemical Performance of Li/S Batteries with SH-MJ430-S Cathodes*

After characterization of the functionalized [SH]-MJ430 carbon, sulfur was infused into MJ430 and [SH]-MJ430 carbon to form MJ430-S and [SH]-MJ430-S composites. The exact weight content of sulfur in the composites was determined by TGA as shown in Figure 3.11. The energy-dispersive spectra (EDS) confirm that the distinguishable S_8 particles (Figure 3.12a) would be encapsulated into the mesopores of 20% SH-MJ430 after being melted at 155 °C, showing uniform distribution of S in the 20% SH-MJ430-S (Figure 3.12b). This is consistent with the drastic decrease of the surface area and pore volume of the carbon matrix after sulfur infiltration, demonstrating good confinement of sulfur atoms inside carbon pores (Figure 3.13).

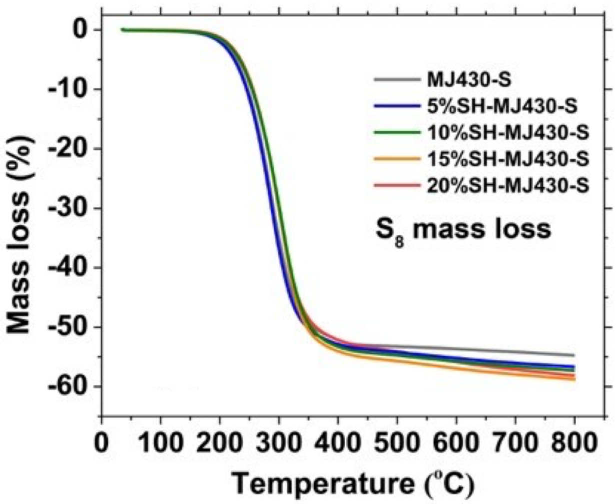

Figure 3.11. TGA of a series of [SH]-MJ430-S composites with an increasing weight percentage of the thiol modifier from 0% to 20%, controlled via reaction conditions.

(a) 20% SH-MJ430 + S_8 physical mixing at room temperature

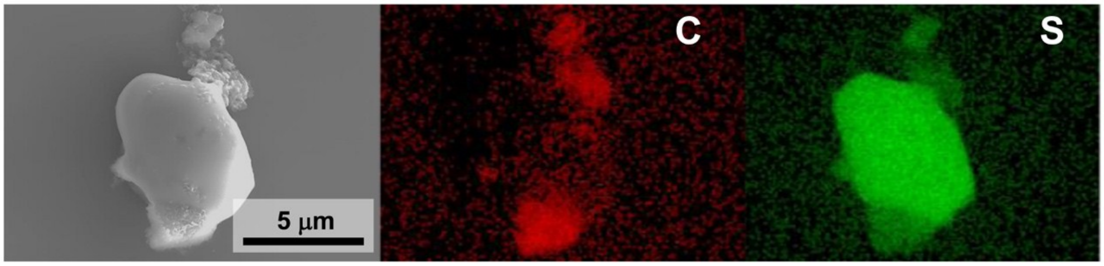

(b) 20% SH-MJ430-S after S_8 infiltration at 155 °C

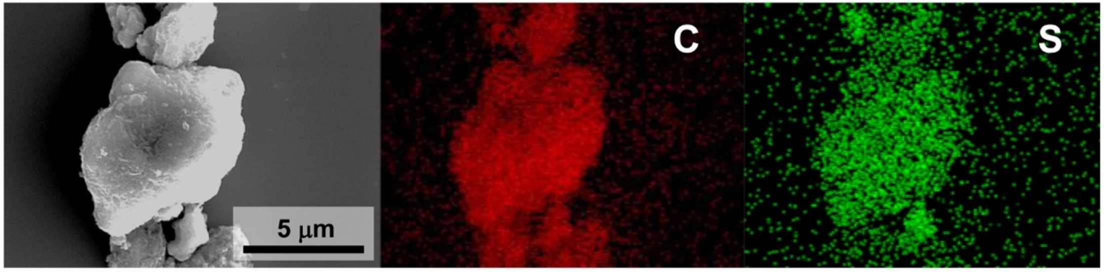

Figure 3.12. EDS elemental mapping images and the corresponding selected SEM images of (a) the physically mixed 20% SH-MJ430 and S_8 powders at room temperature and (b) 20% SH-MJ430-S powders after S_8 infiltration at 155 °C.

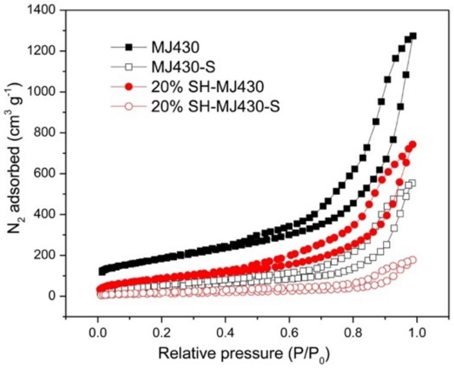

Figure 3.13. N_2 isotherms for the MJ430, 20% SH-MJ430, MJ430-S, 20% SH-MJ430-S. Surface area and pore volume of the composites are 170 m^2 g^{-1} and 0.876 cm^3 g^{-1} for the MJ430-S and 52.0 m^2 g^{-1} and 0.271 cm^3 g^{-1} for the 20% SH-MJ430-S, respectively.

The discharge/charge voltage profiles of MJ430-S and 20% SH- MJ430 cathodes at 0.05C for the first two activation cycles and at 0.25C for the following cycles (1C = 1672 mA g^1) are shown in Figure 3.14a. Initially, a sulfur loading of ~ 1 mg cm^{-2} was utilized to compare with reported work on Li–S batteries, most of which use very thin (< 2 mg cm^{-2}) S electrodes.[128,150,169,170] The voltage profile features of the electrodes reflect those expected of a Li–S system, consisting of two discharge plateaus at 2.3 V and 2.1 V.[123] In the initial charge process, the MJ430-S cathode shows an obvious overcharging behavior at 2.37 V, which is attributed to the occurrence of redox shuttling of dissolved LiPSs.[179,180] Briefly, the dissolved LiPSs escaping from the cathode are continuously reduced at the anode and oxidized at the cathode, shuttling back and forth between each event. This behavior is inhibited in the 20% SH-MJ430-S cathode indicating an efficient protection of LiPS diffusion from the cathode to the Li anode, due to the interactions of the SH modifiers with LiPSs. Figure 3.14b compares the corresponding long-term cycling performance of MJ430-S and 20% SH-MJ430-S cathodes. As expected, the modified cathode displays an obvious improvement in capacity retention. The capacity of the unmodified MJ430-S decreased from 812 to 486 mAh g^{-1} at 0.25C (a capacity retention of 60%) after 300 cycles. Over the same number of cycles, the 20% SH-MJ430-S cathode shows a capacity retention of 89%, with the discharge capacity dropping from 838 to 745 mAh g^{-1}.

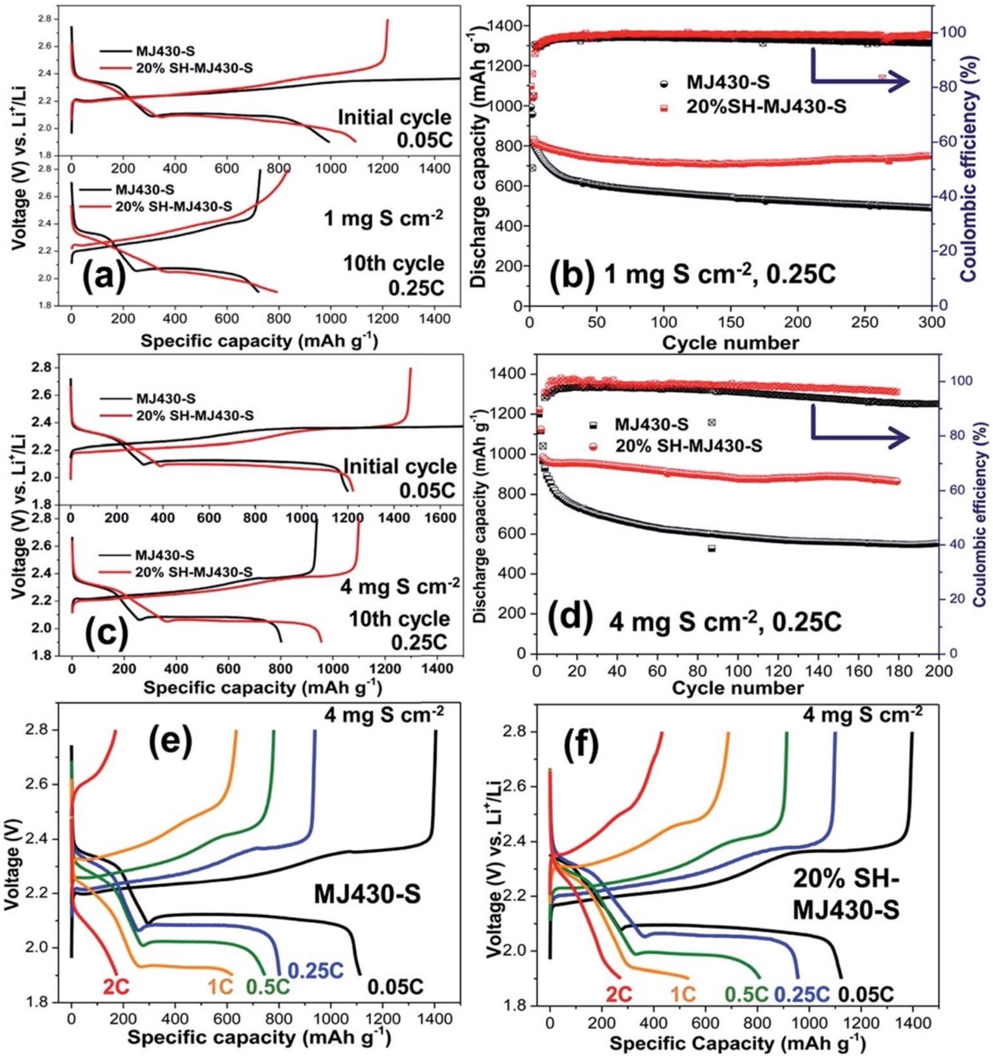

Figure 3.14. (a) The discharge/charge voltage profiles of MJ430-S and 20% SH-MJ430-S electrodes based on a S loading of 1 mg cm^{-2} the initial activation cycle (0.05C) and the 10th cycle (0.25C) and (b) the corresponding cycling performance within the first 300 cycles. (c) The discharge/ charge voltage profiles and (d) the corresponding cycling performance of MJ430-S and 20% SH-MJ430-S electrodes based on a S loading of 4 mg cm^{-2}. The discharge/charge voltage profiles of (e) MJ430-S and (f) 20% SH-MJ430-S electrodes at various rates.

The enhanced capability of LiPS trapping in the 20% SH- MJ430-S cathode (1 mg S cm^{-2}) due to our modified surface allows us to address critical concerns in developing high-S- loaded Li–S cells, providing an effective means to increase the areal capacity of the resultant batteries. The thiol modifier could also enhance the electrolyte wettability of electrodes by creating a more polar electrode surface, which is equally beneficial for the high-sulfur-loading cathodes. The electrochemical performance of MJ430-S and 20% SH-MJ430-S cathodes with a high sulfur loading of 4 mg cm^{-2} is evaluated in Figure 3.14c and d. In Figure 3.14c, the thick MJ430-S and 20% SH-MJ430-S cathodes deliver higher discharge capacities than the thin electrodes in Figure 3.14a, due to the improved electrical conductivity of C-coated Al foil current collectors used in our high loading cells. More interestingly, the decreased coulombic efficiency of MJ430-S and 20% SH-MJ430-S cathodes (Figure 3.14d) suggests a severe dissolution of LiPSs in the thick cathodes. After 180 cycles, the MJ430-S cells show a poor cycling retention of 56% at 0.25C (556 mA h g^{-1}, Figure 3.14d), whereas the capacity retention in the 20% SH-MJ430-S cells remains at 87% (865 mA h g^{-1}, Figure 3.14d). We attribute the enhanced capacity retention of 20% SH-MJ430- S cells to the improved wettability and the restriction of LiPS dissolution in the modified cathode.

The rate capability of MJ430-S and 20% SH-MJ430-S cells is exhibited in Figure 3.14e and f. After the activation cycles, the discharge capacities of 20% SH-MJ430-S at 0.05, 0.25, 0.5, 1, and 2C are 1121, 956, 811, 537, and 270 mA h g^{-1}, respectively. Upon close examination of the discharge curves of MJ430-S and 20% SH-MJ430-S cells, we can find an increased polarization in 20% SH-MJ430-S compared to MJ430-S especially for the second discharge plateau. This difference of the second discharge plateau is consistent with the distinction in the cyclic voltammogram of MJ430-S and 20% SH-MJ430-S cells (Figure 3.15). After modification, a distinction is recognized that the second reduction peak (~ 2.05 V for the MJ430-S) becomes broad and is shifted to ~ 2.02 V, which indicates that the thiol interface plays a significant role in the reduction of soluble LiPSs. The mechanism by which LiPSs dissolve and disproportionate will be further explored in the following sections.

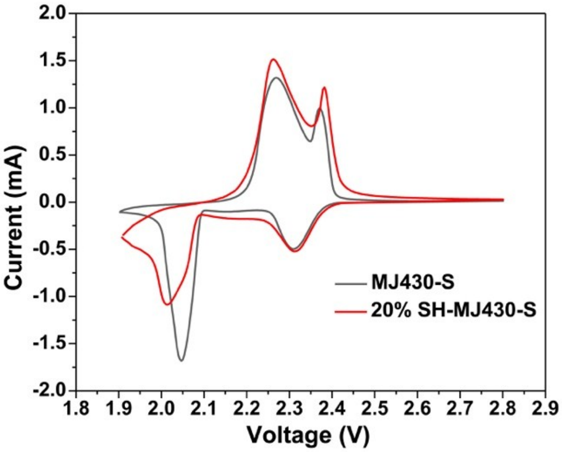

Figure 3.15. CV of the Li/S cells using MJ430-S and 20% SH-MJ430-S cathodes at the seep rate of 0.02 mV s^{-1}.

Furthermore, to investigate the relationship between the thiol modifiers and the resultant electrochemical overpotentials, the electrochemical performance of [SH]-MJ430-S cathodes ([SH] = 0, 5, 10, 15, 20 wt% SH) is investigated in Figure 3.16a and b. A gradual reduction in overpotential was observed as the concentration of SH modifier decreases (Figure 3.16a), whereas 20 wt% SH- MJ430-S still displays the highest discharge capacity after long-term cycling (Figure 3.16b). Moreover, the SEM images of cycled 20% SH-MJ430-S cathodes (Figure 3.17) show less pulverization of carbon particles upon repeated cycling, suggesting that the amorphous surface film produced by our modifiers can also enhance the long-term mechanical integrity of the electrode.

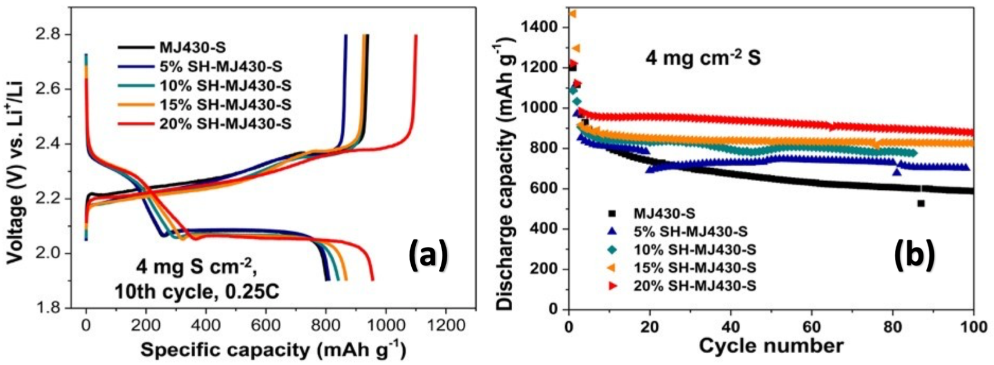

Figure 3.16. (a) The discharge/charge voltage profiles and (b) their cycling performance of a series of [SH]-MJ430-S composites with an increasing weight percentage of the thiol modifier from 0% to 20%, controlled via reaction conditions.

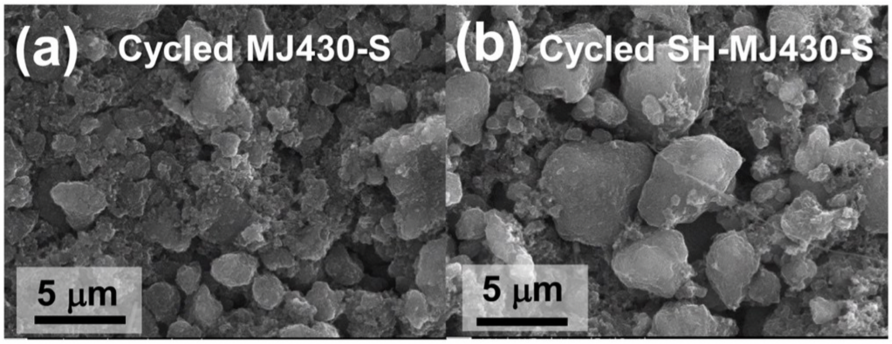

Figure 3.17. SEM images of (a) MJ430-S and (b) 20% SH-MJ430-S cathode discharged to 1.9 V after long-term cycling.

The thick cells were discharged at a relatively low rate (0.25C) to prevent the problems of the Li anode during cycling, including dendrite formation, pulverization, and solid electrolyte interphase buildup.[141] The SEM images of the Li metal surface before and after long-term cycling are shown in Figure 3.18. In comparison to the rough surface with a thick passive interphase in the MJ430-S cell (Figure 3.18b), the cell with the 20% SH-MJ430-S cathode showed a smoother surface of Li metal (Figure 3.18c) although it was still covered by some particles, the so-called lithium dendrites.[181] The severe passive interphase in the MJ430-S cell is probably formed by the reaction of dissolved LiPSs with the Li and electrolyte. Future work associated with the anode will be pursued to achieve high discharge/charge current densities.[182–184]

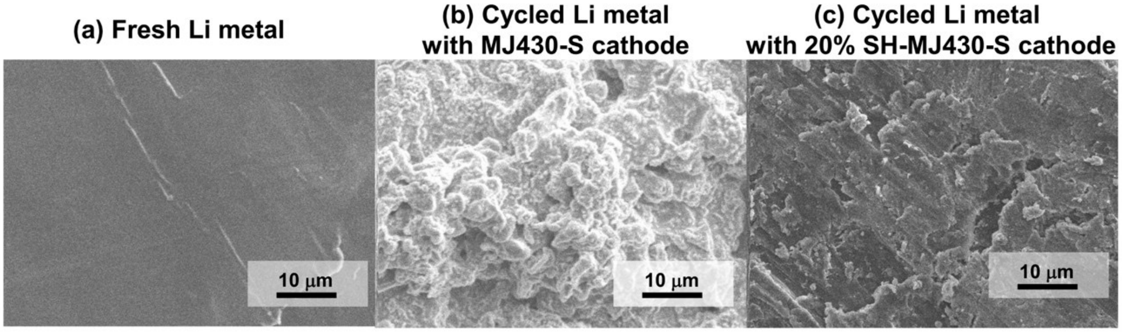

Figure 3.18. SEM images of the Li metal surface (a) before and (b) after the cycling process with the MJ430-S cathode and (c) with the 20% SH-MJ430-S cathode.

The electrochemical performance of 20% SH-MJ430-S with a high sulfur loading resembles those of the state-of-the-art Li–S battery systems, as listed in Table 3.1. In the future, we will explore the surface modification of other highly sp^2-hybridized carbons (e.g., CNTs) to provide an interconnected conductive scaffold, reduce polarization, and achieve higher energy densities in particular for the long-term cycle performance of Li–S batteries. In this thesis, however, considering the complexity of surface modification of CNTs and graphene as mentioned in the introduction, we adopt the mesoporous carbon matrix as the platform to isolate the additional effects of CNTs and graphene on the SH-modified cells, even though the mesoporous carbon matrix would compromise the overall cycling performance of Li–S batteries.

Table 3.1. Electrochemical performances for representative Li/S batteries in comparison to this work.

Cathode components	Active materials	Areal S Loading (mg cm^{-2})	Electrolytes	Cycling performance (based on S loading mass)				
				C Rate	Initial Discharge Capacity (mAh g^{-1})	Cycle Numb-er	Residual Reversible Capacity (mAh g^{-1})	Capacity Decay/ Cycle (%)
20%SH-MJ430-S (this work)	Melt-infiltrated S_8	4.0	1M LiTFSI-DOL/DME(1:1)+1wt%$LiNO_3$	0.25C	956	180	865	0.05
Mo_2C/Carbon Cloth-S[185]	Melt-infiltrated S_8	1	1M LiTFSI-DOL/DME (1:1)+1.5wt%$LiNO_3$	0.2C	1177	300	789	0.11
		4.68		0.1C	692	50	500	0.55
$NiCo_2S_4$@Carbon textile[186]	Li_2S_6 catholyte	1.5	1M LiTFSI-DOL/DME (1:1) + 0.2M Li_2S_6	0.1C	1600	100	1100	0.31
				0.5C	923	500	836	0.02
HCNCs[a]/S[187]	Melt-infiltrated S_8	1.4	1M LiTFSI-DOL/DME(1:1)+0.1M $LiNO_3$	1C	852	300	630	0.09
		4		0.2C	883	100	622	0.30
Ketjen black-S with plasma-modified separators[188]	Melt-infiltrated S_8	-	1M LiTFSI-DOL/DME(1:1)+0.1M $LiNO_3$	0.2C	988.9	100	798.5	0.19
amCMK-S[155]	Li_2S	-	1M LiTFSI-DOL/DME(1:1)+0.25M $LiNO_3$	0.2C	1211	100	920	0.24
N-Doped HCS[b]-S[189]	Melt-infiltrated S_8	0.5-0.7	1M LiTFSI-DOL/DME(1:1)+0.4M $LiNO_3$	0.2C	1113	100	980	0.12
HCv[c,190]	Melt-infiltrated S_8	1	1M LiTFSI-DOL/DME(1:1)+0.1M $LiNO_3$	0.2C	1380	150	730	0.31
TiO@C-HS[d]/S[191]	Melt-infiltrated S_8	4	1M LiTFSI-DOL/DME(1:1)+0.2M $LiNO_3$	0.05C	886	50	821	0.14
Graphene-S[134]	Graphene-enveloped micron sized S	1.2	1M LiTFSI-DOL/TEGDME(1:1)	0.2C	705	50	500	0.58
MWCNT-S with VACNT[e,136]	Melt-infiltrated S_8	6.3	1M LiTFSI-DOL/DME(1:1)+0.25M $LiNO_3$	0.05C	995	150	696	0.2
IKB[f]-S[142]	Melt-infiltrated S_8	3.5	1M LiTFSI-DOL/DME(1:1)+0.1M $LiNO_3$	0.1C	1000	100	750	0.25
Nano-S@PEDOT[60]	S nanoparticles	1.66	1M LiTFSI-DOL/DME(1:1)	0.25C	1120	50	930	0.34
S@ZIB-8[g,144]	Melt-infiltrated S_8	1	0.6M LiTFSI-DOL/DME(1:1)+0.1M $LiNO_3$	0.5C	750	250	600	0.08
Graphene-S63 hybrid[163]	G-S hybrids	1.26	1M LiTFSI-DOL/DME(1:1)+0.5wt%$LiNO_3$	0.45C	725	100	541	0.25
		4.6		0.2C	1200	100	822	0.32

N,S-codoped graphene-S[146]	Li_2S_6 catholyte	8.5	1M $LiCF_3SO_3$ DOL/DME (1:1) + 0.1M $LiNO_3$	0.5C	925	200	670	0.14
polySGN[192]	S-rich copolymer	3.7	1.85M $LiCF_3SO_3$ DOL/DME (1:1) + 0.1M $LiNO_3$	0.2C	978	100	655	0.33
		10.5		0.1C	992	100	717	0.28
CATB-coated nanoS-GO[156]	S-GO nanocomposites	0.8	1 M LiTFSI in $PYR_{14}TFSI$/DOL/DME mixture (2:1:1) + 0.1M $LiNO_3$	1C	880	160	780	0.07
Porous CNTs-S with Graphene/DTT additional interlayer[160]	Melt-infiltrated S_8	3.51	1M LiTFSI-DOL/DME(1:1)+1wt%$LiNO_3$	0.2C	1262	200	984	0.11
PEI[h]-CNT-S[162]	Melt-infiltrated S_8	1.2	1M LiTFSI-DOL/DME(1:1)+0.2M $LiNO_3$	0.5C	949	300	750	0.07
S-GSH[i,169]	S-rich copolymer	1	1M LiTFSI-DOL/DME(1:1)+1wt% $LiNO_3$+ 0.02 M Li_2S_8	1C	985	450	857	0.03
S-TTCA[j,170]	S-rich copolymer	0.8	1M LiTFSI-DIOX/TEGDME (1:1) +0.2M $LiNO_3$	0.2C	1050	100	945	0.08
S-DIB-OLC[k,171]	S-rich copolymer	3-5	1M LiTFSI-DOL/DME(1:1)+0.25M $LiNO_3$	0.1C	1150	100	880	0.24
PVDF-S with VGCF-PEOCMC interlayer[193]	S_8	5	1M LiTFSI-DOL/DME(1:1)+1wt%$LiNO_3$	0.06C	650	100	600	0.08
70S/d-Ti_2C[194]	Nano-S	1	1M LiTFSI-DOL/DME(1:1)+2wt%$LiNO_3$	0.5C	1071	650	723	0.05

[a] Hollow Carbon Nanosphere Clusters (HCNCs); [b] Hollow Carbon Spheres (HCS); [c] Hollow Carbon Fiber (HCF); [d] Hollow Spheres(HS); [e] Vertically Aligned CNTs (VACNTs) as the binders for the hierarchical free-standing paper cathode; [f] Integrated Ketjen Black with conductive amorphous carbon as a "binder" (IKB); [g] A metal-organic framework (MOF), assembled by Zn ions and 2-methylimidazolate (ZIF-8); [h] Polyethylenimine (PEI); [i] Copolymerization of sulfur with Sulfydryl-functionalized rGO (GSH) to form sulfur copolymers; [j] Copolymerization of sulfur with porous trithiocyanuric (TTCA) frameworks; [k] the sulfur-rich copolymer cathode was synthesized via inverse vulcanization of sulfur and 1,3-diisopropenylbenzene (DIB) while using carbon onions (OLC) as hosts.

3.3.4 *Spectroscopic Analysis of Interactions between Solvated Active Materials and Electrode Surfaces*

NMR. As discussed above, the improved capacity retention of MJ430-S cathodes with thiol modifiers is presumed to strongly correspond to the multifunctional interactions on the thiol surface, especially during the second discharge stage. To verify our postulated electrostatic interactions of the thiol groups with active materials, solid-state magic angle spinning (MAS) NMR was performed on various samples to reveal the changes in the atomic environments. Here ^{7}Li, ^{13}C, and ^{19}F NMR were collected on two sets of samples to probe the various possible interactions. In the first set, the ^{7}Li spectra show the interactions of MJ430/20% SH-MJ430 carbon with a concentrated Li_2S_8 solution in DME. In Figure 3.19, the spectra of both samples can be fit using two Lorentzian peaks. Here we assign the upfield resonance at 1 ppm to long chain Li_2S_n (n = 6, 8), and the downfield resonance at around 0 ppm to its short chain byproducts Li_2S_n (n = 2 and 4) of the dynamic equilibrium in LiPS solutions.[195] It has been both theoretically and experimentally documented that Li^+ coordinated by the Lewis-basic donors results in a downfield shift of around 0.5 ppm,[196] so the shift from MJ430 to 20% SH-MJ430 was attributed to the formation of electrostatic Li bonds between the terminal Li in LiPSs and the filled p-orbitals of S from the thiol surface. This result suggests that our surface modifiers can interact with LiPSs in organic solvents even without applying an external bias to electro- chemically drive disulfide bonding.

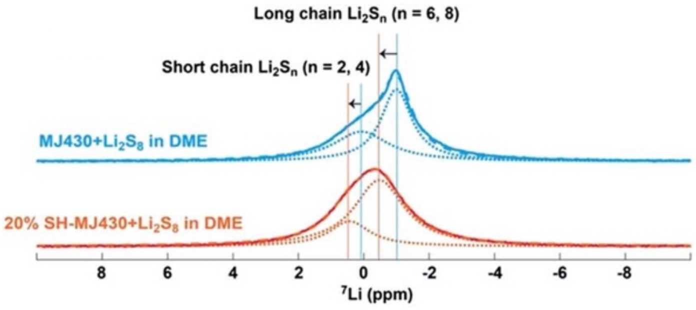

Figure 3.19. ^{7}Li MAS NMR spectra of Li_2S_8 solution interacting with the MJ430 and 20% SH-MJ430, with experimental data in solid lines, deconvolution peaks in dotted lines, and the sum of deconvolution peaks in dashed lines.

To further understand the effect of a thiol surface on battery performance, our second set of samples are cathode materials from cycled cells discharged to different voltages (1.9 V and 2.1 V). All the samples are acquired without them being washed to capture both soluble and insoluble species. Figure 3.20a shows ^{7}Li MAS NMR spectra after normalizing to the weight of active materials packed in rotors. While the resonances at 2.5 ppm and 1.2 ppm are attributed to solid Li_2S and solid Li_2S_n, respectively,[197] the relatively broad peak at 1 ppm includes the signals from solution Li_2S_n and LiTFSI that is confined on the carbon surface or inside the nanoscale pores.[125] The ^{19}F signal at around 80 ppm and the ^{13}C signal at 121 ppm in Figure 3.20b and c both confirm the presence of the confined LiTFSI solution. The relatively sharp ^{7}Li signal at around 1 ppm (Fig. 5b) shown only in 20% SH-MJ430-S suggests the existence of mobile Li^+ species surrounded by solvent molecules in the modified cathodes. As a result, the existence of mobile Li^+ species implies that the surface modification improves the integration of electrolyte into the cathode matrix, probably due to the dipole– dipole interaction of thiol groups with solvated Li^+ and with polar molecules or moieties from the electrolyte.

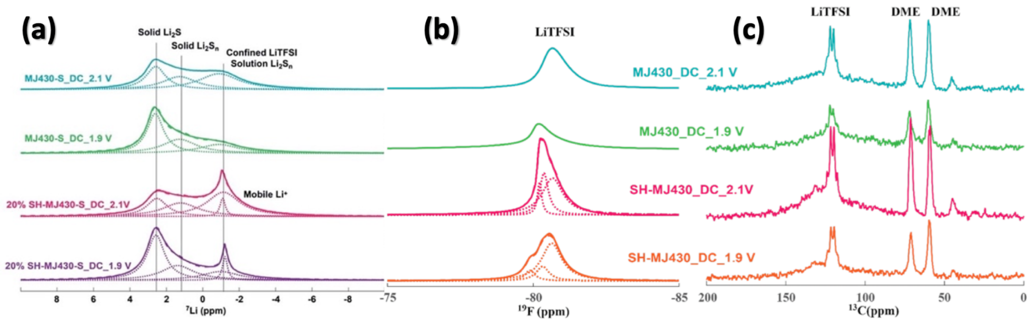

Figure 3.20. (a)^{7}Li, (b) ^{19}F, and (c) ^{13}C MAS NMR spectra of cathode materials with the MJ430-S and 20% SH-MJ430-S from Li–S cells that are discharged to different voltages, with experimental data in solid lines, deconvolution peaks in dotted lines, and the sum of deconvolution peaks in dashed lines.

The improved wettability was further confirmed by the contact angle analysis in Figure 3.21. The angle at the electrolyte/MJ430-S electrode interface is 24°, while that at the electrolyte/20% SH-MJ430-S electrode interface is 8°. This suggests stronger adhesion between the electrolyte and the 20% SH-MJ430-S than that at the electrolyte and the MJ430-S interface, which would significantly confine the LiTFSI-DOL/DME electrolyte with dissolved LiPSs inside the cathode. The different contact angle at the H_2O/MJ430-S and H_2O/20% SH-MJ430-S interface also verify the improved wettability of modified SH-MJ430-S cathode. This effect could lead to improved utilization of active materials during cycling, since better access to the electrolyte within pores would aid in solvation and confinement of solvated LiPSs. This is consistent with the integration area of each deconvolution peak in Figure 3.20a (Table 3.2), which shows that the amount of LiPSs and LiTFSI increases by 50% in the modified electrode when discharged to 2.1 V and these LiPSs are further reduced to solid Li_2S at 1.9 V increasing the accumulation of Li_2S. The downfield chemical shift at 1 ppm in the powder materials (Figure 3.19) is not observed in the cycled cells (Figure 3.20a), perhaps due to the fact that Li^+ is in great excess to the SH-thiol modifiers in the cycled cells (~1 Li^+ to 0.1 SH). Therefore, the electrostatic Li bond does not contribute as significantly as in the powder materials where Li^+ is comparable to the SH-thiol modifiers (~1 Li^+ to 1.6 SH).

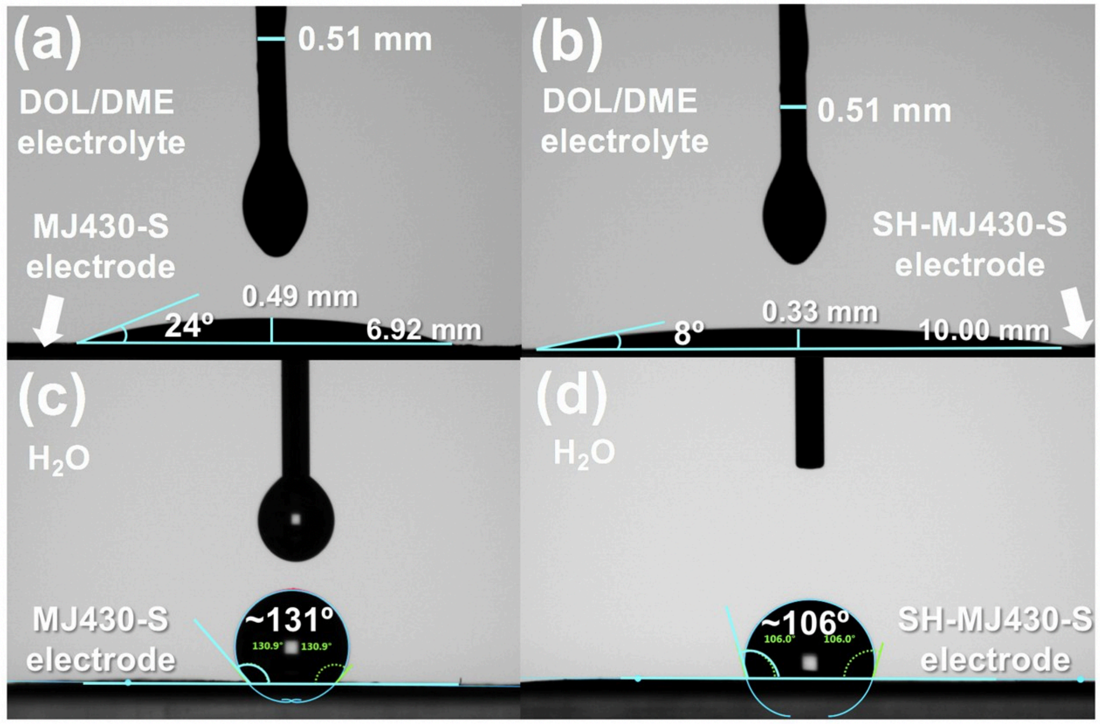

Figure 3.21. The contact angle analysis of (a) MJ430-S and (b) 20% SH-MJ430-S cathode with LiTFSI-DOL/DME electrolyte, as well as (c) MJ430-S and (d) 20% SH-MJ430-S cathode with H_2O. The photographs were obtained by dropping the same amount of electrolyte or H_2O onto the MJ430-S/20% SH-MJ430-S electrode.

Table 3.2. Peak width (PW) and integrated area of individual deconvolution peaks in Figure 3.20a, the integration is normalized to MJ430-S_2.1V (the sum of its three peaks is 1.0).

	Solid Li_2S		Solid Li_2S_n		Confined LiTFSI Solution Li_2S_n		Mobile Li^+	
	PW (ppm)	Integration	PW (ppm)	Integration	PW (ppm)	Integration	PW (ppm)	Integration
MJ430-S_2.1V	0.66	0.30	1.14	0.29	1.34	0.41	-	-
MJ430-S_1.9V	0.55	0.68	1.12	0.49	1.33	0.37	-	-
20% SH-MJ430-S_2.1V	0.67	0.31	1.17	0.40	1.08	0.66	0.17	0.08
20% SH-MJ430-S_1.9V	0.58	0.93	1.09	0.56	1.2	0.37	0.16	0.14

XPS. With strong evidence to support the reaction mechanisms through changes in the Li^+ environment, we utilized XPS to spectroscopically identify changes of sulfur speciation in cycled cathodes. Although S_{2p} high-resolution analysis can determine the difference between S–S bonds (S^0; 164 eV) and S^-Li^+ bonds (S^1; 161 eV),[198–200] it cannot distinguish between physisorbed and chemically anchored S species. Thus, to minimize convolution from non-surface bound sulfur species, cycled cathodes were thoroughly washed with DOL/DME to remove any soluble sulfur species, which presumably includes all polysulfides not bound to the surface. The comparative photoelectron spectra of modified and pristine cathodes are shown in Figure 3.22. The successful removal of non-surface- bound sulfur species was confirmed by the unmodified cathode spectrum, Figure 3.22a. Only very minor photoelectron signals at 161 or 164 eV, which correspond to the tail and core sulfur species of LiPS, respectively, are detectable, indicating that virtually all free LiPSs have been removed. This is in contrast to the spectra in Figure 3.22b, which shows a large signal for both states of sulfur, suggesting that despite thorough washing, LiPS chains remain tethered to the electrode surface with the thiol modifiers via covalent disulfide bonds. During repeated discharge/charge processes, the thiol modifiers are primarily regarded as thiolates ($–S^-$) and thiyl radicals (–S•) in the electrochemical system.[167] The oxidized species in both XPS samples are of indefinite origin; however, we note that a sulfite (SO_3^-) signal at 167 eV is detectable even in as-received carbon samples, potentially indicating its origin as a byproduct of manufacturing, rather than cell-related processes.

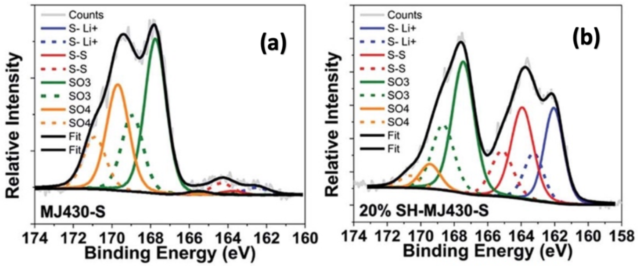

Figure 3.22. High resolution S_{2p} XPS spectra of (a) MJ430-S and (b) 20% SH-MJ430-S cathodes, obtained from Li–S cells discharged to 1.9 V after 100 cycles.

EIS. In our cells, we observe an additional rate-dependent overpotential in modified cathodes (Figure 3.14), which is indicative of a kinetic-limiting chemical reaction occurring as a result of thiol modification. To further discern this influence, EIS was performed on the cells with/without SH modifiers at different stages of discharge within 40 cycles. The Nyquist plots are shown in Figure 3.23a-j. In order to obtain mechanistic insights from these plots, we fitted the impedance data using an electric equivalent circuit (EEC, Figure 3.23k) and the element values derived from the EEC fit are summarized in Figure 3.23k and l.

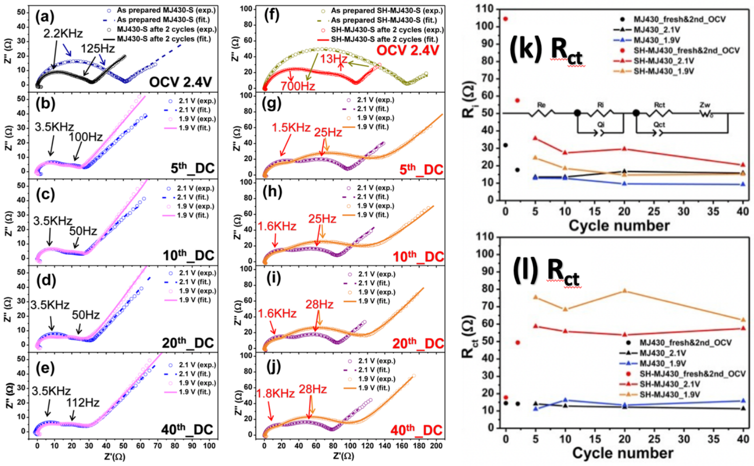

Figure 3.23. EIS analysis of (a-e) MJ430-S and (f-j) 20% SH-MJ430-S cells at different stages of discharge within 40 cycles. Fitted values of (k) the interface resistance R_i and (l) the charge transfer resistance R_ct of MJ430-S and 20% SH-MJ430-S cells at different voltage stages. The electric equivalent circuit (EEC) used to fit impedance data is an inset in (k).

The EEC has been successfully applied for Li-ion and Li/S batteries previously.[158,201] It contains the following serial-connected elements: a bulk internal resistance (R_e), a high-frequency interphase resistance (R_i) in parallel with a constant phase element (Q_i), a mid-frequency charge transfer resistance (R_ct) in parallel with a constant phase element (Q_ct), and a Warburg diffusion element (Z_w). In the as prepared Li/S (MJ430-S) cell, R_i can be clearly observed even though there is no thiol modifier on the carbon surface and no surface film generated by cycling (Figure 3.23a). It is known that carbon surfaces can be unintentionally functionalized by environmentally abundant elements or groups, such as -O, -H, and -OH, etc., during the synthesis and storage, especially for the type of mesoporous carbon used in this thesis.[202] These functional groups could easily transfer to sulfur surface during the infusion process and form a surface film, which impedes the Li^+ transport.[203] Thereby, we speculate that R_i and Q_i associated with the high frequency semicircle should originate from this kind of surface film. The observation that R_i will decrease with extended cycling well supports this speculation, since the electrochemical cycling gradually removes the functional groups and thus improve the electrolyte wetting. By comparing the plots of as-prepared cells held at the open circuit (Figure 3.23a and f), we observed that the high-frequency interphase resistance (R_i) of the 20% SH-MJ430-S cathode ($R_\mathrm{i,fresh,SH} = 104.5\ \Omega$) is three-fold higher than that of the cells with MJ430-S cathodes ($R_\mathrm{i,fresh} = 31.8\ \Omega$). The large increase in $R_\mathrm{i,fresh}$ after the modification is primarily ascribed to the reduced lithium diffusion in the thicker surface film produced by the modification. After two formation cycles, R_i values of both MJ430-S and 20% SH-MJ430-S cells dramatically decrease, likely attributable to the redistribution of sulfur species on the surface of the carbon host, allowing for better interface contacts.

The comparable mid-frequency charge transfer resistance $R_{ct,fresh}$ after the modification ($R_{ct,fresh,MJ430}$ =14.4 Ω vs. $R_{ct,fresh,SH\text{-}MJ430}$ =17.7 Ω) suggests that electron and lithium transport across solid/liquid interface in the initial charge transfer process is not significantly affected, even though the modified cathodes have a thicker surface film. This may be due to the highly conductive carbon hosts and improved electrolyte wettability, which facilitates the charge transfer between the electrolytes and S particles. The electrical conductivity was also measured using a four-point probe technique. It showed an electrical conductivity of 48 S m^{-1} after the modification, which should still be sufficient for electron conduction throughout the entire cathode in Li/S cells.[154,171,204,205]

In contrast, R_{ct} of the 20% SH-MJ430-S cathode quickly increases ($R_{ct,fresh,SH}$ = 17.7 Ω vs. $R_{ct,2nd,SH}$ = 49.4 Ω) and continues growing to 70–80 Ω in the following cycles (Figure 3.23f-j), while R_{ct} of the cell with the MJ430-S cathode remains constant (~15 Ω) upon cycling. The growth of $R_{ct,SH}$ is likely related to the kinetically limiting formation of covalent disulfide bonds with thiol modifiers. Additionally, we notice a ~10 Ω increase in $R_{ct,SH}$ when the 20% SH-MJ430-S cell is discharged from 2.1 to 1.9 V (Figure 3.23g-j). We hypothesized that the increased resistance at lower potentials may be caused in part by an increasing activation barrier for further reduction of polysulfide chains tethered to the surface. Therefore, we suggest that the kinetic limitation after the modification is partially due to the need to drive additional surface reactions (formation of disulfide bonding), and partially due to a thickening of the dynamic semi-solid layer of the active material within cathode pores (a result of more, and stronger, interaction modes with LiPSs), which hinders Li^+ diffusion within the carbon matrix.

3.4 CONCLUSION

In summary, the utility of a thiol-based, multifunctional, redox-active interface has been demonstrated for LiPS-trapping and improving electrolyte wetting in C/S composite electrodes for Li–S batteries. This was achieved through a highly flexible synthetic method which grafts organic molecules onto the surface of conductive carbon host materials, allowing for variability in both desired functionality and degree of functionalization. In this study, we showed that thiol surfaces could interact with solvated active materials in multiple ways, including covalent interactions and electrostatic lithium bonding. Additionally, the polar, nucleophilic surface introduced by the thiol modifiers allowed for better wetting of the electrode surface by the electrolyte due to the dipole–dipole interaction of the thiol groups with Li^+ from the electrolyte. This improved wettability allows for better sulfur utilization in high loading (4 mg cm^{-2}) cells while maintaining the tethering of solvated LiPSs to the cathode surface. The realization of multiple performance enhancements from a single functional group suggests the possibility of further rational molecular design of cathode systems based on small molecule interfaces. In the future, we will plan to explore the potential of altering the molecular structure of modifiers and investigate other carbon matrices. For example, a dithiol molecular functionalization could be considered to improve the reaction kinetics, as several dithiols have been reported to catalyze the reduction of polysulfides in chemical or biochemical systems.[160,168]

Chapter 4. CONCLUSION AND FUTURE PERSPECTIVES

This chapter first summarizes the fundamental study and the improvement of Zn/MnO_2 and Li/S batteries covered by this thesis. Future perspectives on how to further enhance their performance based on the study are also provided.

4.1 CONCLUSION

Nowadays, it is acknowledged that the practical applications of batteries in the storage and energy fields are primarily hindered by the relatively high cost of batteries. Thus, it is necessary to consider low-cost "next generation" beyond LIBs.

Rechargeable Zn/MnO_2 batteries are very promising for large-scale grid energy storage applications owing to their low cost, environmentally benign constitutes, and excellent safety. The major limitation, however, is the poor cycle stability. In chapter 2, based on our coupled theoretical and experimental study (*e.g.,* DFT, XRD, sXAS, SEM, etc.), we unraveled the co-intercalation (~ 1.40 V) and conversion (~ 1.26 V) reactions of Zn^{2+}/H^+ in the Zn/MnO_2 upon cycling. The rapid capacity fading of the system is unequivocally ascribed to the irreversible conversion reactions. These irreversible reactions are also characterized as kinetic-limiting reactions. Therefore, by cycling cells at higher rates, we successfully limited the irreversible reactions and significantly improve the cycling performance of Zn/MnO_2 cells that can deliver high energy and power densities (for cathode only) of ~ 231 Wh kg^{-1} and ~ 4 kW kg^{-1} at 9C, respectively.

In addition to the stationary grid, battery technologies are also of importance for long-range EVs. Li/S batteries hold great promise as the next-generation energy batteries due to their high theoretical specific capacity, low environmental impact, and low cost. In chapter 3, we successfully grafted a thiol-based, multifunctional, redox-active interface on the surface of mesoporous carbon MJ430. After modification, the capacity retention of the cells has been increased to 87% from 56%. Furthermore, we utilized NMR, XPS, and EIS to monitor the surface interactions of the thiol groups with active materials. According to the results, the thiol surfaces could covalently (S-S) and electrostatically (Li^+S^-) interact with the active materials. Meanwhile, the nucleophilic surface allowed for better wetting of the electrode due to the dipole-dipole interactions of the thiol groups with Li^+ in the electrolyte.

4.2 FUTURE PERSPECTIVES

4.2.1 *δ-MnO_2 with Intercalated Alkaline Cations for Zn/MnO_2 Batteries*

In chapter 2 we clarified the concurrence of Zn^{2+} and H^+ intercalations and conversions corresponding to the two discharge plateaus at ~ 1.40 and 1.26 V, respectively. The rapid capacity fading is clearly ascribed to the irreversible, kinetic-limiting H^+/Zn^{2+} conversions at 1.26 V that cause significant disruption of the original electrode architecture and blocking of the ion and electron transports. In addition to the rate-controlling, it is also very valuable to investigate other feasibilities to limit the subsequent conversion reactions. One of the attractive methods is to incorporate heteroatoms (*e.g.,* alkali metals,[206] as shown in Figure 4.1) between the two manganese oxide sheets of δ-MnO_2 to control the interlayer spacing and change the bonding structures between the adjacent layers, which hopefully could reinforce the layered structure of δ-MnO_2 and thus mitigate the irreversible conversions.

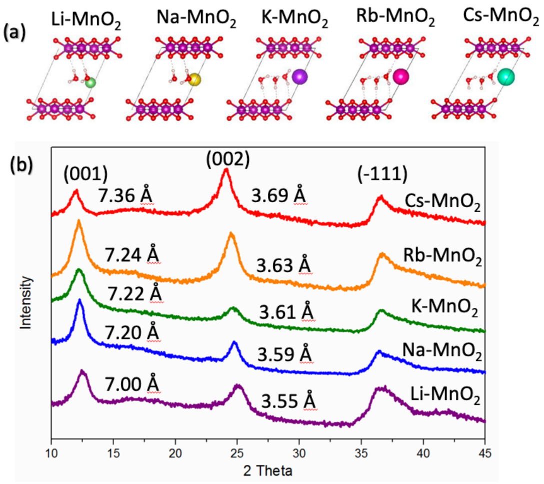

Figure 4.1. (a) Unit cell of the alkali-intercalated δ-MnO$_2$[206] and (b) their XRD patterns.

4.2.2 *Multifunctional Polyelectrolyte Gels for Li/S Batteries*

Chapter 3 provided an idea with the utility of a thiol-based, multifunctional interface for LiPS-trapping and improving electrolyte wetting in the C/S composite cathode. In addition to the cathode modification, we also expect to incorporate self-healing and LiPS-trapping polyelectrolyte gels that contain room temperature ionic liquid (RTIL) to further improve the capacity retention and significantly enhance both gravimetric and volumetric energy densities. An example of quasi-solid-state gel-Li/S cell design is shown in Figure 4.2a. The design would continue with the SH-modified MJ430/S cathode composites. The solid fraction of the gel will consist of three components: (1) a partially-crosslinked ionomer bearing oligo(ethylene oxide) units and charged pyrrolidinium units on a polymethacrylate backbone, with TFSI counterion, (2) a linear polymethacrylate with naphthalene diimide (NDI) pendant groups, and (3) a multi-branched crosslinker with pyrene (Py) headgroups to bind with the linear chain through π-π stacking interactions. The liquid component of the gel will be a room temperature LiTFSI-dissolved ionic liquid based on a cation (*e.g.,* *N*-methyl-*N*-butylpyrrolidinium (Pyr$_{14}$)) coupled with TFSI. Those components are expected to increase the mechanical strength, conduct reversible self-healing for mitigate electrode cracking, and further trap LiPSs.

In the preliminary experiment, we successfully synthesized a particular gel electrolyte consisting of solvate ionogel (SIG)/ solvate ionic liquid (SIL) (PEDGMA M_n ~750 + Li(tetraglyme)TFSI + anisole) as the prototype. Figure 4.2b and c display the electrochemical performance of the quasi-solid-sate cells solely containing the SIG/SIL electrolytes (without the addition of self-healing and thiol-modified components). The results show a better capacity retention but a larger overpotential compared to the conventional Li/S cells, which needs to be further investigated and optimized.

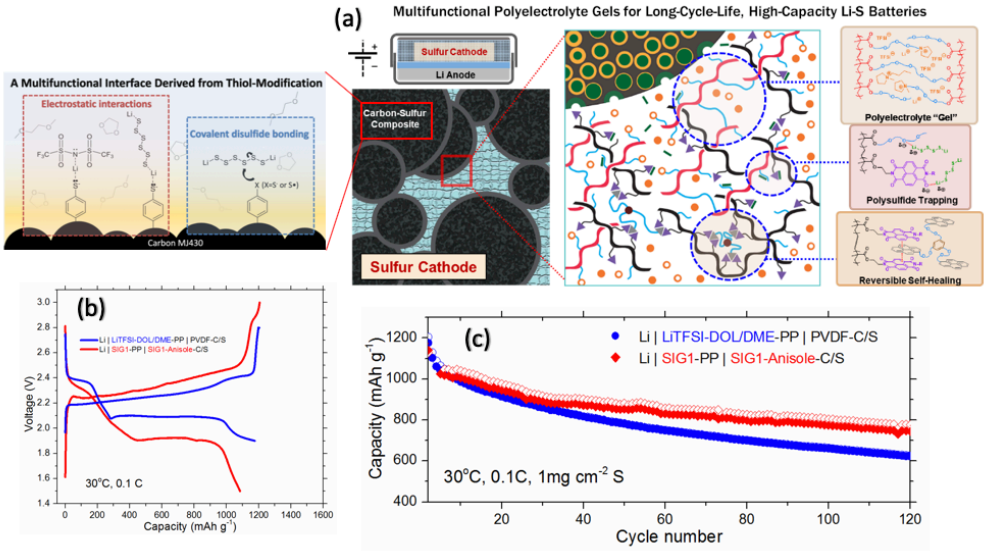

Figure 4.2. (a) Schematic overview of the Li/S cell design using both modified cathode and self-healing, interpenetrating gel. (b-c) Comparison of the electrochemical performance of the conventional Li/S cells containing organic LiTFSI-DOL/DME electrolytes (blue) and the quasi-solid-state cells containing particular SIG/SIL electrolytes (red).

BIBLIOGRAPHY

1. Goodenough, J. B. & Kim, Y. Challenges for Rechargeable Li Batteries. *Chem. Mater.* **22**, 587–603 (2010).
2. Lu, L., Yang, H. & Burnett, J. Investigation on wind power potential on Hong Kong islands - An analysis of wind power and wind turbine characteristics. *Renew. Energy* **27**, 1–12 (2002).
3. Nazeeruddin, M. K., Baranoff, E. & Grätzel, M. Dye-sensitized solar cells: A brief overview. *Sol. Energy* (2011). doi:10.1016/j.solener.2011.01.018
4. Goodenough, J. B. & Park, K.-S. The Li-ion rechargeable battery: a perspective. *J. Am. Chem. Soc.* **135**, 1167–76 (2013).
5. Newman, J. & Thomas-Alyea, K. E. *Electrochemical systems*. (John Wiley & Sons, Inc., 2012).
6. Team, M. E. V. A guide to understanding battery specifications. (2008). Available at: http://web.mit.edu/evt/summary_battery_specifications.pdf.
7. Yang, Z. G. *et al.* Electrochemical energy storage for green grid. *Chem. Rev.* **111**, 3577–3613 (2011).
8. Dunn, B., Kamath, H. & Tarascon, J.-M. M. Electrical energy storage for the grid: A battery of choices. *Science (80-.).* **334**, 928–935 (2011).
9. Doughty, D. H., Butler, P. C., Akhil, A. a, Clark, N. H. & Boyes, J. D. Batteries for Large-Scale Stationary Electrical Energy Storage. *Electrochem. Soc. Interface* **19**, 49–53 (2010).
10. Larcher, D. & Tarascon, J. M. Towards greener and more sustainable batteries for electrical energy storage. *Nature Chemistry* **7**, 19–29 (2015).
11. Version, D., Based, E. & Modeling, S. Wind Turbine and Electrochemical Based Storage Modeling and Integrated Control Strategies to Improve Renewable Energy Integration in the Grid. (2011).
12. EPRI. *VRB Energy Storage for Voltage Stabilization: Testing and Evaluation of the PacifiCorp Vanadium Redox Battery Energy Storage System at Castle Valley, Utah*. (2005).
13. EPRI-DOE. *Handbook Supplement of Energy Storage for Grid Connected Wind Generation Applications*. (2004).
14. Armand, M. Issues and challenges facing rechargeable lithium batteries. **414**, 359–367 (2001).
15. Placke, T., Kloepsch, R., Dühnen, S. & Winter, M. Lithium ion, lithium metal, and alternative rechargeable battery technologies: the odyssey for high energy density. *J. Solid State Electrochem.* **21**, 1939–1964 (2017).
16. Saxena, S., MacDonald, J. & Moura, S. Charging ahead on the transition to electric vehicles with standard 120 V wall outlets. *Appl. Energy* **157**, 720–728 (2015).
17. Schmidt, O., Hawkes, A., Gambhir, A. & Staaell, I. The future cost of electrical energy storage based on experience rates. **2**, 17110 (2017).
18. Nykvist, B. & Nilsson, M. Rapidly falling costs of battery packs for electric vehicles. (2015). doi:10.1038/NCLIMATE2564
19. Pavlov, D. *Lead-acid batteries: science and technology*. (Elsevier, 2011).
20. Putois, F. Market for nickel-cadmium batteries. *J. Power Sources* **57**, 67–70 (1995).
21. Zhan, F. *et al.* Characteristics of Ni/MH power batteries and its application to electric vehicles. *J. Alloys Compd.* **293**–**295**, 804–808 (1999).

22. Andre, D. *et al.* Characterization of high-power lithium-ion batteries by electrochemical impedance spectroscopy. I. Experimental investigation. *J. Power Sources* **196**, 5334–5341 (2011).
23. Patry, G., Romagny, A., Martinet, S. & Froelich, D. Cost modeling of lithium-ion battery cells for automotive applications. *Energy Sci. Eng.* **3**, 71–82 (2015).
24. Andre, D. *et al.* Future generations of cathode materials: an automotive industry perspective. *J. Mater. Chem. A* **3**, 6709–6732 (2015).
25. Blomgren, G. E. The Development and Future of Lithium Ion Batteries. *J. Electrochem. Soc.* **164**, A5019–A5025 (2017).
26. Schmuch, R., Wagner, R., Hörpel, G., Placke, T. & Winter, M. Performance and cost of materials for lithium-based rechargeable automotive batteries. *Nat. Energy* **3**, 267–278 (2018).
27. Voelcker, J. Electric-car battery costs: Tesla $190 per kwh for pack, GM $145 for cells. (2016). Available at: https://www.greencarreports.com/news/1103667_electric-car-battery-costs-tesla-190-per-kwh-for-pack-gm-145-for-cells.
28. About Electri Vehicles. Available at: https://www.greencarreports.com/news/1103667_electric-car-battery-costs-tesla-190-per-kwh-for-pack-gm-145-for-cells.
29. Van Noorden, R. The rechargeable revolution: A better battery. *Nature* (2014). doi:10.1038/507026a
30. Armand, M. & Tarascon, J. Building better batteries. **451**, 2–7 (2008).
31. Wanger, T. C. The Lithium future-resources, recycling, and the environment. *Conserv. Lett.* (2011). doi:10.1111/j.1755-263X.2011.00166.x
32. Roth, E. P. & Orendorff, C. J. How Electrolytes Influence Battery Safety. *Interface Mag.* (2016). doi:10.1149/2.f04122if
33. White, C. D. & Zhang, K. M. Using vehicle-to-grid technology for frequency regulation and peak-load reduction. *J. Power Sources* (2011). doi:10.1016/j.jpowsour.2010.11.010
34. Ingale, N. D., Gallaway, J. W., Nyce, M., Couzis, A. & Banerjee, S. Rechargeability and economic aspects of alkaline zinc-manganese dioxide cells for electrical storage and load leveling. *J. Power Sources* **276**, 7–18 (2015).
35. Chen, H. *et al.* Progress in electrical energy storage system: A critical review. *Prog. Nat. Sci.* **19**, 291–312 (2009).
36. Tang, W. *et al.* Aqueous rechargeable lithium batteries as an energy storage system of superfast charging. *Energy Environ. Sci.* **6**, 2093 (2013).
37. Aurbach, D. *et al.* Prototype systems for rechargeable magnesium batteries. *Nature* **407**, 724–727 (2000).
38. Liu, Y., Ai, K. & Lu, L. Quest for nonaqueous multivalent secondary batteries: Magnesium and beyond. *Chem. Rev.* **114**, 11683–11720 (2014).
39. Li, Z., Xiang, K., Xing, W., Carter, W. C. & Chiang, Y. M. Reversible aluminum-ion intercalation in prussian blue analogs and demonstration of a high-power aluminum-ion asymmetric capacitor. *Adv. Energy Mater.* **5**, 1401410 (2015).
40. Xu, C. *et al.* Secondary batteries with multivalent ions for energy storage. *Sci. Rep.* **5**, 14120 (2015).
41. Lin, M.-C. *et al.* An ultrafast rechargeable aluminium-ion battery. *Nature* **520**, 325–8 (2015).
42. Zhang, N. *et al.* Rechargeable aqueous zinc-manganese dioxide batteries with high energy

and power densities. *Nat. Commun.* **8**, 405 (2017).

43. Pan, H. *et al.* Reversible aqueous zinc/manganese oxide energy storage from conversion reactions. *Nat. Energy* **1**, 16039 (2016).
44. Xu, C., Li, B., Du, H. & Kang, F. Energetic zinc ion chemistry: The rechargeable zinc ion battery. *Angew. Chemie - Int. Ed.* **51**, 933–935 (2012).
45. Lee, B. *et al.* Electrochemically-induced reversible transition from the tunneled to layered polymorphs of manganese dioxide. *Sci. Rep.* **4**, 6066 (2014).
46. Alfaruqi, M. H. *et al.* Electrochemically Induced Structural Transformation in a γ-MnO $_2$ Cathode of a High Capacity Zinc-Ion Battery System. *Chem. Mater.* **27**, 3609–3620 (2015).
47. Shoji, T. & Yamamoto, T. Charging and discharging behavior of zinc-manganese galvanic cells using zinc sulfate as electrolyte. *J. Electroanal. Chem.* **362**, 153–157 (1993).
48. Chabre, Y. & Pannetier, J. Structural and electrochemical properties of the proton / γ-MnO2system. *Prog. Solid State Chem.* **23**, 1–130 (1995).
49. Kitchaev, D. A., Dacek, S. T., Sun, W. & Ceder, G. Thermodynamics of Phase Selection in MnO 2 Framework Structures through Alkali Intercalation and Hydration. *J. Am. Chem. Soc.* **139**, 2672–2681 (2017).
50. Lei, G. Crystal structures and metal uptake capacity of 10Å- manganates: An overview. *Mar. Geol.* **133**, 103–112 (1996).
51. Arthur, T. S. *et al.* Understanding the electrochemical mechanism of K-αMnO2for magnesium battery cathodes. *ACS Appl. Mater. Interfaces* **6**, 7004–7008 (2014).
52. IEA. Energy Technology Perspectives 2017. (2017). Available at: http://www.iea.org/etp2017/.
53. EV-Volumes. Global Plug-in Sales for 2016. (2017). Available at: http://www.ev-volumes.com/news/global-plug-in-sales-for-2016/.
54. Cano, Z. P. *et al.* Batteries and fuel cells for emerging electric vehicle markets. *Nat. Energy* **3**, 279–289 (2018).
55. Hagen, M. *et al.* Lithium-Sulfur Cells: The Gap between the State-of-the-Art and the Requirements for High Energy Battery Cells. *Adv. Energy Mater.* **5**, 1401986 (2015).
56. Scheers, J., Fantini, S. & Johansson, P. A review of electrolytes for lithium–sulphur batteries. *J. Power Sources* **255**, 204–218 (2014).
57. Zhang, S. S. Role of LiNO3 in rechargeable lithium/sulfur battery. *Electrochim. Acta* **70**, 344–348 (2012).
58. Ji, X., Lee, K. T. & Nazar, L. F. A highly ordered nanostructured carbon-sulphur cathode for lithium-sulphur batteries. *Nat. Mater.* **8**, 500–506 (2009).
59. Zhou, W. *et al.* Amylopectin wrapped graphene oxide/sulfur for improved cyclability of Lithium-Sulfur battery. *ACS Nano* **7**, 8801–8808 (2013).
60. Chen, H. *et al.* Ultrafine Sulfur Nanoparticles in Conducting Polymer Shell as Cathode Materials for High Performance Lithium/Sulfur Batteries. *Sci. Rep.* **3**, 1910 (2013).
61. Hoefling, A. *et al.* Mechanism for the stable performance of sulfur-copolymer cathode in lithium–sulfur battery studied by solid-state NMR spectroscopy. *Chem. Mater.* **30**, 2915–2923 (2018).
62. Li, Y. *et al.* densed. *Chem. Mater.* **31**, 2036–2047 (2019).
63. Lam, L. T., Haigh, N. P., Phyland, C. G. & Urban, A. J. Failure mode of valve-regulated lead-acid batteries under high-rate partial-state-of-charge operation. *J. Power Sources* **133**, 126–134 (2004).

64. Carter, R. *et al.* A Sugar-Derived Room-Temperature Sodium Sulfur Battery with Long Term Cycling Stability. *Nano Lett.* **17**, 1863–1869 (2017).
65. Perry, M. L. & Weber, A. Z. Advanced Redox-Flow Batteries: A Perspective. *J. Electrochem. Soc.* **163**, A5064–A5067 (2016).
66. Lu, Y., Goodenough, J. B. & Kim, Y. Aqueous cathode for next-generation alkali-ion batteries. *J. Am. Chem. Soc.* **133**, 5756–5759 (2011).
67. Pasta, M., Wessells, C. D., Huggins, R. A. & Cui, Y. A high-rate and long cycle life aqueous electrolyte battery for grid-scale energy storage. *Nat. Commun.* **3**, 1149 (2012).
68. Guduru, R., Icaza, J., Guduru, R. K. & Icaza, J. C. A Brief Review on Multivalent Intercalation Batteries with Aqueous Electrolytes. *Nanomaterials* **6**, 41 (2016).
69. Rong, Z. *et al.* Materials Design Rules for Multivalent Ion Mobility in Intercalation Structures. *Chem. Mater.* **27**, 6016–6021 (2015).
70. Kordesch, K., Gsellmann, J. & Tomantschger, K. The alkaline manganese dioxide-zinc cell. *J. Electroanal. Chem.* **118**, 187–201 (1981).
71. Qu, D., Diehl, D., Conway, B. E. E., Pell, W. G. G. & Qian, S. Y. Y. Development of high-capacity primary alkaline manganese dioxide/zinc cells consisting of Bi-doping of MnO2. *J. Appl. Electrochem.* **35**, 1111–1120 (2005).
72. Gallaway, J. W. *et al.* Hetaerolite Profiles in Alkaline Batteries Measured by High Energy EDXRD. *J. Electrochem. Soc.* **162**, A162–A168 (2014).
73. Yamamoto, T. & Shoji, T. Rechargeable ZnlZnSO4IMnO2-type Cells. **7**, 27–28 (1986).
74. Alfaruqi, M. H. *et al.* A layered δ-MnO2 nanoflake cathode with high zinc-storage capacities for eco-friendly battery applications. *Electrochem. commun.* **60**, 121–125 (2015).
75. Lee, J., Ju, J. B., Cho, W. Il, Cho, B. W. & Oh, S. H. Todorokite-type MnO2as a zinc-ion intercalating material. *Electrochim. Acta* **112**, 138–143 (2013).
76. Kim, S. H. & Oh, S. M. Degradation mechanism of layered MnO2cathodes in Zn/ZnSO4/MnO2rechargeable cells. *J. Power Sources* **72**, 150–158 (1998).
77. Sun, W. *et al.* Zn/MnO 2 Battery Chemistry With H + and Zn 2+ Coinsertion. *J. Am. Chem. Soc.* **139**, 9775–9778 (2017).
78. Zhao, S. *et al.* Unravelling the reaction chemistry and degradation mechanism in aqueous Zn/MnO2 rechargeable batteries. *J. Mater. Chem. A* **6**, 5733–5739 (2018).
79. Wei, W., Cui, X., Chen, W. & Ivey, D. G. Manganese oxide-based materials as electrochemical supercapacitor electrodes. *Chem. Soc. Rev.* **40**, 1697–1721 (2011).
80. Bergmann, A., Zaharieva, I., Dau, H. & Strasser, P. Electrochemical water splitting by layered and 3D cross-linked manganese oxides: correlating structural motifs and catalytic activity. *Energy Environ. Sci.* **6**, 2745 (2013).
81. Huynh, M., Shi, C., Billinge, S. J. L. & Nocera, D. G. Nature of Activated Manganese Oxide for Oxygen Evolution. *J. Am. Chem. Soc.* **137**, 14887–14904 (2015).
82. Suib, S. L. Porous manganese oxide octahedral molecular sieves and octahedral layered materials. *Accounts of Chemical Research* **41**, 479–487 (2008).
83. Qiao, R. *et al.* High-efficiency in situ resonant inelastic x-ray scattering (iRIXS) endstation at the Advanced Light Source. *Rev. Sci. Instrum.* **88**, 033106 (2017).
84. Perdew, J. P., Burke, K. & Ernzerhof, M. Generalized gradient approximation made simple. *Phys. Rev. Lett.* **77**, 3865–3868 (1996).
85. Blöchl, P. E. Projector augmented-wave method. *Phys. Rev. B* **50**, 17953–17979 (1994).
86. Joubert, D. From ultrasoft pseudopotentials to the projector augmented-wave method.

Phys. Rev. B - Condens. Matter Mater. Phys. **59**, 1758–1775 (1999).

87. Kresse, G. & Hafner, J. Ab initio molecular dynamics for liquid metals. *Phys. Rev. B* **47**, 558–561 (1993).
88. Kresse, G. & Furthmüller, J. Efficient iterative schemes for ab initio total-energy calculations using a plane-wave basis set. *Phys. Rev. B - Condens. Matter Mater. Phys.* **54**, 11169–11186 (1996).
89. Zaanen, J. *et al.* What can be learned about high Tc from local density theory? *Phys. C Supercond. its Appl.* **153–55**, 1636–1641 (1988).
90. Anisimov, V. I., Zaanen, J. & Andersen, O. K. Band theory and Mott insulators: Hubbard U instead of Stoner I. *Phys. Rev. B* **44**, 943–954 (1991).
91. Mueller, T., Hautier, G., Jain, A. & Ceder, G. Evaluation of tavorite-structured cathode materials for lithium-ion batteries using high-throughput computing. *Chem. Mater.* **23**, 3854–3862 (2011).
92. Monkhorst, H. & Pack, J. Special points for Brillouin zone integrations. *Phys. Rev. B* **13**, 5188–5192 (1976).
93. Zhou, Y. K., Toupin, M., Bélanger, D., Brousse, T. & Favier, F. Electrochemical preparation and characterization of Birnessite-type layered manganese oxide films. *J. Phys. Chem. Solids* **67**, 1351–1354 (2006).
94. Qu, D. Investigation of the porosity of electrolytic manganese dioxide and its performance as alkaline cathode material. *J. Power Sources* **156**, 692–699 (2006).
95. Thapa, A. K. *et al.* Synthesis of mesoporous birnessite-MnO2 composite as a cathode electrode for lithium battery. *Electrochim. Acta* **116**, 188–193 (2014).
96. Lee, B. *et al.* Elucidating the intercalation mechanism of zinc ions into α-MnO $_2$ for rechargeable zinc batteries. *Chem. Commun.* **51**, 9265–9268 (2015).
97. Lanson, B., Drits, V. A., Silvester, E. & Manceau, A. Structure of H-exchanged hexagonal birnessite and its mechanism of formation from Na-rich monoclinic buserite at low pH. *Am. Mineral.* **85**, 826–838 (2000).
98. Ruetschi, P. & Giovanoli, R. Cation Vacancies in MnO2 and Their Influence on Electrochemical Reactivity. *J. Electrochem. Soc.* **135**, 2663–2669 (1988).
99. Hertzberg, B. J. *et al.* Effect of Multiple Cation Electrolyte Mixtures on Rechargeable Zn-MnO2Alkaline Battery. *Chem. Mater.* **28**, 4536–4545 (2016).
100. Alfaruqi, M. H. *et al.* Enhanced reversible divalent zinc storage in a structurally stable α-MnO2nanorod electrode. *J. Power Sources* **288**, 320–327 (2015).
101. Lin, F. *et al.* Synchrotron X-ray Analytical Techniques for Studying Materials Electrochemistry in Rechargeable Batteries. *Chem. Rev.* **117**, 13123–13186 (2017).
102. Li, Q. *et al.* Quantitative probe of the transition metal redox in battery electrodes through soft x-ray absorption spectroscopy. *J. Phys. D. Appl. Phys.* **49**, 413003 (2016).
103. Qiao, R., Chin, T., Harris, S. J., Yan, S. & Yang, W. Spectroscopic fingerprints of valence and spin states in manganese oxides and fluorides. *Curr. Appl. Phys.* **13**, 544–548 (2013).
104. Qiao, R. *et al.* Revealing and suppressing surface Mn(II) formation of Na0.44MnO2 electrodes for Na-ion batteries. *Nano Energy* **16**, 186–195 (2015).
105. Ling, C., Zhang, R., Arthur, T. S. & Mizuno, F. How General is the Conversion Reaction in Mg Battery Cathode: A Case Study of the Magnesiation of a-MnO2. *Chem. Mater.* **27**, 5799–5807 (2015).
106. Allen J. Bard; Larry R. Faulkner; Johna Leddy; Cynthia G. Zoski. *Electrochemical Methods : Fundamentals and Applications*. *Wiley New York* **2**, (Wiley, 1980).

107. Li, X. *et al.* Atomic layer deposition of solid-state electrolyte coated cathode materials with superior high-voltage cycling behavior for lithium ion battery application. *Energy Environ. Sci.* **7**, 768–778 (2014).
108. Xu, C., Chiang, S. W., Ma, J. & Kang, F. Investigation on Zinc Ion Storage in Alpha Manganese Dioxide for Zinc Ion Battery by Electrochemical Impedance Spectrum. *J. Electrochem. Soc.* **160**, A93–A97 (2012).
109. Guo, X. *et al.* A Hollow-Structured Manganese Oxide Cathode for Stable Zn-MnO2 Batteries. *Nanomaterials* **8**, 301 (2018).
110. Kundu, D., Adams, B. D., Duffort, V., Vajargah, S. H. & Nazar, L. F. A high-capacity and long-life aqueous rechargeable zinc battery using a metal oxide intercalation cathode. *Nat. Energy* **1**, 16119 (2016).
111. Jiang, B. *et al.* Manganese Sesquioxide as Cathode Material for Multivalent Zinc Ion Battery with High Capacity and Long Cycle Life. *Electrochim. Acta* **229**, 422–428 (2017).
112. Jo, J. H., Sun, Y.-K. & Myung, S.-T. Hollandite-type Al-doped VO $_{1.52}$ (OH) $_{0.77}$ as a zinc ion insertion host material. *J. Mater. Chem. A* **5**, 8367–8375 (2017).
113. Li, G. *et al.* Towards polyvalent ion batteries: A zinc-ion battery based on NASICON structured Na3V2(PO4)3. *Nano Energy* **25**, 211–217 (2016).
114. Zhao, J. *et al.* High-voltage Zn/LiMn0.8Fe0.2PO4aqueous rechargeable battery by virtue of 'water-in-salt' electrolyte. *Electrochem. commun.* **69**, 6–10 (2016).
115. Zhang, L., Chen, L., Zhou, X. & Liu, Z. Towards high-voltage aqueous metal-ion batteries beyond 1.5 V: The zinc/zinc hexacyanoferrate system. *Adv. Energy Mater.* **5**, 1–5 (2015).
116. Zhang, Y. *et al.* Preparation of M1/3Ni1/3Mn2/3O2(M = Mg or Zn) and its performance as the cathode material of aqueous divalent cations battery. *Electrochim. Acta* **182**, 971–978 (2015).
117. Zhang, L. L. & Zhao, X. S. Carbon-based materials as supercapacitor electrodes. *Chem. Soc. Rev.* **38**, 2520 (2009).
118. Hannah, D. C., Sai Gautam, G., Canepa, P. & Ceder, G. On the Balance of Intercalation and Conversion Reactions in Battery Cathodes. *Adv. Energy Mater.* **8**, 1800379 (2018).
119. Li, Y. *et al.* A multi-functional interface derived from thiol-modified mesoporous carbon in lithium–sulfur batteries. *J. Mater. Chem. A* 13372–13381 (2019). doi:10.1039/c9ta02743b
120. Howell, D. Overview of Battery R & D Activities. in *briefing, Department of Energy Vehicle Technologies Program* (2012).
121. Goodenough, J. B. & Park, K. S. The Li-ion rechargeable battery: A perspective. *Journal of the American Chemical Society* **135**, 1167–1176 (2013).
122. Li, G. *et al.* Revisiting the Role of Polysulfides in Lithium-Sulfur Batteries. *Adv. Mater.* **1705590**, 1–19 (2018).
123. Manthiram, A., Fu, Y., Chung, S.-H., Zu, C. & Su, Y.-S. Rechargeable Lithium–Sulfur Batteries. *Chem. Rev.* **114**, 11751–11787 (2014).
124. Xu, R., Lu, J. & Amine, K. Progress in Mechanistic Understanding and Characterization Techniques of Li-S Batteries. *Advanced Energy Materials* **5**, 1500408 (2015).
125. Chen, J. *et al.* Restricting the Solubility of Polysulfides in Li-S Batteries Via Electrolyte Salt Selection. *Adv. Energy Mater.* **6**, 1600160 (2016).
126. Zhang, S. *et al.* Optimization of Pore Structure of Cathodic Carbon Supports for Solvate Ionic Liquid Electrolytes Based Lithium–Sulfur Batteries. *ACS Appl. Mater. Interfaces* **8**, 27803–27813 (2016).

127. Eftekhari, A. & Kim, D. W. Cathode materials for lithium-sulfur batteries: A practical perspective. *J. Mater. Chem. A* **5**, 17734–17776 (2017).
128. Pang, Q., Liang, X., Kwok, C. Y. & Nazar, L. F. Advances in lithium-sulfur batteries based on multifunctional cathodes and electrolytes. *Nature Energy* **1**, 16132 (2016).
129. Li, X. *et al.* Optimization of mesoporous carbon structures for lithium–sulfur battery applications. *J. Mater. Chem.* **21**, 16603 (2011).
130. Lin, C. *et al.* A facile synthesis of three dimensional graphene sponge composited with sulfur nanoparticles for flexible Li–S cathodes. *Phys. Chem. Chem. Phys.* **18**, 22146–22153 (2016).
131. Li, Y. & Chen, F. Li–S batteries: Firing for compactness. *Nat. Energy* **2**, 17096 (2017).
132. Yang, C.-P., Yin, Y.-X., Guo, Y.-G. & Wan, L.-J. Electrochemical (De)Lithiation of 1D Sulfur Chains in Li−S Batteries: A Model System Study. *J. Am. Chem. Soc* **137**, (2015).
133. Li, Z., Wu, H. Bin & Lou, X. W. Rational designs and engineering of hollow micro-/nanostructures as sulfur hosts for advanced lithium-sulfur batteries. *Energy and Environmental Science* **9**, 3061–3070 (2016).
134. Evers, S. & Nazar, L. F. Graphene-enveloped sulfur in a one pot reaction: a cathode with good coulombic efficiency and high practical sulfur content. *Chem. Commun.* **48**, 1233–1235 (2012).
135. Fujimori, T. *et al.* Conducting linear chains of sulphur inside carbon nanotubes. *Nat. Commun.* **4**, 2162 (2013).
136. Yuan, Z. *et al.* Hierarchical free-standing carbon-nanotube paper electrodes with ultrahigh sulfur-loading for lithium-sulfur batteries. *Adv. Funct. Mater.* **24**, 6105–6112 (2014).
137. Li, H. *et al.* Dense Graphene Monolith for High Volumetric Energy Density Li-S Batteries. *Adv. Energy Mater.* **8**, 1703438 (2018).
138. Hernández-Rentero, C. *et al.* Low-cost disordered carbons for Li/S batteries: A high-performance carbon with dual porosity derived from cherry pits. *Nano Res.* **11**, 89–100 (2018).
139. Li, Z., Zhang, J. & Lou, X. W. Hollow Carbon Nanofibers Filled with MnO 2 Nanosheets as Efficient Sulfur Hosts for Lithium-Sulfur Batteries. *Angew. Chemie - Int. Ed.* **54**, 12886–12890 (2015).
140. Chung, S. H. & Manthiram, A. Eggshell membrane-derived polysulfide absorbents for highly stable and reversible lithium-sulfur cells. *ACS Sustain. Chem. Eng.* **2**, 2248–2252 (2014).
141. Lochala, J., Liu, D., Wu, B., Robinson, C. & Xiao, J. Research Progress toward the Practical Applications of Lithium–Sulfur Batteries. *ACS Appl. Mater. Interfaces* **9**, 24407–24421 (2017).
142. Lv, D. *et al.* High Energy Density Lithium-Sulfur Batteries: Challenges of Thick Sulfur Cathodes. *Adv. Energy Mater.* **5**, 1402290 (2015).
143. Zhang, J. *et al.* A Conductive Molecular Framework Derived Li2S/N,P-Codoped Carbon Cathode for Advanced Lithium–Sulfur Batteries. *Adv. Energy Mater.* **7**, 1602876 (2017).
144. Zhou, J. *et al.* The impact of the particle size of a metal-organic framework for sulfur storage in Li-S batteries. *J. Mater. Chem. A* **3**, 8272–8275 (2015).
145. Xiao, Z., Yang, Z., Zhang, L., Pan, H. & Wang, R. Sandwich-Type NbS $_2$ @S@I-Doped Graphene for High-Sulfur-Loaded, Ultrahigh-Rate, and Long-Life Lithium–Sulfur Batteries. *ACS Nano* **11**, 8488–8498 (2017).
146. Zhou, G., Paek, E., Hwang, G. S. & Manthiram, A. Long-life Li/polysulphide batteries

with high sulphur loading enabled by lightweight three-dimensional nitrogen/sulphur-codoped graphene sponge. *Nat. Commun.* **6**, 7760 (2015).

147. Yang, Y. *et al.* Improving the performance of lithium-sulfur batteries by conductive polymer coating. *ACS Nano* **5**, 9187–9193 (2011).
148. Xia, W., Mahmood, A., Zou, R. & Xu, Q. Metal–organic frameworks and their derived nanostructures for electrochemical energy storage and conversion. *Energy Environ. Sci.* **8**, 1837–1866 (2015).
149. Zheng, J. *et al.* Lewis Acid−Base Interactions between Polysulfides and Metal Organic Framework in Lithium Sulfur Batteries. *Nano Lett* **14**, (2014).
150. Liu, X., Huang, J.-Q., Zhang, Q. & Mai, L. Nanostructured Metal Oxides and Sulfides for Lithium-Sulfur Batteries. *Adv. Mater.* **29**, 1601759 (2017).
151. Pei, F. *et al.* A Two-Dimensional Porous Carbon-Modified Separator for High-Energy-Density Li-S Batteries. *Joule* **2**, 323–336 (2018).
152. Tang, W. *et al.* In Situ Observation and Electrochemical Study of Encapsulated Sulfur Nanoparticles by MoS2Flakes. *J. Am. Chem. Soc.* **139**, 10133–10141 (2017).
153. Seh, Z. W., Sun, Y., Zhang, Q. & Cui, Y. Designing high-energy lithium-sulfur batteries. *Chemical Society Reviews* **45**, 5605–5634 (2016).
154. Pang, Q., Liang, X., Kwok, C. Y. & Nazar, L. F. Review—The Importance of Chemical Interactions between Sulfur Host Materials and Lithium Polysulfides for Advanced Lithium-Sulfur Batteries. *J. Electrochem. Soc.* **162**, A2567–A2576 (2015).
155. Kim, J. H. *et al.* Stabilization of Insoluble Discharge Products by Facile Aniline Modification for High Performance Li-S Batteries. *Adv. Energy Mater.* **5**, 1500268 (2015).
156. Song, M. K., Zhang, Y. & Cairns, E. J. A long-life, high-rate lithium/sulfur cell: A multifaceted approach to enhancing cell performance. *Nano Lett.* **13**, 5891–5899 (2013).
157. Sun, Z. *et al.* Conductive porous vanadium nitride/graphene composite as chemical anchor of polysulfides for lithium-sulfur batteries. *Nat. Commun.* **8**, 14627 (2017).
158. Shaibani, M. *et al.* Suppressed Polysulfide Crossover in Li-S Batteries through a High-Flux Graphene Oxide Membrane Supported on a Sulfur Cathode. *ACS Nano* **10**, 7768–7779 (2016).
159. Mao, J., Wang, Y., Zhu, J., Yu, J. & Hu, Z. Thiol functionalized carbon nanotubes: synthesis by sulfur chemistry and their multi-purpose applications. *Appl. Surf. Sci.* **447**, 235–243 (2018).
160. Hua, W. *et al.* Polysulfide-Scission Reagents for the Suppression of the Shuttle Effect in Lithium-Sulfur Batteries. *ACS Nano* **11**, 2209–2218 (2017).
161. Ponraj, R. *et al.* Effective Trapping of Lithium Polysulfides Using a Functionalized Carbon Nanotube-Coated Separator for Lithium-Sulfur Cells with Enhanced Cycling Stability. *ACS Appl. Mater. Interfaces* **9**, 38445–38454 (2017).
162. Ma, L. *et al.* Enhanced Li-S batteries using amine-functionalized carbon nanotubes in the cathode. *ACS Nano* **10**, 1050–1059 (2016).
163. Zhou, G. *et al.* Fibrous Hybrid of Graphene and Sulfur Nanocrystals for High-Performance Lithium–Sulfur Batteries. *ACS Nano* **7**, 5367–5375 (2013).
164. Kreuer, K. -D, Rabenau, A. & Weppner, W. Vehicle Mechanism, A New Model for the Interpretation of the Conductivity of Fast Proton Conductors. *Angew. Chemie Int. Ed. English* **21**, 208–209 (1982).
165. Liu, M., Visco, S. J. & Jonghe, L. C. D. L. C. D. L. C. De. No Title. *J. Electrochem. Soc.*

136, 2570–2575 (1989).

166. Joseph, A. & George, B. THE CURRENT STATUS OF SULPHUR VULCANIZATION AND DEVULCANIZATION CHEMISTRY: DEVULCANIZATION. *Rubber Sci.* **29(1)**, 62–100 (2016).
167. Borsari, M., Cannio, M. & Gavioli, G. Electrochemical Behavior of Diphenyl Disulfide and Thiophenol on Glassy Carbon and Gold Electrodes in Aprotic Media. *Electroanalysis* **15**, 1192–1197 (2003).
168. Lamoureux, G. V. & Whitesides, G. M. Synthesis of Dithiols as Reducing Agents for Disulfides in Neutral Aqueous Solution and Comparison of Reduction Potentials. *J. Org. Chem.* **58**, 633–641 (1993).
169. Xu, N. *et al.* Greatly Suppressed Shuttle Effect for Improved Lithium Sulfur Battery Performance through Short Chain Intermediates. *Nano Lett.* **17**, 538–543 (2017).
170. Kim, H., Lee, J., Ahn, H., Kim, O. & Park, M. J. Synthesis of three-dimensionally interconnected sulfur-rich polymers for cathode materials of high-rate lithium-sulfur batteries. *Nat. Commun.* **6**, 7278 (2015).
171. Choudhury, S. *et al.* Carbon onion/sulfur hybrid cathodes via inverse vulcanization for lithium–sulfur batteries. *Sustain. Energy Fuels* **2**, 133–146 (2018).
172. Toupin, M. & Bélanger, D. Spontaneous functionalization of carbon black by reaction with 4-nitrophenyldiazonium cations. *Langmuir* **24**, 1910–1917 (2008).
173. Latimer, A. M., Silander, J. A., Gelfand, A. E., Rebelo, A. G. & Richardson, D. M. *South African journal of science. South African Journal of Science* **106**, (Academy of Science of South Africa, 2010).
174. Castner, D. G., Hinds, K. & Grainger, D. W. X-ray Photoelectron Spectroscopy Sulfur 2p Study of Organic Thiol and Disulfide Binding Interactions with Gold Surfaces. *Langmuir* **12**, 5083–5086 (2002).
175. Li, G. *et al.* Three-dimensional porous carbon composites containing high sulfur nanoparticle content for high-performance lithium-sulfur batteries. *Nat. Commun.* **7**, 10601 (2016).
176. Kwon, S. J., Kim, C. W., Jeong, W. T. & Lee, K. S. Synthesis and electrochemical properties of olivine LiFePO4 as a cathode material prepared by mechanical alloying. *J. Power Sources* **137**, 93–99 (2004).
177. Dance, I. G., Fisher, K. J., Banda, R. M. H. & Scudder, M. L. Layered Structure of Crystalline Compounds AgSR. *Inorg. Chem.* **30**, 183–187 (1991).
178. Viel, P. *et al.* Covalent grafting onto self-adhesive surfaces based on aryldiazonium salt seed layers. *J. Mater. Chem.* **18**, 5913–5920 (2008).
179. Park, J. W. *et al.* Solvent effect of room temperature ionic liquids on electrochemical reactions in lithium-sulfur batteries. *J. Phys. Chem. C* **117**, 4431–4440 (2013).
180. Mikhaylik, Y. V. & Akridge, J. R. Polysulfide Shuttle Study in the Li/S Battery System. *J. Electrochem. Soc.* **151**, A1969 (2004).
181. Kim, S. H., Yeon, J. S., Kim, R., Choi, K. M. & Park, H. S. A functional separator coated with sulfonated metal-organic framework/Nafion hybrids for Li-S batteries. *J. Mater. Chem. A* **6**, 24971–24978 (2018).
182. Hu, X. *et al.* Nitrogen-rich hierarchically porous carbon as a high-rate anode material with ultra-stable cyclability and high capacity for capacitive sodium-ion batteries. *Nano Energy* **56**, 828–839 (2019).
183. Li, X. *et al.* A Simple One-Pot Strategy for Synthesizing Ultrafine SnS $_2$

Nanoparticle/Graphene Composites as Anodes for Lithium/Sodium-Ion Batteries. *ChemSusChem* **11**, 1549–1557 (2018).

184. Chen, Y. *et al.* High-rate FeS2/CNT neural network nanostructure composite anodes for stable, high-capacity sodium-ion batteries. *Nano Energy* **46**, 117–127 (2018).
185. Zeng, X. *et al.* Conductive molybdenum carbide as the polysulfide reservoir for lithium-sulfur batteries. *J. Mater. Chem. A* **6**, 17142–17147 (2018).
186. Liu, B., Huang, S., Kong, D., Hu, J. & Yang, H. Y. Bifunctional NiCo 2 S 4 catalysts supported on a carbon textile interlayer for ultra-stable Li–S battery. *J. Mater. Chem. A* **7**, 7604–7613 (2019).
187. Dean, R. K. *et al.* Promoting sulfur immobilization by a hierarchical morphology of hollow carbon nanosphere clusters for high-stability Li–S battery. *J. Mater. Chem. A* **7**, 6250–6258 (2019).
188. Ahn, J. H., Shin, H. J., Abbas, S., Lee, K. Y. & Ha, H. Y. Plasma-functionalized carbon-layered separators for improved performance of lithium sulfur batteries. *J. Mater. Chem. A* **7**, 3772–3782 (2019).
189. Zhou, W. *et al.* Tailoring Pore Size of Nitrogen-Doped Hollow Carbon Nanospheres for Confining Sulfur in Lithium-Sulfur Batteries. *Adv. Energy Mater.* **5**, 1401752 (2015).
190. Zheng, G. *et al.* Hollow Carbon Nanofiber-Encapsulated Sulfur Cathodes for High Specific Capacity Rechargeable Lithium Batteries. *Nano Lett* **11**, 4462–4467 (2011).
191. Li, Z. *et al.* A sulfur host based on titanium monoxide@carbon hollow spheres for advanced lithium–sulfur batteries. *Nat. Commun.* **7**, 13065 (2016).
192. Chang, C. H. & Manthiram, A. Covalently Grafted Polysulfur-Graphene Nanocomposites for Ultrahigh Sulfur-Loading Lithium-Polysulfur Batteries. *ACS Energy Lett.* **3**, 72–77 (2018).
193. Zhang, Y. *et al.* High sulfur loading lithium-sulfur batteries based on a upper current collector electrode with lithium-ion conductive polymers. *J. Mater. Chem. A* **5**, 97–101 (2017).
194. Liang, X., Garsuch, A. & Nazar, L. F. Sulfur Cathodes Based on Conductive MXene Nanosheets for High-Performance Lithium-Sulfur Batteries. *Angew. Chemie* **127**, 3979–3983 (2015).
195. Cuisinier, M. *et al.* Sulfur Speciation in Li–S Batteries Determined by Operando X-ray Absorption Spectroscopy. *J. Phys. Chem. Lett.* **4**, 3227–3232 (2013).
196. Hou, T. Z. *et al.* Lithium Bond Chemistry in Lithium–Sulfur Batteries. *Angew. Chemie - Int. Ed.* **56**, 8178–8182 (2017).
197. Patel, M. U. M. *et al.* X-ray Absorption Near-Edge Structure and Nuclear Magnetic Resonance Study of the Lithium-Sulfur Battery and its Components. *ChemPhysChem* **15**, 894–904 (2014).
198. Liang, X. *et al.* Tuning Transition Metal Oxide-Sulfur Interactions for Long Life Lithium Sulfur Batteries: The ‘goldilocks’ Principle. *Adv. Energy Mater.* **6**, 1501636 (2016).
199. Pang, Q., Kundu, D., Cuisinier, M. & Nazar, L. F. Surface-enhanced redox chemistry of polysulphides on a metallic and polar host for lithium-sulphur batteries. *Nat. Commun.* **5**, (2014).
200. Liang, X. *et al.* A highly efficient polysulfide mediator for lithium-sulfur batteries. *Nat. Commun.* **6**, 5682 (2015).
201. Liu, M. *et al.* Novel gel polymer electrolyte for high-performance lithium-sulfur batteries. *Nano Energy* **22**, 278–289 (2016).

202. Li, H., Xi, H. an, Zhu, S., Wen, Z. & Wang, R. Preparation, structural characterization, and electrochemical properties of chemically modified mesoporous carbon. *Microporous Mesoporous Mater.* **96**, 357–362 (2006).
203. Li, W. *et al.* Dynamic behaviour of interphases and its implication on high-energy-density cathode materials in lithium-ion batteries. *Nat. Commun.* **8**, 14589 (2017).
204. Yuan, Z. *et al.* Powering Lithium-Sulfur Battery Performance by Propelling Polysulfide Redox at Sulfiphilic Hosts. *Nano Lett.* **16**, 519–527 (2016).
205. Zeng, S. *et al.* Conducting Polymers Crosslinked with Sulfur as Cathode Materials for High-Rate, Ultralong-Life Lithium–Sulfur Batteries. *ChemSusChem* **10**, 3378–3386 (2017).
206. Kosasang, S. *et al.* Insight into the effect of intercalated alkaline cations of layered manganese oxides on the oxygen reduction reaction and oxygen evolution reaction. *Chem. Commun.* **54**, 8575–8578 (2018).

VITA

Yun Li was born and raised in Chongqing, a municipality in southwest China. She attended Chongqing No.8 Middle School and graduated in 2009. She then got enrolled in Xiamen University and graduated with a B.S. in chemistry in 2013. At Xiamen University, she worked as an undergraduate researcher in Dr. Yong Yang' lab. This experience led her to find her interest in batteries. In September of 2013, she joined the University of Washington and began working under the supervision of Dr. Jihui Yang on versatile battery systems.